SAPIENZA
UNIVERSITÀ DI ROMA

Facoltà di Scienze Matematiche Fisiche e Naturali

The Bearable Lightness of New Physics Beyond the Standard Model

Thesis submitted for the degree of Doctor Philosophiae

Candidate

Claudio Toni

Thesis Directors

Prof. Marco Nardecchia

Dr. Luca Di Luzio

Teaching Board Advisor

Prof. Antonio Davide Polosa

XXXVI ciclo

To Francesco Totti,
whose vicissitudes were
the background of
my doctoral research

"Pulling back, I tried to find the point of wasting precious time,
I sip and toast to normalcy, a fool's way into jealousy,
I mock and imitate goodbyes when I know that I can't deny
That I'll be here forever-while, I show up to the party just to leave"

Amoeba, Clairo

Contents

Abstract

The absence of new physics signals at the TeV scale has recently triggered a shift of interest towards light and weakly coupled extensions of the Standard Model (SM). We consider a light new physics scenario coupled to the SM fields in a $SM + X$ effective theory. Different types of light new physics, searched by present and future experiments at the intensity frontier, are studied and investigated, from sub-GeV abelian gauge vector bosons to right-handed neutrinos at GeV scale. In the former case, we study the dependence on the UV completion of the effective Wess-Zumino terms that appears in the IR theory when gauge bosons are coupled to a SM current whose conservation is broken at loop level. We show how to avoid the would be strong constraints of energy enhanced process due to flavor changing neutral current generated by the Wess-Zumino terms [1, 2]. In the latter case, we work in a minimal see-saw scenario with two right-handed neutrinos with mass at the GeV scale and highlight the prospects for testing the decay $N_2 \to N_1\gamma$ induced by an effective dipole operator at future facilities targeting long-lived particles such as the SHiP experiment [3]. In the last part of the thesis, we critically re-examine the new particle interpretation of recent experimental anomalies observed in nuclear transition from the ATOMKI collaboration. Indeed, the hypothetical particle, denoted as $X17$ and proposed by the collaboration itself, would be a light and weakly-interacting boson and we employ a multipole expansion to estimate the nucleon coupling to the light state, identifying the axial vector state as the most promising candidate [4]. Intensity-frontier experiments like MEG II and PADME will probe the ATOMKI anomaly in the near future.

Introduction

The Standard Model (SM) of particle physics has achieved a remarkable success as a result of several decades of exploration, of constantly pushing the boundaries of our knowledge of theory, experiment, and technology. The discovery of the Higgs boson at LHC in 2012 [5] has been the last but not least of the many successful predictions of the SM. Since the birth of the theory in the 60s [6] and during its development in the 80s and 90s, the experimental search at the high-energy frontier provided the best tool to explore the physics and processes beyond the SM theory and led to the verification of almost all the SM predictions. The Livingston plot[1] in figure 1 shows us the history of discovery at the energy frontier and how accelerator science and technology provided the right tool to test and discover the SM over the last fifty years, from the 60s to the time of the Higgs discovery [7].

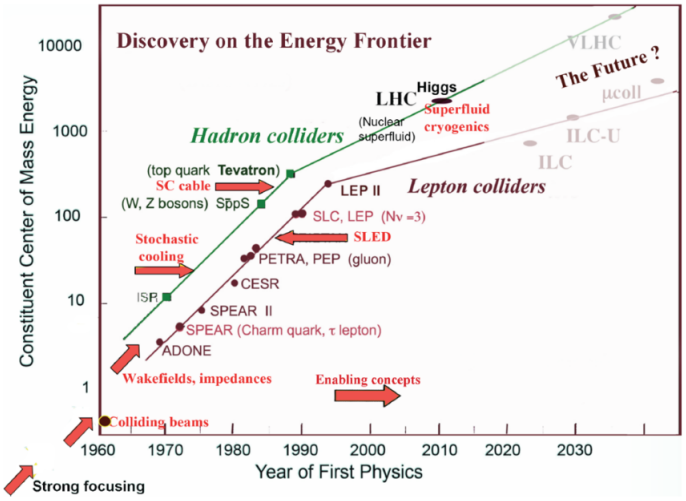

Figure 1: Livingston plot from *Planning the Future of U.S. Particle Physics (Snowmass 2013): Chapter 6: Accelerator Capabilities* [7].

However, while the SM provides a theoretically consistent description of all known particles and their interactions (ignoring gravity) up to the Planck scale, it is clearly incomplete as it does not address several pieces of evidence for new physics beyond the Standard Model (BSM), like the Dark Matter (DM) or the neutrino masses, as well as left unsolved some questions or aspects, like the hierarchy problem or the SM flavour structure. After the Higgs discovery, the community of high energy physics was expecting the presence of new physics at TeV scale, as suggested by many

[1] Its name comes from the first plot representing accelerator evolution showed by M. Stanley Livingston in his book *High-energy accelerators* (1954).

theoretical models (supersymmetry, extra dimensions, composite Higgs,...) in order to explain the hierarchy problem. Unfortunately, no BSM signal has been observed at the collider searches in the last ten years of searches, thus letting down our high expectations. Obviously, new physics may reside above the TeV-scale or may be even behind the corner, closer than we think, but the null result at colliders affected how we approach the search and research of new physics.

The disappointment of the energy-frontier searches slightly changes the paradigm of the phenomenological research over the last few years. The idea that new physics could well be found at the "low-energy frontier", and be accessible with intensity-frontier tools, has indeed gained more and more attention. Experiments that use intense beams of photons, charged particles, and/or sensitive detectors may be used to directly produce and study new, feebly-interacting particles that lie well below the Weak scale. This is the reason why, in the last years, light and weakly coupled new physics have raised considerable interest. Let consider as example two well motivated scenarios of light and weakly coupled new physics: the dark photon and the axion.

Besides gravity, there are only a few well-motivated interactions allowed by SM symmetries that provide a "portal" from the SM sector into the dark sector. One of this portal is the kinetic mixing between the hypercharge and dark abelian gauge tensor fields, leading to the idea of a dark photon [8]. Masses for the dark photon can arise trough an Higgs mechanism or a Stückelberg mechanism, especially in the context of large volume string compactifications with branes [9, 10], and can take on a large range of values, from the GeV scale to much smaller values (sub-eV).

One of the unresolved puzzles in the SM is the lack of any observed CP violation in the strong interactions described by Quantum Chromodynamics (QCD). Solutions to this problem are scarce. Perhaps the most popular suggestion is the so-called Peccei-Quinn (PQ) $U(1)$ approximate global symmetry, which is spontaneously broken at a scale f_a [11]. The axion is a hypothetical particle that arises as the pseudo-Nambu-Goldstone boson (PNGB) of this symmetry breaking [12].

In figure 2 we can see the net increase of citations per year of the axion and dark photon paradigms in recent years, a clear sign of how the focus of the phenomenological community has recently changed.

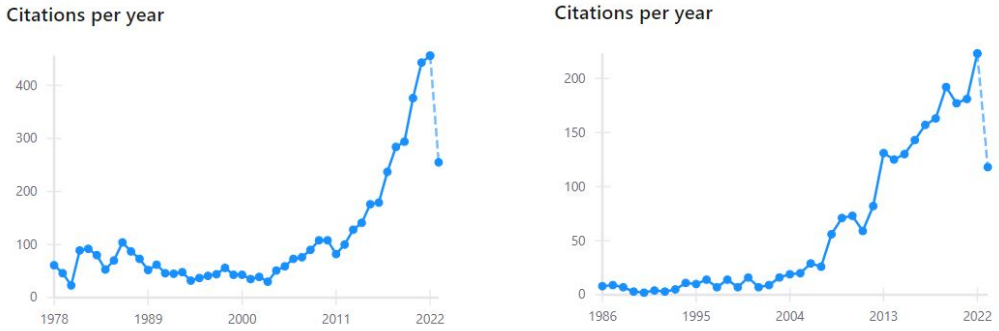

Figure 2: Number of citations per year of the funding papers of the axion [12] (left) and dark photon [8] (right) paradigm.

Given the intricate structure of the SM, which describes only a subdominant component of the Universe, it would not be too surprising if the dark sector contains a rich structure itself, with DM making up only a part of it. Indeed, many dark sectors could exist, each with its own beautiful structure, distinct particles, and forces. These dark sectors (or "hidden sectors") may contain new light weakly-coupled particles, particles well below the Weak-scale that interact only feebly with ordinary matter. Such particles could easily have escaped past experimental searches, but a rich experimental program has now been devised to look for several well-motivated possibilities. The

existence of such dark sectors, consisting of new, light, weakly-coupled particles that do not interact with the known SM forces, are motivated also by bottom-up and top-down theoretical considerations. They arise in many theoretical extensions to the SM, such as moduli that are present in string theory or new (pseudo-)scalars that appear naturally when symmetries are broken at high energy scales. Various experimental "anomalies", such as the discrepancy between the measured and calculated muon anomalous magnetic moment and some puzzling results from astrophysics provide exciting phenomenological motivations.

Existing facilities and technologies and small-case experiments enable the exploration of dark sectors. A rich, diverse, and low-cost experimental program is already underway that has the potential for one or more game-changing discoveries. Current ideas for extending the searches to smaller couplings and higher masses increase this potential considerably. Looking at the plot in figure 3, we see that such searches could explore a region of dark sector parameter space complementary to the one under observation in collider searches.

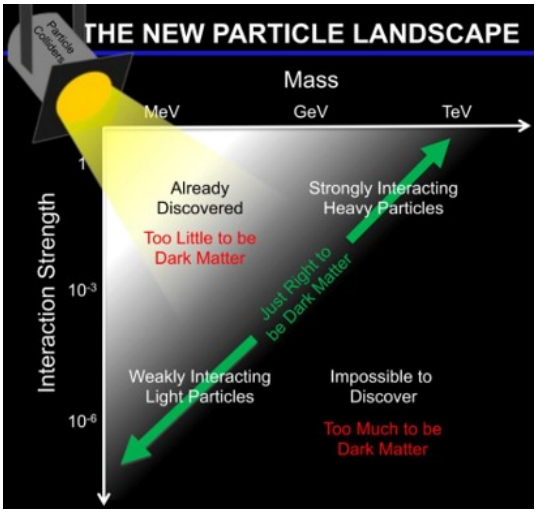

Figure 3: Figurative plot on the mass and coupling of Dark Matter searches from Jonathan Feng's talk at *"Shedding light on X17"* workshop [13]

Stated the novel prospective of the high energy physics community, the approach of the thesis has been to explore different lines of research that would include the presence of light new physics. Indeed, due to the lack of a primary direction of research in the high energy physics nowadays, we have chosen to space over the rich phenomenology that intensity-frontier can actually offer. We consider here scenarios where new physics (NP) is ultraviolet (UV) completed at very high energy scale but one or few NP states are light enough, i.e. are at the GeV scale or below, to be detectable at intensity-frontier experiment, even if they are weakly coupled to the SM fields. Hence we assume a infrared (IR) effective field theory where the field content is given by the SM plus a light new state, denoted agnostically as X, while every other UV field is heavier than the electroweak scale and integrated out. The focus is then to investigate the phenomenology of the $SM + X$ effective theory, where the X field can be for example a dark photon, an axion, right-handed neutrinos (RHNs), etc. In this work we consider two scenarios:

- the X field is a gauge boson and we study the dependence on the UV completion of the effective Wess-Zumino terms that appears in the IR theory;

- the X fields are two RHNs with masses at the GeV-scale and we highlight the prospects for testing the decay $N_2 \to N_1\gamma$ induced by an effective dipole operator,

and to each scenario we dedicate a chapter of first part of the thesis.

In the first chapter we investigate the dependence on UV physics of new light gauge vectors coupled to non conserved currents. As known, non conservation of vector currents gives rise to energy enhanced processes when the longitudinal state of the gauge boson is emitted, leading to strong constraints on the coupling and mass of such particles [14, 15]. A particular class of non conserved currents is when current conservation is exact at tree level but broken at loop by chiral anomalies, requiring new fermions in the UV or equivalently Wess-Zumino terms in the IR which, as recently pointed out [15], display an axion-like behaviour and lead to amplitudes that grow with the energy. Taking as a paradigmatic examples the gauging of baryon and lepton family number, anomaly-free UV models have been explicitly constructed introducing new mostly-chiral heavy fermions, such that Wess-Zumino terms are suppressed in the IR, thus relaxing would-be strong bounds on light dark vectors coupled to non-conserved currents [1]. However, the updated direct search for charged stable and unstable particles rules out the scenarios we explicitly consider [2].

In the second chapter we study the phenomenology of right-handed neutrinos magnetic moments at the GeV scale [3]. While the see-saw model [16, 17] is a full-fledged UV complete theory, in the case of electroweak scale RH neutrinos it is interesting to consider it as a low energy effective field theory (EFT) extended with higher dimensional operators build from the SM and the RHN fields, the so-called νSMEFT [18–21]. A minimal see-saw extension of the Standard Model with two right-handed singlet fermions with mass at the GeV scale is considered, augmented by an effective dipole operator between the sterile states, and current bounds on this effective interaction from fixed-target and collider experiments are taken in account to constraint the parameter space of the model.

In the second part we critically re-examine the possible theoretical interpretation of recent experimental anomalies observed in nuclear transition from the ATOMKI collaboration. Among the various processes that can be investigated at intensity frontier, rare nuclear transition can provide a good handle to observe NP appearing at the MeV scale, since they can significantly be affected by BSM physics even if this is very weakly coupled. The search of the ATOMKI collaboration leads to various anomalous measurements in the IPC decays of excited ^{8}Be [22], ^{4}He [23] and, more recently, ^{12}C [24] nuclei. Although to this day no independent confirmation of these results has arrived, given the multitude of processes in which these anomalies have been observed the ATOMKI results have attracted a considerable attention from the particle physics community. The collaboration itself proposed a new BSM boson X with mass around 17 MeV to explain the anomalous signal they measured. Following the recent interest on the topic and in view of the latest experimental results recently released by the ATOMKI collaboration [22, 23], we perform a phenomenological analysis within the usual $SM + X$ framework and estimate the range of values of the nucleon couplings to the new light state in order to match the experimental observations employing a multipole expansion method. Our conclusions identify the axial vector state as the most promising candidate, while other spin/parity assignments seem disfavored for a combined explanation [4].

Part I: $SM + X$ framework

Chapter 1

Light vectors coupled to anomalous currents with harmless Wess-Zumino terms

1.1 Introduction

The physics of light spin-1 dark boson has witnessed a growing amount of interest in the recent years, from both a theoretical and phenomenological standpoint. A standard benchmark is that of a secluded U(1) gauge boson, kinetically mixed with the photon [8] and hence universally coupled to the SM sector via the electromagnetic current. This framework, although elegant and predictive, can be too restrictive for phenomenological applications and hence more general forms of the light vector boson interactions with the SM fields can be envisaged. Going beyond the kinetic mixing framework, a theoretically motivated option is provided by the gauging of the accidental global symmetries of the SM, that is baryon number $\mathrm{U}(1)_B$ and family lepton number $\mathrm{U}(1)_{L_i}$ (with $i = e, \mu, \tau$) in the limit of massless neutrinos. Within the SM field content, only the $L_i - L_j$ combinations turn out to be anomaly free [25–27]. Hence, in order to consistently gauge a general linear combination

$$X = \alpha_B B + \sum_{i=e,\,\mu,\,\tau} \alpha_i L_i \,, \tag{1.1}$$

one requires new fermions, also known as *anomalons*, which cancel the anomalies of the new $\mathrm{U}(1)_X$ factor, also in combination with the electroweak gauge group. Note that Eq. (1.1) is the most general linear combination of abelian global symmetries of the SM that can be gauged, under the assumption that all SM Yukawa operators are allowed in the quark sector at the renormalizable level. Barring the cases of $B/3 - L_i$ and linear combinations thereof, the anomalons need to be charged under the electroweak gauge group (henceforth indicated more precisely as electroweak anomalons).[1] In the latter case, in order to evade detection at high-energy particle colliders, the new fermions need to be heavier than the electroweak scale. Consequently, their effects on the physics of the light vector boson associated with the $\mathrm{U}(1)_X$ gauge symmetry, here denoted as $\mathcal{X}$, can be described within an $SM + \mathcal{X}$ EFT approach. In particular, after integrating out the new heavy fermions at one loop, one generates dimension-4 Wess-Zumino (WZ) terms, schematically of the form $\mathcal{X}(W\partial W + WWW)$ and $\mathcal{X}B\partial B$ (with W and B denoting $\mathrm{SU}(2)_L$ and $\mathrm{U}(1)_Y$ gauge bosons). These contact interactions

[1] This is not the case if some of the quark Yukawa operators arise at the non-renormalizable level, as e.g. discussed recently in Ref. [28].

have the role of compensating, in the EFT without electroweak anomalons, the anomalous shift of the effective action due to the anomalous SM fermion current coupled to $\mathcal{X}$ (see e.g. [29–32]).

As it was emphasized more recently in Refs. [14, 15], WZ terms display an axion-like behaviour (as can be understood by applying the equivalence theorem to the longitudinal component of $\mathcal{X}$) and lead to amplitudes that grow with the energy. The anomalous $\mathcal{X}W\partial W$ vertex can be dressed with SM flavour-violating interactions leading to loop-induced flavour changing neutral current (FCNC) processes, while the anomalous $\mathcal{X}B\partial B$ vertex is responsible for $Z \to \gamma\mathcal{X}$ decays at the tree level (see also [33–36]). In both cases these processes are enhanced as $(\text{energy}/m_{\mathcal{X}})^2$, thus resulting into the typically most stringent bounds on light vectors with no direct couplings to electrons, as e.g. in the case of gauged baryon number.

It is known (see e.g. [15]) that in the limit where the mass of the anomalons stems from a SM-preserving vacuum expectation value (VEV), the low-energy coefficients of the WZ terms are entirely fixed by the requirement of canceling the $\mathrm{SU}(2)_L^2\mathrm{U}(1)_X$ and $\mathrm{U}(1)_Y^2\mathrm{U}(1)_X$ anomalies of the SM sector. On the other hand, if the anomalons pick up a mass contribution from the electroweak VEV then the coefficients of the WZ terms become model-dependent. In particular, in the limit where the anomalons mass is completely due to electroweak symmetry breaking sources, the anomalous couplings of the longitudinal component of $\mathcal{X}$ with SM electroweak gauge bosons goes to zero, thus relaxing the above mentioned strong bounds on light vectors.

In this chapter, we revisit the argument why WZ terms become harmless in the limit where the electroweak anomalons obtain their mass solely from the Higgs, classify the structure of UV completions that allow for such a pattern and discuss their electroweak-scale phenomenology. Due to its non-decoupling nature, the phenomenology of the electroweak anomalons is tightly constrained (but not yet ruled out) by Higgs coupling measurements and direct searches, thus making the whole setup testable at the high-luminosity phase of the LHC (HL-LHC). Chiral fermionic extensions of the SM, sharing some similarities with our setup, were previously discussed in a different context in Refs. [37,38]. Here, the main phenomenological interest consists in the physics of light (i.e. sub-GeV) vector bosons coupled to anomalous SM currents and the possibility of re-opening a large portion of parameter space, which might be probed by several low-energy experiments or help in explaining current experimental anomalies, such as e.g. that of the muon g-2 [39].

The chapter is structured as follows. Sect. 1.2 is the core of the work, in which we provide the general setup for the gauging of the generic linear combination of U(1) factors in Eq. (1.1). We discuss in particular the heavy anomalons sector leading to the cancellation of gauge anomalies and compute the resulting WZ terms in the EFT. In passing, we also deal with the issue of neutrino masses when lepton family generators are gauged. Sect. 1.3 is devoted instead to the phenomenology of the electroweak anomalons, in the limit where their mass dominantly stems from the Higgs VEV. In Sect. 1.4 we briefly consider the case where the $\mathcal{X}$ field acquire a mass trough the Stückelberg mechanism, thus leaving the $U(1)_X$ unbroken. We conclude in Sect. 1.5, while in App. A we collect a series of technical results about the calculation of WZ terms.

1.2 Gauging the Standard Model accidental symmetries

In this Section, we provide an explicit UV completion for the gauging of the most general combination of the SM global symmetries in Eq. (1.1), discuss the the conditions for the cancellation of gauge anomalies, compute the spectrum and the EFT below the scale of the heavy fermions (anomalons) assuming that the only new physics light state is the vector boson $\mathcal{X}$.

1.2.1 UV model

The field content of the model is displayed in Table 1.1, where the anomalon fields are highlighted in color and we also extended the scalar sector of the SM in order to spontaneously break the $\mathrm{U}(1)_X$ symmetry. Similar setups for anomaly cancellation were considered e.g. in Refs. [40–45].[2] Here, the more general SM charges of the electroweak anomalon fields $(\mathcal{L}, \mathcal{N}, \mathcal{E})$ are needed to evade LHC constraints on purely-chiral fermions for $\mathcal{Y} \approx 2, -1$ [37,38], as it will be reviewed in Sect. 1.3. In fact, as already anticipated in the Introduction, we will be interested in exploring the limit in which the electroweak anomalon masses are dominantly due to the Higgs, so that the strong bounds stemming from the anomalous WZ couplings of the light vector with SM gauge bosons are relaxed. We have also included N copies of chiral SM-singlet fermions ν_R^α $(\alpha = 1, \ldots, N)$ which allow to have more freedom for the cancellation of $\mathrm{U}(1)_X$ and $\mathrm{U}(1)_X^3$ anomalies (as well as provide a seesaw setup for neutrino masses), but whose presence does not impact the calculation of the electroweak WZ terms.

Field	Lorentz	$\mathrm{SU}(3)_C$	$\mathrm{SU}(2)_L$	$\mathrm{U}(1)_Y$	$\mathrm{U}(1)_X$
q_L^i	$(\frac{1}{2}, 0)$	3	2	$1/6$	$\alpha_B/3$
u_R^i	$(0, \frac{1}{2})$	3	1	$2/3$	$\alpha_B/3$
d_R^i	$(0, \frac{1}{2})$	3	1	$-1/3$	$\alpha_B/3$
ℓ_L^i	$(\frac{1}{2}, 0)$	1	2	$-1/2$	α_i
e_R^i	$(0, \frac{1}{2})$	1	1	-1	α_i
H	$(0, 0)$	1	2	$1/2$	0
$\mathcal{L}_L$	$(\frac{1}{2}, 0)$	1	2	$\mathcal{Y} - 1/2$	$X_{\mathcal{L}_L}$
$\mathcal{L}_R$	$(0, \frac{1}{2})$	1	2	$\mathcal{Y} - 1/2$	$X_{\mathcal{L}_R}$
$\mathcal{E}_L$	$(\frac{1}{2}, 0)$	1	1	$\mathcal{Y} - 1$	$X_{\mathcal{E}_L}$
$\mathcal{E}_R$	$(0, \frac{1}{2})$	1	1	$\mathcal{Y} - 1$	$X_{\mathcal{E}_R}$
$\mathcal{N}_L$	$(\frac{1}{2}, 0)$	1	1	$\mathcal{Y}$	$X_{\mathcal{N}_L}$
$\mathcal{N}_R$	$(0, \frac{1}{2})$	1	1	$\mathcal{Y}$	$X_{\mathcal{N}_R}$
ν_R^α	$(0, \frac{1}{2})$	1	1	0	$X_{\nu_R}^\alpha$
$\mathcal{S}$	$(0, 0)$	1	1	0	$X_{\mathcal{S}}$

Table 1.1: Anomaly-free field content for a general $\mathrm{SU}(3)_C \times \mathrm{SU}(2)_L \times \mathrm{U}(1)_Y \times \mathrm{U}(1)_X$ gauge theory, with $X = \alpha_B B + \sum_{i=e,\mu,\tau} \alpha_i L_i$. The conditions on the $\mathrm{U}(1)_X$ charges fulfilling the cancellation of gauge anomalies are reported in the text.

[2] For other anomalon configurations leading to anomaly cancellation when baryon and/or lepton number generators are gauged see e.g. [46, 47].

Anomaly cancellation

The $\mathrm{U}(1)_X$ charges are required to cancel all gauge anomalies. This corresponds to the following five conditions:

$$\begin{aligned}
\text{Gravity}\times\mathrm{U}(1)_X: \quad & 2(X_{\mathcal{L}_L}-X_{\mathcal{L}_R})+(X_{\mathcal{E}_L}-X_{\mathcal{E}_R})+(X_{\mathcal{N}_L}-X_{\mathcal{N}_R})-\sum_{\alpha=1}^{N}X^{\alpha}_{\nu_R} \\
& +\alpha_e+\alpha_\mu+\alpha_\tau=0\,, && (1.2)\\
\mathrm{U}(1)_X^3: \quad & 2(X^3_{\mathcal{L}_L}-X^3_{\mathcal{L}_R})+(X^3_{\mathcal{E}_L}-X^3_{\mathcal{E}_R})+(X^3_{\mathcal{N}_L}-X^3_{\mathcal{N}_R})-\sum_{\alpha=1}^{N}\left(X^{\alpha}_{\nu_R}\right)^3 \\
& +\alpha_e^3+\alpha_\mu^3+\alpha_\tau^3=0\,, && (1.3)\\
\mathrm{SU}(2)_L^2\times\mathrm{U}(1)_X: \quad & \frac{1}{2}(X_{\mathcal{L}_L}-X_{\mathcal{L}_R})+\frac{1}{2}(3\alpha_B+\alpha_e+\alpha_\mu+\alpha_\tau)=0\,, && (1.4)\\
\mathrm{U}(1)_Y^2\times\mathrm{U}(1)_X: \quad & 2(\mathcal{Y}-\frac{1}{2})^2(X_{\mathcal{L}_L}-X_{\mathcal{L}_R})+(\mathcal{Y}-1)^2(X_{\mathcal{E}_L}-X_{\mathcal{E}_R})+\mathcal{Y}^2(X_{\mathcal{N}_L}-X_{\mathcal{N}_R}) \\
& -\frac{1}{2}(3\alpha_B+\alpha_e+\alpha_\mu+\alpha_\tau)=0\,, && (1.5)\\
\mathrm{U}(1)_Y\times\mathrm{U}(1)_X^2: \quad & 2(\mathcal{Y}-\frac{1}{2})(X^2_{\mathcal{L}_L}-X^2_{\mathcal{L}_R})+(\mathcal{Y}-1)(X^2_{\mathcal{E}_L}-X^2_{\mathcal{E}_R})+\mathcal{Y}(X^2_{\mathcal{N}_L}-X^2_{\mathcal{N}_R})=0\,. && (1.6)
\end{aligned}$$

Renormalizable operators

Further constraints on the $\mathrm{U}(1)_X$ charges are obtained by the requirement that the electroweak anomalons pick up their mass from the VEV of H. Hence, the Yukawa Lagrangian involving the electroweak anomalon fields is (the discussion of neutrino masses is postponed to Sect. 1.2.3)

$$-\mathscr{L}_Y=y_1\bar{\mathcal{L}}_L\mathcal{E}_RH+y_2\bar{\mathcal{L}}_R\mathcal{E}_LH+y_3\bar{\mathcal{L}}_L\mathcal{N}_R\tilde{H}+y_4\bar{\mathcal{L}}_R\mathcal{N}_L\tilde{H}+\text{h.c.}\,, \tag{1.7}$$

with $\tilde{H}=i\sigma_2H^*$. The extra conditions on the $\mathrm{U}(1)_X$ charges stemming from Eq. (1.7) read

$$\begin{aligned}
X_{\mathcal{E}_R}&=X_{\mathcal{L}_L}\,, && (1.8)\\
X_{\mathcal{E}_L}&=X_{\mathcal{L}_R}\,, && (1.9)\\
X_{\mathcal{N}_R}&=X_{\mathcal{L}_L}\,, && (1.10)\\
X_{\mathcal{N}_L}&=X_{\mathcal{L}_R}\,, && (1.11)
\end{aligned}$$

thus reducing the number of independent charges to two. By substituting Eqs. (1.8)–(1.11) into Eqs. (1.2)–(1.6), we obtain the following non-trivial conditions

$$\begin{aligned}
X_{\mathcal{L}_R}-X_{\mathcal{L}_L}&=3\alpha_B+\alpha_e+\alpha_\mu+\alpha_\tau\equiv3\alpha_{B+L}\,, && (1.12)\\
\sum_{\alpha=1}^{N}X^{\alpha}_{\nu_R}&=\alpha_e+\alpha_\mu+\alpha_\tau\,, && (1.13)\\
\sum_{\alpha=1}^{N}\left(X^{\alpha}_{\nu_R}\right)^3&=\alpha_e^3+\alpha_\mu^3+\alpha_\tau^3\,, && (1.14)
\end{aligned}$$

where we have introduced the shorthand α_{B+L} defined in Eq. (1.12). Note that the condition of cancellation of electroweak anomalies fixes only the difference $X_{\mathcal{L}_R}-X_{\mathcal{L}_R}$, leaving us with one free charge that we choose to be $X_{\mathcal{L}_L}$. This redundancy is related to the electroweak anomalon number $\mathrm{U}(1)_A$, corresponding to a common re-phasing of the electroweak anomalon fields.

Other renormalizable operators, which are allowed by the SM gauge symmetry, may or may not be allowed by $\mathrm{U}(1)_X$ invariance. For instance, extra Yukawas of the type[3]

$$-\Delta\mathscr{L}_Y = y_{\mathcal{L}}\bar{\mathcal{L}}_L\mathcal{L}_R\mathcal{S}^* + y_{\mathcal{E}}\bar{\mathcal{E}}_L\mathcal{E}_R\mathcal{S} + y_{\mathcal{N}}\bar{\mathcal{N}}_L\mathcal{N}_R\mathcal{S} + \text{h.c.}\,, \tag{1.15}$$

are only permitted for $X_{\mathcal{S}} = X_{\mathcal{L}_R} - X_{\mathcal{L}_L} = 3\alpha_{B+L}$. These terms would yield an additional vector-like mass to the anomalons after $\mathrm{U}(1)_X$ symmetry breaking. Finally, for specific values of $\mathrm{U}(1)_Y$ and $\mathrm{U}(1)_X$ charges, the electroweak anomalons can mix with the SM leptons at the renormalizable level. The classification of $d = 4$ mixing operators is provided in Table 1.2, where we emphasized the phenomenologically relevant case $\mathcal{Y} = 2, -1$ (see Sect. 1.3.2). Note that in the presence of mixing operators the electroweak anomalon number is explicitly broken, and hence $X_{\mathcal{L}_L}$ gets fixed in terms of the coefficients of the X generator in Eq. (1.1).

Mixing operator	$\mathrm{U}(1)_Y$	$\mathrm{U}(1)_X$
$\bar{\ell}^i_L\mathcal{E}_R H$	$\mathcal{Y}=0$	$X_{\mathcal{L}_L}=\alpha_i$
$\bar{\ell}^i_L\mathcal{E}_R\tilde{H}$	$\mathcal{Y}=1$	$X_{\mathcal{L}_L}=\alpha_i$
$\bar{\ell}^i_L(\mathcal{E}_L)^c H$	$\mathcal{Y}=2$	$X_{\mathcal{L}_L}=-\alpha_i-3\alpha_{B+L}$
$\bar{\ell}^i_L(\mathcal{E}_L)^c\tilde{H}$	$\mathcal{Y}=1$	$X_{\mathcal{L}_L}=-\alpha_i-3\alpha_{B+L}$
$\bar{\ell}^i_L\mathcal{N}_R H$	$\mathcal{Y}=-1$	$X_{\mathcal{L}_L}=\alpha_i$
$\bar{\ell}^i_L\mathcal{N}_R\tilde{H}$	$\mathcal{Y}=0$	$X_{\mathcal{L}_L}=\alpha_i$
$\bar{\ell}^i_L(\mathcal{N}_L)^c H$	$\mathcal{Y}=1$	$X_{\mathcal{L}_L}=-\alpha_i-3\alpha_{B+L}$
$\bar{\ell}^i_L(\mathcal{N}_L)^c\tilde{H}$	$\mathcal{Y}=0$	$X_{\mathcal{L}_L}=-\alpha_i-3\alpha_{B+L}$
$\bar{\mathcal{L}}_L e^i_R H$	$\mathcal{Y}=0$	$X_{\mathcal{L}_L}=\alpha_i$
$\bar{\mathcal{L}}_L e^i_R\tilde{H}$	$\mathcal{Y}=-1$	$X_{\mathcal{L}_L}=\alpha_i$
$\bar{\mathcal{L}}_R(e^i_R)^c H$	$\mathcal{Y}=2$	$X_{\mathcal{L}_L}=-\alpha_i-3\alpha_{B+L}$
$\bar{\mathcal{L}}_R(e^i_R)^c\tilde{H}$	$\mathcal{Y}=1$	$X_{\mathcal{L}_L}=-\alpha_i-3\alpha_{B+L}$
$\bar{\mathcal{L}}_L\nu^\alpha_R H$	$\mathcal{Y}=1$	$X_{\mathcal{L}_L}=X^\alpha_{\nu_R}$
$\bar{\mathcal{L}}_L\nu^\alpha_R\tilde{H}$	$\mathcal{Y}=0$	$X_{\mathcal{L}_L}=X^\alpha_{\nu_R}$
$\bar{\mathcal{L}}_R(\nu^\alpha_R)^c H$	$\mathcal{Y}=1$	$X_{\mathcal{L}_L}=-X^\alpha_{\nu_R}-3\alpha_{B+L}$
$\bar{\mathcal{L}}_R(\nu^\alpha_R)^c\tilde{H}$	$\mathcal{Y}=0$	$X_{\mathcal{L}_L}=-X^\alpha_{\nu_R}-3\alpha_{B+L}$
$\bar{\mathcal{L}}_R\ell^i_L\mathcal{S}$	$\mathcal{Y}=0$	$X_{\mathcal{L}_L}=\alpha_i+X_{\mathcal{S}}-3\alpha_{B+L}$
$\bar{\mathcal{L}}_L(\ell^i_L)^c\mathcal{S}$	$\mathcal{Y}=1$	$X_{\mathcal{L}_L}=-\alpha_i+X_{\mathcal{S}}$
$\bar{\mathcal{E}}_L e^i_R\mathcal{S}$	$\mathcal{Y}=0$	$X_{\mathcal{L}_L}=\alpha_i+X_{\mathcal{S}}-3\alpha_{B+L}$
$\bar{\mathcal{E}}_L\nu^\alpha_R\mathcal{S}$	$\mathcal{Y}=1$	$X_{\mathcal{L}_L}=X^\alpha_{\nu_R}+X_{\mathcal{S}}-3\alpha_{B+L}$
$\bar{\mathcal{E}}_R(e^i_R)^c\mathcal{S}$	$\mathcal{Y}=2$	$X_{\mathcal{L}_L}=-\alpha_i+X_{\mathcal{S}}$
$\bar{\mathcal{E}}_R(\nu^\alpha_R)^c\mathcal{S}$	$\mathcal{Y}=1$	$X_{\mathcal{L}_L}=-X^\alpha_{\nu_R}+X_{\mathcal{S}}$
$\bar{\mathcal{N}}_L e^i_R\mathcal{S}$	$\mathcal{Y}=-1$	$X_{\mathcal{L}_L}=\alpha_i+X_{\mathcal{S}}-3\alpha_{B+L}$
$\bar{\mathcal{N}}_L\nu^\alpha_R\mathcal{S}$	$\mathcal{Y}=0$	$X_{\mathcal{L}_L}=X^\alpha_{\nu_R}+X_{\mathcal{S}}-3\alpha_{B+L}$
$\bar{\mathcal{N}}_R(e^i_R)^c\mathcal{S}$	$\mathcal{Y}=1$	$X_{\mathcal{L}_L}=-\alpha_i+X_{\mathcal{S}}$
$\bar{\mathcal{N}}_R(\nu^\alpha_R)^c\mathcal{S}$	$\mathcal{Y}=0$	$X_{\mathcal{L}_L}=-X^\alpha_{\nu_R}+X_{\mathcal{S}}$

Table 1.2: Renormalizable operators leading to a mixing between electroweak anomalons and SM leptons (first column) and required conditions on $\mathrm{U}(1)_Y$ and $\mathrm{U}(1)_X$ charges (second and third columns). For completeness, we also include mixings via RH neutrinos and/or $\mathcal{S}$, whose $\mathrm{U}(1)_X$ charges depend on the mechanism giving mass to neutrinos (see Sect. 1.2.3). Mixing operators via $\mathcal{S}^*$ are trivially obtained by flipping the sign of $X_{\mathcal{S}}$ in the third column.

[3]The case $\mathcal{S} \to \mathcal{S}^*$ is trivially obtained by replacing $X_{\mathcal{S}} \to -X_{\mathcal{S}}$.

Spectrum

By adding a proper term in the scalar potential, $\Delta V(H,\mathcal{S})$, the following VEV configurations are generated

$$\langle H\rangle = \frac{1}{\sqrt{2}}\begin{pmatrix}0\\ v\end{pmatrix}\,, \qquad \langle \mathcal{S}\rangle = \frac{v_X}{\sqrt{2}}\,, \tag{1.16}$$

with $v \simeq 246$ GeV and v_X being the order parameter of $\mathrm{U}(1)_X$ breaking. The latter is responsible for the mass of the $\mathrm{U}(1)_X$ gauge boson, $\mathcal{X}^\mu$, that is

$$m_{\mathcal{X}} = X_{\mathcal{S}} g_X v_X\,, \tag{1.17}$$

where g_X is the $\mathrm{U}(1)_X$ gauge coupling entering the covariant derivative, i.e. $D^\mu\mathcal{S} = (\partial^\mu + i g_X X_{\mathcal{S}} \mathcal{X}^\mu)\mathcal{S}$. The scalar field can be expanded around the vacuum as $\mathcal{S} = \frac{v_X}{\sqrt{2}} e^{i\xi/v_X} + \ldots$, where ξ is the Goldstone boson associated with the massive state $\mathcal{X}$ and we neglected the radial mode. After $\mathrm{U}(1)_X$ and electroweak symmetry breaking the Yukawa terms in $\mathscr{L}_Y + \Delta\mathscr{L}_Y$ (see Eq. (1.7) and Eq. (1.15)) give mass to the electroweak anomalons (neglecting for simplicity possible mixings with the SM sector)

$$-\mathscr{L}_{\rm mass} = \bar\Psi^{\mathcal{E}}_L \mathcal{M}_{\mathcal{E}}\, \Psi^{\mathcal{E}}_R + \bar\Psi^{\mathcal{N}}_L \mathcal{M}_{\mathcal{N}}\, \Psi^{\mathcal{N}}_R + \text{h.c.}\,, \tag{1.18}$$

which can be cast into 2-flavour Dirac fermions, $\Psi^{\mathcal{E}}_{L,R} = (\mathcal{E}_{\mathcal{L}_{L,R}}, \mathcal{E}_{L,R})$ and $\Psi^{\mathcal{N}}_{L,R} = (\mathcal{N}_{\mathcal{L}_{L,R}}, \mathcal{N}_{L,R})$, with

$$\mathcal{M}_{\mathcal{E}} = \begin{pmatrix} m_{\mathcal{L}} & m_1\\ m_2^* & m_{\mathcal{E}}\end{pmatrix}\,, \qquad \mathcal{M}_{\mathcal{N}} = \begin{pmatrix} m_{\mathcal{L}} & m_3\\ m_4^* & m_{\mathcal{N}}\end{pmatrix}\,, \tag{1.19}$$

and

$$m_{\mathcal{L},\mathcal{E},\mathcal{N}} = \frac{y_{\mathcal{L},\mathcal{E},\mathcal{N}}}{\sqrt{2}} v_X\,, \qquad m_{1,2,3,4} = \frac{y_{1,2,3,4}}{\sqrt{2}} v\,. \tag{1.20}$$

The mass matrices are diagonalized via the bi-unitary transformations $\Psi^{\mathcal{E},\mathcal{N}}_R \to U_{\mathcal{E},\mathcal{N}}\, \Psi^{\mathcal{E},\mathcal{N}}_R$ and $\Psi^{\mathcal{E},\mathcal{N}}_L \to V_{\mathcal{E},\mathcal{N}}\, \Psi^{\mathcal{E},\mathcal{N}}_L$, with the unitary matrices entering non-trivially into the gauge currents in the mass basis. In the limit $y_{\mathcal{E}} = y_{\mathcal{N}}$, $y_1 = y_3$, $y_2 = y_4$ (and hence $\mathcal{M}_{\mathcal{E}} = \mathcal{M}_{\mathcal{N}}$), the Yukawa Lagrangian features a custodial symmetry which helps in taming corrections to electroweak precision observables (see Sect. 1.3.1). In the following, we will stick to the custodial limit, while for the calculations in App. A we will consider the more general case.

1.2.2 EFT of a light vector and decoupling of WZ terms

We are interested in the limit where the electroweak anomalons are heavier the electroweak scale, while the vector $\mathcal{X}$ is much lighter than the electroweak scale. Parametrically (see Eq. (1.17)), this can be obtained in two ways: *i)* $v_X \gtrsim v$ and $g_X \ll 1$ or *ii)* $v_X \ll v$ and $g_X \lesssim 1$. In case *ii)* or if the $\Delta\mathscr{L}_Y$ operators in Eq. (1.15) are absent due to charge assignment (i.e. $X_{\mathcal{S}} \neq 3\alpha_{B+L}$), this requires $y_{1,2,3,4} \sim \sqrt{4\pi}$ in order for the anomalons to be heavier than the electroweak scale. Upon integrating out the electroweak anomalons at one loop one finds in the EFT given by the SM and the light vector $\mathcal{X}$ (also keeping the Goldstone mode ξ, see App. A for details)

$$\begin{aligned}
\mathscr{L}^{\mathrm{U}(1)_X}_{\rm EFT} \supset\; & g_X g'^2 \frac{C_{BB}}{24\pi^2}\epsilon^{\alpha\mu\nu\beta}\mathcal{X}_\alpha B_\mu \partial_\beta B_\nu + g_X g^2 \frac{C_{ab}}{24\pi^2}\epsilon^{\alpha\mu\nu\beta}\mathcal{X}_\alpha W^a_\mu \partial_\beta W^b_\nu\\
& + g_X g g' \frac{C_{aB}}{24\pi^2}\epsilon^{\alpha\mu\nu\beta}\mathcal{X}_\alpha W^a_\mu \partial_\beta B_\nu + g_X g g' \frac{C_{Ba}}{24\pi^2}\epsilon^{\alpha\mu\nu\beta}\mathcal{X}_\alpha B_\mu \partial_\beta W^a_\nu\\
& + g_X g^2 \frac{D_{ab}}{48\pi^2}\frac{\xi}{m_{\mathcal{X}}}\epsilon^{\alpha\mu\beta\nu}(\partial_\alpha W^a_\mu)(\partial_\beta W^b_\nu) + g_X g'^2 \frac{D_{BB}}{48\pi^2}\frac{\xi}{m_{\mathcal{X}}}\epsilon^{\alpha\mu\beta\nu}(\partial_\alpha B_\mu)(\partial_\beta B_\nu)\\
& + g_X g g' \frac{D_{aB}}{24\pi^2}\frac{\xi}{m_{\mathcal{X}}}\epsilon^{\alpha\mu\beta\nu}(\partial_\alpha W^a_\mu)(\partial_\beta B_\nu)\,,
\end{aligned} \tag{1.21}$$

where $a, b = 1, 2, 3$ and we neglected non-abelian W terms scaling with an extra gauge coupling g. In general, from the requirement that the electromagnetic group remains unbroken, one obtains

$$C_{ab} = \begin{pmatrix} C_{11} & C_{12} & 0 \\ -C_{12} & C_{11} & 0 \\ 0 & 0 & C_{33} \end{pmatrix}, \quad C_{aB} = \begin{pmatrix} 0, & 0, & C_{3B} \end{pmatrix}, \quad C_{Ba} = \begin{pmatrix} 0, & 0, & C_{B3} \end{pmatrix}, \tag{1.22}$$

$$D_{ab} = \begin{pmatrix} D_{11} & 0 & 0 \\ 0 & D_{11} & 0 \\ 0 & 0 & D_{33} \end{pmatrix}, \quad D_{aB} = \begin{pmatrix} 0, & 0, & D_{3B} \end{pmatrix}, \tag{1.23}$$

together with the sum-rules

$$C_{33} + C_{3B} + C_{B3} + C_{BB} = 0\,, \tag{1.24}$$

$$D_{33} + 2D_{3B} + D_{BB} = 0\,. \tag{1.25}$$

A relatively simple case is given in the limit where the masses of the anomalon fields stem completely from the VEV of $\mathcal{S}$, yielding

$$C_{11} = C_{33} = -C_{BB} = 3\alpha_{B+L}\,, \tag{1.26}$$

$$C_{B3} = -C_{3B} = D_{3B} = C_{12} = 0\,, \tag{1.27}$$

$$D_{11} = D_{33} = -D_{BB} = -9\alpha_{B+L}\,, \tag{1.28}$$

where the effective coefficients are set by the anomalous trace of the SM current (see Eqs. (A.46)–(A.47)). Here, instead, we focus on the more general case where the anomalon masses have both a SM-singlet and an electroweak symmetry breaking source. Although we were not able to cast explicit expressions for the EFT coefficients into a simple analytical form (see Eqs. (A.28)–(A.29)), we will present them here under the simplified (but phenomenologically motivated) hypothesis in which the anomalon masses are degenerate, that is

$$\mathcal{M}_{\mathcal{E}}^{\dagger}\mathcal{M}_{\mathcal{E}} = \mathcal{M}_{\mathcal{N}}^{\dagger}\mathcal{M}_{\mathcal{N}} = m_{\Psi}^2 \begin{pmatrix} 1 & 0 \\ 0 & 1 \end{pmatrix}, \tag{1.29}$$

with m_Ψ denoting the degenerate anomalons mass. Eq. (1.29) enforces the mass matrices to be

$$\mathcal{M}_{\mathcal{E}} = \mathcal{M}_{\mathcal{N}} = \frac{1}{\sqrt{2}} \begin{pmatrix} y_{\mathcal{S}} v_X & i y_H v \\ i y_H v & y_{\mathcal{S}} v_X \end{pmatrix} = m_\Psi \begin{pmatrix} \cos\theta & i\sin\theta \\ i\sin\theta & \cos\theta \end{pmatrix}, \tag{1.30}$$

with $y_{\mathcal{S},H}$ real parameters,[4] while

$$m_\Psi^2 = \frac{1}{2}\left((y_H v)^2 + (y_S v_X)^2\right), \tag{1.31}$$

and

$$\tan\theta = \frac{y_H v}{y_S v_X}\,. \tag{1.32}$$

[4]The accidental global $\mathrm{U}(1)^6$ symmetry corresponding to the re-phasing of the each electroweak anomalon field is broken by the $\mathscr{L}_Y + \Delta\mathscr{L}_Y$, leaving an unbroken electroweak anomalon number $\mathrm{U}(1)_A$, that is the subgroup corresponding to the common re-phasing of all the anomalon fields. Hence, of the seven complex parameters introduced in $\mathscr{L}_Y + \Delta\mathscr{L}_Y$, $6 - 1 = 5$ phases are unphysical and can be rotated away. One possible choice is to set $\mathrm{Arg}(y_{\mathcal{L}}) = \mathrm{Arg}(y_{\mathcal{E}}) = \mathrm{Arg}(y_{\mathcal{N}}) = 0$, $\mathrm{Arg}(y_1) = -\mathrm{Arg}(y_2)$, and $\mathrm{Arg}(y_3) = -\mathrm{Arg}(y_4)$.

Specializing the general expressions in Eqs. (A.28)–(A.29) to the degenerate case above, we find

$$C_{11} = C_{33} = -C_{BB} = \frac{3}{4}\alpha_{B+L}(1+3\cos 2\theta)\,, \tag{1.33}$$

$$C_{B3} = -C_{3B} = \frac{9}{4}\alpha_{B+L}(1-\cos 2\theta), \qquad C_{12} = 0\,, \tag{1.34}$$

$$D_{11} = D_{33} = -D_{BB} = -\frac{9}{2}\alpha_{B+L}(1+\cos 2\theta), \qquad D_{3B} = 0\,. \tag{1.35}$$

The important point to be noted is that when the anomalons pick-up a mass from both electroweak preserving and breaking sources, the low-energy WZ coefficients acquire a model dependence through the angle θ.

In order to understand the phenomenological implications of this model dependence, we briefly recall here the argument of Refs. [14,15] regarding the energy-enhanced emission of the longitudinal modes of $\mathcal{X}$ stemming from the WZ operators. Taking the limit $g_X \to 0$ and $m_{\mathcal{X}} \to 0$, while keeping fixed the ratio $m_{\mathcal{X}}/g_X \propto v_X$, the transverse modes of $\mathcal{X}$ decouple, while the longitudinal mode is enhanced as $E/m_{\mathcal{X}}$. In this regime, the equivalence theorem states that the longitudinally polarized vectors are equivalent to the corresponding scalar Goldstone bosons. This is readily seen by working in the so-called "Equivalent Gauge" of Ref. [48], where the longitudinally polarized state, $|\mathcal{X}_L\rangle$, is represented as

$$\langle 0|\mathcal{X}_\mu(x)|\mathcal{X}_L(\vec{p})\rangle = \epsilon^L_\mu(\vec{p})e^{-ipx}\,, \qquad \langle 0|\xi(x)|\mathcal{X}_L(\vec{p})\rangle = -ie^{-ipx}\,, \tag{1.36}$$

with the polarization vector

$$\epsilon^L_\mu(\vec{p}) = -\frac{m_{\mathcal{X}}}{E_{\vec{p}}+|\vec{p}|}\left\{1, \frac{\vec{p}}{|\vec{p}|}\right\}\,, \tag{1.37}$$

vanishing in the $m_{\mathcal{X}} \to 0$ limit. The advantage of this representation is that it makes the equivalence theorem explicit, since in the high-energy limit (or equivalently $m_{\mathcal{X}} \to 0$) only the Goldstone mode survives. Hence, adopting the above prescription, only the diagrams with one external ξ contribute to physical processes in the $m_{\mathcal{X}} \to 0$ limit. For instance, upon integrating out the W boson, the axion-like operator $\xi W^- \bar{W}^+$ proportional to D_{11} in Eq. (1.21) yields the effective interaction

$$g_{\xi d_i d_j}\bar{d}_j\gamma^\mu P_L d_i\,(\partial_\mu\xi/m_{\mathcal{X}}) + \text{h.c.}\,, \tag{1.38}$$

in terms of the effective coupling [49]

$$g_{\xi d_i d_j} = -\frac{g_X g^4}{(4\pi)^4}D_{11}\sum_{\alpha=u,c,t}V_{\alpha i}V^*_{\alpha j}F(m^2_\alpha/m^2_W)\,, \tag{1.39}$$

with $D_{11} \propto (1+\cos 2\theta)$ given in Eq. (1.35), V denoting the CKM matrix and the loop function

$$F(x) = \frac{x(1+x(\ln x - 1))}{(1-x)^2}\,. \tag{1.40}$$

This leads to FCNC processes, such as $K \to \pi\mathcal{X}_L$, $B \to K\mathcal{X}_L$, etc, whose rate is enhanced as $(E/m_{\mathcal{X}})^2$, where E is the decay energy (cf. the derivative operator in Eq. (1.38)), thus implying strong bounds on light vector bosons coupled to anomalous currents [14,15].

On the other hand, the above constraints from energy-enhanced $\mathcal{X}_L$ emission disappear for $D_{11} = 0$, that is when the $\mathrm{U}(1)_X$ Goldstone decouples from the electroweak anomalons. This corresponds to $\theta = \pi/2$, which implies that the anomalon masses are entirely due to the Higgs VEV (cf. Eq. (1.32)). From a top-down perspective this condition can be neatly obtained in terms of

$\mathrm{U}(1)_X$ charges ($X_\mathcal{S} \neq 3\alpha_{B+L}$) which forbid the operators of $\Delta\mathscr{L}_Y$ in Eq. (1.15). Alternatively, it can be parametrically obtained by taking $v_X \ll v$ or $y_\mathcal{S} \approx 0$. Note that the latter condition is radiatively stable, since it corresponds to an enhanced U(1) global symmetry of the Lagrangian in which LH and RH anomalons fields are rotated with an opposite phase.

In conclusion, we have shown that the bounds of Refs. [14, 15] can be relaxed by assuming that the anomalon fields are mostly chiral (namely, their mass mostly stems from the Higgs VEV). This possibility, however, leads to non-decoupling signatures in Higgs observables and direct searches, to be discussed in Sect. 1.3.

1.2.3 Neutrino masses

If the X generator has a non-trivial projection on family lepton numbers, $\alpha_i \neq 0$ ($i = e, \mu, \tau$), then we need RH neutrinos, ν_R^α ($\alpha = 1, \ldots, N$), in order to cancel $\mathrm{U}(1)_X$ and $\mathrm{U}(1)_X^3$ anomalies (cf. conditions in Eqs. (1.13)–(1.14)). The simplest solution is to introduce one RH neutrino for each $\alpha_i \neq 0$ and set $X^i_{\nu_R} = \alpha_i$. Another possibility is to have universal charges $X^\alpha_{\nu_R} = X_{\nu_R}$, so that the anomaly-free conditions are

$$X_{\nu_R} = \left(\frac{\alpha_e^3 + \alpha_\mu^3 + \alpha_\tau^3}{\alpha_e + \alpha_\mu + \alpha_\tau}\right)^{1/2}, \qquad N = \left(\frac{(\alpha_e + \alpha_\mu + \alpha_\tau)^3}{\alpha_e^3 + \alpha_\mu^3 + \alpha_\tau^3}\right)^{1/2}. \tag{1.41}$$

The SM-singlet states ν_R^α can be used to give mass to light neutrinos via the seesaw mechanism. In fact, SM gauge invariance would allow the operators[5]

$$-\mathscr{L}_Y^{\nu_R} = y_D^{i\beta}\bar{\ell}_L^i \nu_R^\beta \tilde{H} + \frac{1}{2} y_{\nu_R}^{\alpha\beta} \nu_R^\alpha \nu_R^\beta \mathcal{S}^* + \text{h.c.} \quad \longrightarrow \quad m_D^{i\beta}\,\bar{\ell}_L^i \nu_R^\beta + \frac{1}{2} M_R^{\alpha\beta} \nu_R^\alpha \nu_R^\beta + \text{h.c.}\,, \tag{1.42}$$

with $m_D = y_D v/\sqrt{2}$ and $M_R = y_R v_X/\sqrt{2}$, leading to light neutrino masses via the seesaw mechanism

$$m_\nu = m_D M_R^{-1} m_D^T\,. \tag{1.43}$$

However, in order for the operators in Eq. (1.42) to be $\mathrm{U}(1)_X$ invariant, the following constraints on $\mathrm{U}(1)_X$ charges need to be satisfied

$$-\alpha_i + X^\beta_{\nu_R} = 0\,, \tag{1.44}$$

$$X^\alpha_{\nu_R} + X^\beta_{\nu_R} - X_\mathcal{S} = 0\,. \tag{1.45}$$

While the first condition can be easily fulfilled (since it also ensures the cancellation of $\mathrm{U}(1)_X$ and $\mathrm{U}(1)_X^3$ anomalies), the second one could imply texture zeros in M_R if some leptonic generators are non-universal $\alpha_i \neq \alpha_j$. Consistency with light neutrino data might then require the introduction of extra scalars in order to reproduce realistic low-energy textures (see e.g. [50–52]).

1.3 Electroweak anomalons phenomenology

In the previous Section we have seen that mostly chiral electroweak anomalons (i.e. which take their mass mostly from the Higgs VEV) allow to decouple dangerous WZ terms, which would otherwise lead to the energy-enhanced longitudinal emission of light vectors coupled to anomalous currents. We are hence interested in studying the electroweak phenomenology of the exotic leptons $\mathcal{L} + \mathcal{N} + \mathcal{E}$, whose quantum numbers are displayed in Table 1.1. In particular, following the analysis of Refs. [37, 38], we will argue that phenomenology requires $\mathcal{Y} \approx 2, -1$.

[5] We neglect here bare Majorana mass terms, since in that case RH neutrinos would not contribute to the cancellation of $\mathrm{U}(1)_X$ and $\mathrm{U}(1)_X^3$ anomalies. Instead, possible mixings between RH neutrinos and electroweak anomalons have been classified in Table 1.2.

1.3.1 Electroweak precision tests

The contribution of the electroweak anomalons in terms of mass eigenstates (cf. Table 1.1 and Eq. (1.18)) to the S and T parameters is [37]

$$S = \frac{1}{6\pi}\Big[\big(1-2(\mathcal{Y}-\frac{1}{2})\log\frac{m^2_{\mathcal{N}_1}}{m^2_{\mathcal{E}_1}}\big)+\big(1+2(\mathcal{Y}-\frac{1}{2})\log\frac{m^2_{\mathcal{N}_2}}{m^2_{\mathcal{E}_2}}\big)+\mathcal{O}\big(\frac{m_Z^2}{m^2_{\mathcal{N},\mathcal{E}}}\big)\Big]\approx\frac{1}{3\pi}\,, \tag{1.46}$$

$$\begin{aligned} T = {}& \frac{1}{16\pi c_W^2 s_W^2 m_Z^2}\big(m^2_{\mathcal{N}_1}+m^2_{\mathcal{E}_1}-2\frac{m^2_{\mathcal{N}_1}m^2_{\mathcal{E}_1}}{m^2_{\mathcal{N}_1}-m^2_{\mathcal{E}_1}}\log\frac{m^2_{\mathcal{N}_1}}{m^2_{\mathcal{E}_1}}\big) \\ & + \frac{1}{16\pi c_W^2 s_W^2 m_Z^2}\big(m^2_{\mathcal{N}_2}+m^2_{\mathcal{E}_2}-2\frac{m^2_{\mathcal{N}_2}m^2_{\mathcal{E}_2}}{m^2_{\mathcal{N}_2}-m^2_{\mathcal{E}_2}}\log\frac{m^2_{\mathcal{N}_2}}{m^2_{\mathcal{E}_2}}\big)\approx 0\,, \end{aligned} \tag{1.47}$$

where the approximation in the last steps holds in the custodial limit $m_{\mathcal{N}_{1,2}} \approx m_{\mathcal{E}_{1,2}}$. Recent fits for oblique parameters, e.g. from Gfitter [53], yield

$$S = 0.05 \pm 0.11\,, \qquad T = 0.09 \pm 0.13\,, \tag{1.48}$$

which are easily satisfied in the custodial limit, although a mass splitting might play a role to explain the recent M_W anomaly [54].

1.3.2 Higgs physics

We now consider the constraints from Higgs coupling measurements. In particular, we assess the impact of the new heavy fermions on the decay rate of the Higgs boson to two photons, or to a photon and a Z boson. Taking a fermion ψ of mass m_ψ the interaction Lagrangian is given by

$$\mathcal{L}^{\rm int}_\psi = -\frac{m_\psi}{v}h\overline{\psi}\psi + eQ_\psi\overline{\psi}\gamma^\mu\psi A_\mu + \frac{e}{c_W s_W}\overline{\psi}\gamma^\mu\left(\frac{T^3_\psi}{2}-Q_\psi s_W^2-\frac{T^3_\psi}{2}\gamma_5\right)\psi Z_\mu\,, \tag{1.49}$$

where h is the 125 GeV Higgs, A_μ and Z_μ the photon and Z boson fields, T^3_ψ is the eigenvalue of the third generator of $\mathrm{SU}(2)_L$ when it acts on the left-handed component of ψ, so that $T^3_\psi = \pm\frac{1}{2}$ when ψ_L arises from a doublet in the fundamental of $\mathrm{SU}(2)_L$. Its one-loop contributions to the amplitudes $h\to\gamma\gamma$ and $h\to\gamma Z$ are [55]

$$\mathcal{A}^\psi_{\gamma\gamma} \approx \frac{4}{3}Q^2_\psi\,, \quad \mathcal{A}^\psi_{Z\gamma} \approx -\frac{1}{3}Q_\psi\frac{T^3_\psi-2Q_\psi s_W^2}{c_W}\,, \tag{1.50}$$

where we assumed that ψ is much heavier than the Higgs and the Z boson, which holds for the heavy fermions we consider here. In the SM, these amplitudes are dominated by the loop of the W gauge boson interfering negatively with the loop of the top quark and they amount to $A^{\rm SM}_{\gamma\gamma}\approx -6.5$ and $\mathcal{A}^{\rm SM}_{\gamma Z}\approx 5.7$ at leading order. In the presence of a single Higgs doublet, the new physics contribution yields $\mathcal{A}^{\rm NP}_{\gamma\gamma}\approx\frac{8}{3}(1-2\mathcal{Y}+2\mathcal{Y}^2)$. Writing the modified Higgs width to photons as

$$R_{\gamma\gamma} = \frac{|\mathcal{A}^{\rm SM}_{\gamma\gamma}+\mathcal{A}^{\rm NP}_{\gamma\gamma}|^2}{|\mathcal{A}^{\rm SM}_{\gamma\gamma}|^2}\,, \tag{1.51}$$

a recent ATLAS analysis found $R_{\gamma\gamma}=1.00\pm0.12$ [56]. There is in fact the possibility that the new physics contribution interferes negatively with the SM amplitude, namely $\mathcal{A}^{\rm NP}_{\gamma\gamma}\approx -2\mathcal{A}^{\rm SM}_{\gamma\gamma}\approx 13.0$. This is obtained either for $\mathcal{Y}\approx 2$ ($1.93\lesssim\mathcal{Y}\lesssim 2.03$ [2σ range]) or $\mathcal{Y}\approx -1$ ($-1.03\lesssim\mathcal{Y}\lesssim -0.93$ [2σ range]), both yielding $\mathcal{A}^{\rm NP}_{\gamma\gamma}(\mathcal{Y}=2)=\mathcal{A}^{\rm NP}_{\gamma\gamma}(\mathcal{Y}=-1)\approx 13.3$. A correlated signal in the γZ channel

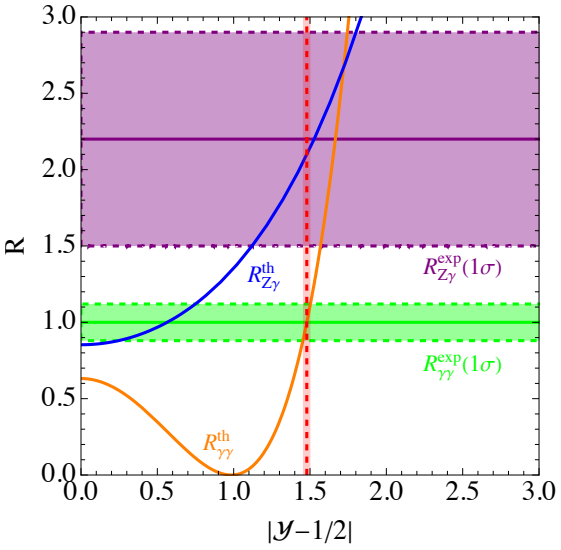

Figure 1.1: $R_{\gamma\gamma}$ and $R_{\gamma Z}$ signal strength in function of the parameter value $\mathcal{Y}$ of the anomalon hypercharges. The shaded areas around the central values represent the 1σ uncertainty bands.

yields $\mathcal{A}^{\rm NP}_{\gamma Z} \approx -\frac{2}{3}c_W[1-(3-8\mathcal{Y}+8\mathcal{Y}^2)t_W^2]$, leading to a large deviation $\mathcal{A}^{\rm NP}_{\gamma Z}(\mathcal{Y}=2) = \mathcal{A}^{\rm NP}_{\gamma Z}(\mathcal{Y}=-1) \approx 2.33$ in the region where the value of $\mathcal{Y}$ is compatible with the di-photon channel. Thus the model with a single Higgs doublet predicts a strong departure of $R_{Z\gamma}$ from its SM value, although extended Higgs sectors can help to tame modifications of Higgs signals (see e.g. [38]). The γZ decay channel of the Higgs has been recently observed both by ATLAS and CMS analysis based on the data from the run-2 [57] and they found $R_{Z\gamma} = 2.2 \pm 0.7$, compatible with the SM within 1.9σ. However the CMS and ATLAS measurement could potentially be a hint of NP and, as it can be seen in Fig.1.1, the central value of their measurements is closed to the prediction of our theory. In the next years HL-LHC is expected to measure $\kappa_{\gamma Z}$ within 10% precision [58] and hence it will confirm or not the central value of the run-2 result.

1.3.3 Direct searches

Direct searches at high-energy particle colliders depend on whether the exotic leptons mix with the SM leptons. In fact, this is possible only for the values $\mathcal{Y} = 0, \pm 1, 2$ (see Table 1.2), including the phenomenologically favored case $\mathcal{Y} = 2, -1$. We discuss in turn the two different scenarios corresponding to $\mathcal{Y} \neq 2, -1$ (stable charged leptons) and $\mathcal{Y} = 2, -1$ (unstable charged leptons) [2].

Stable charged leptons

If $\mathcal{Y} \approx 2, -1$ (but $\mathcal{Y} \neq 2, -1$), no mixing terms are allowed. In this case for each flavor i the heaviest between the $\Psi^{\mathcal{E}_i}$ and $\Psi^{\mathcal{N}_i}$ states decays into the lightest one via CC interactions, which is stable because of exotic lepton number conservation. Charged stable states are cosmologically dangerous and largely excluded unless they are not produced in the early Universe or some mechanism dilutes their abundance. They also provide striking signatures at collider, in terms of charged tracks.

The strongest limit on stable states with $Q = 2e$ is enforced by the ATLAS analysis [59] which searches for stable particles with various choices for their electric charge, ranging from $Q = 2e$ to $Q = 7e$, and specific coupling structure to the $Z-$boson. They consider production via both DY

and photon-fusion interactions at $\sqrt{s} = 13$ TeV with 139 fb^{-1} of integrated luminosity. By properly taking into account the different coupling structure of the model we are investigating with respect to the one assumed by the ATLAS analysis, one obtains a limit $m_{\mathcal{E}_i} \gtrsim 1030$ GeV for a single flavor of doubly charged exotic leptons. This limit increases to ~ 1140 GeV for two degenerate doubly charged exotic leptons.

This analysis do not consider the case of singly charged heavy leptons with $Q = e$. In the scenario where this state is the lightest present in the spectrum, the strongest limit is set by the CMS analysis [60], performed at $\sqrt{s} = 13$ TeV with 3.2 fb^{-1} of integrated luminosity. By recasting the CMS results one obtains a limit $m_{\mathcal{N}_i} \gtrsim 540$ GeV, with the available data set for a single flavor of singly charged exotic lepton, limits that increases to ~ 630 GeV, for two degenerate singly charged exotic leptons. By projecting the results of this analysis to an integrated luminosity of 139 fb^{-1}, corresponding to the luminosity of the ATLAS search for doubly charged leptons, these limits increase to 820 GeV and 930 GeV respectively.

Unstable charged leptons

For $\mathcal{Y} = 2, -1$ the electroweak anomalons have electric charge $Q = 2, -1$ ($\mathcal{N}$ components) and $Q = 1, -2$ ($\mathcal{E}$ components). The $|Q| = 2$ states can decay into a W and a $|Q| = 1$ fermion, while the latter can mix with SM leptons and decay into $Z\ell$ or $h\ell$. The experimental measurements on the Z couplings to leptons [61] requires that the mixing angle between SM and anomalons to be $\lesssim \mathcal{O}(10^{-3})$. The constraints coming from lepton flavour violating decays $Z \to e\mu, \mu\tau, \tau e$, which are generated from the same mixing terms, are estimated to be of the same order. Let us consider $\mathcal{Y} = -1$ (the other can be obtained by charge conjugation) and denote the mass eigenstates as $\Psi^{\mathcal{E}_{1,2}}$ and $\Psi^{\mathcal{N}_{1,2}}$. The charged current interaction yields that doubly charged promptly decay, for mixing angles $\gtrsim 10^{-7}$, into a final state with a same-sign (SS) lepton pair via

$$\Psi^{\mathcal{E}_i} \to W^- \ell^- \to \ell^- \ell^- \not{E}_T \ . \tag{1.52}$$

Final states with SS leptons have small SM backgrounds.

No direct searches for doubly charged lepton exist. There exist however an ATLAS analysis targeting pair-produced doubly charged scalars decaying into a SS lepton pair, performed at $\sqrt{s} = 13$ TeV with 36.1 fb^{-1} of integrated luminosity [62]. In order to recast this analysis we have implemented the model into the `Feynrules` [63] package using the `UFO` [64] format in order to perform a simulation with `MadGraph` [65]. The ATLAS search defines 8 mutually exclusive signal regions (SRs), each them featuring (at least) one SS lepton pair, categorizing them with respect to lepton multiplicity and flavor.

From the measured number of events in each signal region and the estimation of the SM background we estimate the *observed* number of signal events excluded at 95% confidence level (CL) via the CLs procedure [66, 67]. Projections for for higher integrated luminosities are obtained by extrapolating the *expected* 95% CL exclusion. A summary of the exclusion yields are reported in Tab. 1.3 for the various SRs defined by the ATLAS search.

We then consider the pair-production of both the doubly charged leptons $pp \to \bar{\Psi}^{\mathcal{E}_{1,2}} \Psi^{\mathcal{E}_{1,2}}$ and study the limits obtained from the recast of the ATLAS search [62], under various assumptions for the flavor mixing pattern of the exotic leptons. For concreteness we study two scenarios. In the former both the exotic fermions only mix with the first two generations of SM leptons with equal weights, thus $\mathrm{BR}(\Psi^{\mathcal{E}_{1,2}} \to W^- e^-) = \mathrm{BR}(\Psi^{\mathcal{E}_{1,2}} \to W^- \mu^-) = 50\%$. In the latter we assume them to democratically mix with all the three SM lepton families $\mathrm{BR}(\Psi^{\mathcal{E}_{1,2}} \to W^- e^-) = \mathrm{BR}(\Psi^{\mathcal{E}_{1,2}} \to W^- \mu^-) = \mathrm{BR}(\Psi^{\mathcal{E}_{1,2}} \to W^- \tau^-) = 1/3$. The strongest exclusion limits come in both cases from SRs with three leptons and are shown in Fig. 1.2 for the actual luminosity of the ATLAS search $\mathcal{L} = 36.1$ fb^{-1} as well as for two projected benchmark values, $\mathcal{L} = 300,\ 3000$ fb^{-1}. Current limits in the first scenario are around 500 GeV, if one of the two exotic lepton is decoupled from the spectrum,

Signal region	$N_{\rm obs}$	$N_{\rm bkg}$	$N_{\rm obs}^{95\%CL}$	$N_{\rm exp}^{95\%CL}$
$e^\pm e^\pm$	132	160±14	23.4	39.0
$e^\pm \mu^\pm$	106	97.1±7.7	33.7	27.1
$\mu^\pm \mu^\pm$	26	22.6±2.0	15.1	12.4
$e^\pm e^\pm e^\mp$	11	13.0±1.6	8.1	9.7
$e^\pm \mu^\pm \ell^\mp$	23	34.2±3.6	8.6	16.0
$\mu^\pm \mu^\pm \mu^\mp$	13	13.2±1.3	9.4	10.2
$\ell^\pm \ell^\pm \ell'^\mp$	2	3.1±1.4	4.9	7.0
$\ell^\pm \ell^\pm \ell^\mp \ell^\mp$	1	0.33±0.23	4.2	4.2

Table 1.3: Number of observed events in the various signal region of the ATLAS search [62], together with the SM background expectation. The observed and expected number of excluded signal event is computed via the CLs procedure [66, 67].

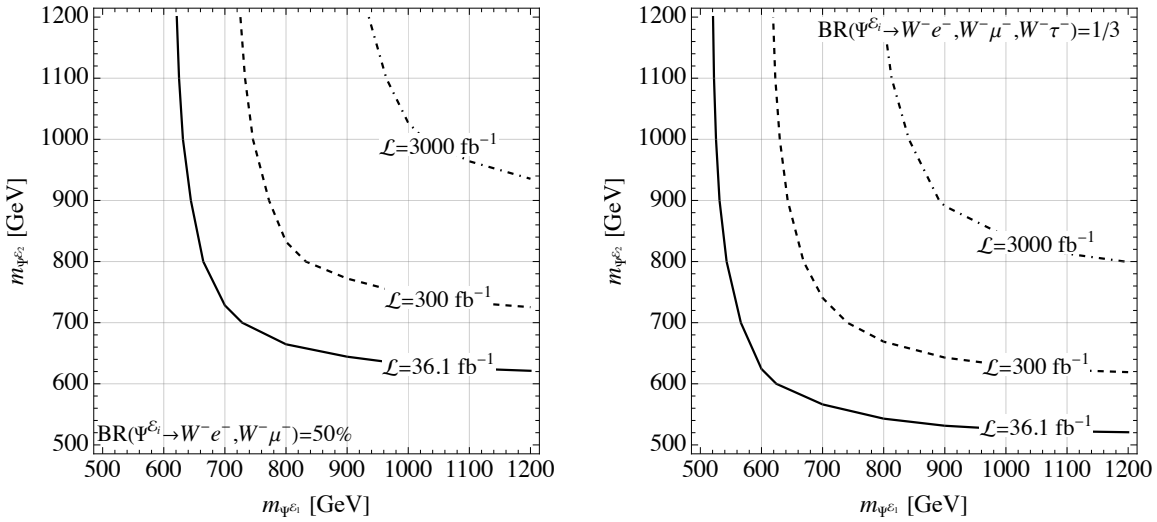

Figure 1.2: 95% CL exclusion limits obtained from the LHC ATLAS search [62], solid line. The dashed and dot-dashed lines show the projected exclusion with $300, 3000\text{fb}^{-1}$ of integrated luminosity. In the left panel we assume exclusive mixing with the first two generation of SM leptons with equal weights, $\text{BR}(\Psi^{\mathcal{E}_{1,2}} \to W^- e^-) = \text{BR}(\Psi^{\mathcal{E}_{1,2}} \to W^- \mu^-) = 50\%$. In the right panel we assume them to democratically mix with all the three SM lepton families $\text{BR}(\Psi^{\mathcal{E}_{1,2}} \to W^- e^-) = \text{BR}(\Psi^{\mathcal{E}_{1,2}} \to W^- \mu^-) = \text{BR}(\Psi^{\mathcal{E}_{1,2}} \to W^- \tau^-) = 1/3$.

reaching ~ 600 GeV if the two states are mass degenerate. At the end of the high luminosity phase of the LHC, values up to $m_{\Psi^{\mathcal{E}_{1,2}}} \simeq 1$ TeV could be tested. Allowing for a mixing with the τ lepton, relaxes these limits of $\mathcal{O}(100$ GeV) given that this final state is not directly targed by the analysis [62], and is anyway expected harder to be tested.

Turning our attention to the $Q = e$ anomalon states, they promptly decay, for mixing angles $\gtrsim \mathcal{O}(10^{-7})$, as

$$\Psi^{\mathcal{N}_i} \to W^- \nu \, , Z \ell^- \, , \tag{1.53}$$

where the branching ratio of each channel is a function of the model parameters. The experimental signature depends on how the W or Z boson decays and in particular signatures as in Tab. 1.3 are possible. The inclusion of the $\Psi^{\mathcal{N}_i}$ decay modes would then increase the constraints from direct searches but it requires a less straightforward analysis than the double charged states. We choose

to be conservative and rely on the constraints we already obtained in Fig. 1.2 since the take-home message, that we are beyond the edge of perturbativity, would not substantially change.

1.3.4 Perturbative unitarity

In the previous section we have shown that current LHC limits pushes the exotic leptons to have a mass $\gtrsim 500 - 600$ GeV, depending on the flavor structure of the model, in the case that they mix with the SM fermions. In case of no SM-BSM mixing these limits might be pushed to higher values, from the null results for searches of heavy-stable charged particles.

Given that the exotic fermions are chiral states which acquire their mass only via their couplings to the Higgs boson, the model Yukawa $y_{1,2,3,4}$ attain large values, possibly at the edge of the perturbative regime of the theory. In order to quantify this statement we apply the procedure shown in [68] and compute the perturbative unitarity bounds obtained by considering all the $2 \to 2$ scatterings present in the model. The strongest limit is obtained in the $J = 0$ partial wave and, working for simplicity in the custodial limit $y_1 = \tilde{y}_3$, $y_2 = \tilde{y}_4$, reads

$$3y_1^2 + 3y_2^2 + \sqrt{9y_1^4 - 2y_1^2 y_2^2 + 9y_2^4} < 16\pi \ . \tag{1.54}$$

This can be then translated into a perturbative limit on the exotic fermion masses, which fixes $m_{\Psi^{\varepsilon_{1,2}}} \lesssim 400$ GeV. This shows that current LHC exclusion already push the model beyond the edge of perturbativity.[6]

1.4 Unbroken symmetry in the Stückelberg scenario

In the previous section we consider the presence of an exotic Higgs field $\mathcal{S}$ in order to break the new symmetry and give mass to the gauge vector boson. A different scenario appears if the $\mathcal{X}$ field acquires its mass with a Stückelberg mechanism.

1.4.1 Brief introduction to the Stückelberg mechanism

Consider a theory with abelian gauge symmetry $\mathrm{U}(1)_X$ and corresponding gauge boson $\mathcal{X}_\mu$, whose UV Lagrangian is given by

$$\mathcal{L}_{\mathrm{U}(1)_X} = \sum_i (D_\mu \phi_i)^\dagger (D^\mu \phi_i) - V(\phi_i) + \sum_i \bar{\Psi}_i i \not{D} \Psi_i + \mathcal{L}_{\text{Yukawa}} - \frac{1}{4} \mathcal{X}_{\mu\nu} \mathcal{X}^{\mu\nu} \,, \tag{1.55}$$

where ϕ_i and Ψ_i denote the scalar and fermion fields of the theory and the covariant derivative is defined as usual, $D_\mu \phi_i = (\partial_\mu - i g_X X_{\phi_i} \mathcal{X}_\mu)\phi_i$ and $D_\mu \Psi_i = (\partial_\mu - i g_X X_{\Psi_i} \mathcal{X}_\mu)\Psi_i$. Under a $\mathrm{U}(1)_X$ transformation

$$\mathcal{X}_\mu \to \mathcal{X}_\mu + \partial_\mu \alpha(x) \,, \tag{1.56}$$

$$\phi_i \to e^{i g_X X_{\phi_i} \alpha(x)} \phi_i \,, \tag{1.57}$$

$$\Psi_i \to e^{i g_X X_{\Psi_i} \alpha(x)} \Psi_i \,. \tag{1.58}$$

Note that gauge invariance does not allow to write a mass term for the gauge field, leaving the $\mathcal{X}_\mu$ massless. However, following Stückelberg's trick [69, 70], one could introduce an extra physical

[6] Large higher-order corrections (starting at two loops) are then expected for Higgs decays and they might slightly change the solutions $\mathcal{Y} \approx 2, -1$.

scalar field π to describe covariantly the three polarizations of a massive vector field and write

$$\mathcal{L}_{\rm St} = \mathcal{L}_{{\rm U}(1)_X} + \frac{1}{2} m_{\mathcal{X}}^2 \left(\mathcal{X}_\mu - \frac{\partial_\mu \pi}{m_{\mathcal{X}}} \right)^2 . \tag{1.59}$$

The scope of the Stückelberg field is to restore the gauge symmetry, which would be broken by the mass term, and make it manifest. Under a $\mathrm{U}(1)_X$ transformation

$$\pi \to \pi + m_X \alpha(x) \,, \tag{1.60}$$

which is essential to make the mass term gauge invariant. The five degrees of freedom of $\mathcal{X}_\mu$ and π fields are then reduced by the gauge symmetry to the three physical polarization states of massive spin-1 boson.

The Stückelberg model relies on the peculiarity that the Stückelberg field is not interacting[7], thus adding a mass m_X for a $\mathrm{U}(1)_X$ gauge boson does not spoil renormalizability of the theory. This should be compared with the non-abelian case where adding the mass leads to a high energy inconsistency or equivalently to a cutoff determined by the coupling g_X of order $\Lambda \sim m_X/g_X$; the theory requires a completion not far above the mass of the particle and/or the introduction of new physical degrees of freedom, see the discussion at the beginning of [71]. In a similar way, a mass term for the fermions via a non-linear Yukawa-like interaction

$$\bar{\Psi}\Psi' e^{i g_X (X_\Psi - X_{\Psi'})\pi/m_X} \,, \tag{1.61}$$

even if gauge invariant, would spoil renormalizability and hence are not allowed.

In addition to (1.59), one introduces a gauge-fixing term with the usual Faddeev and Popov techniques [72] and the Stückelberg's Lagrangian for real vector fields, complemented with ghost terms, is actually BRST invariant [73–75]. The BRST symmetry facilitates considerably the effort to prove the perturbative renormalizability and the unitary of the theory [76–78].

A common choice of the gauge-fixing term is the t' Hooft gauge

$$\mathcal{L}_{gf} = -\frac{1}{2\xi} \left(\partial_\mu \mathcal{X}^\mu + \xi m_X \pi \right)^2 \tag{1.62}$$

with ξ being a free gauge parameter which the physics is independent of. Then the propagators of the $\mathcal{X}_\mu$ and π fields are

$$\Delta_{\mathcal{X}}^{\mu\nu}(q) = \frac{i}{q^2 - m_X^2} \left[-g^{\mu\nu} + (1-\xi) \frac{q^\mu q^\nu}{q^2 - \xi m_X^2} \right] , \tag{1.63}$$

$$\Delta_\pi(q) = \frac{i}{q^2 - \xi m_X^2} \tag{1.64}$$

and the Stückelberg field turns out to be a free field with no need of renormalization. For this particular choice of the gauge, the ghost fields decouple from the theory. For $\xi = 1$ (Feynman gauge), the high energy behavior of the vector field propagator goes like $-ig^{\mu\nu}/q^2$, so the Stückelberg theories are power–counting renormalizable (being also unitary). Note that in the $\xi \to \infty$ one recovers the unitary gauge which is nothing else that the Proca formulation of a massive vector boson [79]. Hence, the Stückelberg mechanism consists in the introduction of new fields to reveal a symmetry of a gauge–fixed theory [80] and does not provide at all any spontaneously symmetry breaking dynamics.

[7] A similar feature appears in the spontaneous symmetry breaking of U(1) global symmetries at leading order in the derivative expansion of the corresponding Goldstone boson.

1.4.2 Unbroken accidental symmetries

Noted that the Stückelberg mechanism does not break the gauge symmetry but it just gives mass to the relative gauge boson, we are left with an unbroken gauge symmetry. Let us rewrite

$$X = \alpha_{B+L}(B+L) + \alpha_{B-L}(B-L) + \alpha_{e\mu}(L_e - L_\mu) + \alpha_{\mu\tau}(L_\mu - L_\tau) \tag{1.65}$$

and consider the a few benchmark scenarios

- $X = B + L$

  The anomalons need to be charged under the electroweak group and, moreover, they need to be chiral either under the $\mathrm{U}(1)_X$ or the SM gauge group (otherwise they cannot cancel the $\mathrm{U}(1)_X\mathrm{SM}^2$ anomalies). In either cases it is not possible to write down a vector-like bare mass term $\bar{\Psi}\Psi'$, neither they can pick up mass via the VEV of a scalar field that breaks the $\mathrm{U}(1)_X$, since in the Stückelberg approach the gauge symmetry remains unbroken. This possibility is marginally allowed by Higgs signals and direct searches, and it will be decisively tested at the HL-LHC via the measurement of $h \to \gamma Z$. However, direct searches push us to the edge of perturbativity of the Yukawa couplings.

- $X = \alpha_{e\mu}(L_e - L_\mu) + \alpha_{\mu\tau}(L_\mu - L_\tau)$

  Here we do not need to introduce new fermions beyond the SM in order to cancel gauge anomalies. However, this case is ruled out by neutrino oscillations, i.e. by the fact some entries in the neutrino mass matrix are forbidden and PMNS mixing is trivial. In other words, $L_i - L_j$ cannot be an exact symmetry of the SM.

- $X = B - L$

  We need to introduce 3 RH neutrinos in order to cancel $\mathrm{U}(1)_X$-gravity and $\mathrm{U}(1)_X^3$ anomalies. However, the RH neutrinos cannot pick-up a vector-like mass and hence we predict Dirac neutrinos. This is consistent with the fact that the $\mathrm{U}(1)_X$ remains unbroken. Note the orthogonal case of the $\mathrm{U}(1)_X$ realized à la Higgs where the $B - L$ is spontaneously broken and one predicts Majorana neutrinos. An unbroken $B - L$ scenario with Stückelberg mass has been studied in [81] where the author highlights in particularly that successful Big Bang nucleosynthesis provides strong bounds for masses $10\ \mathrm{eV} < m_{\mathcal{X}} < 10\ \mathrm{GeV}$ due to resonant enhancement of the rate $f\bar{f} \leftrightarrow \nu_R\bar{\nu}_R$.

1.5 Summary

In this chapter we have revisited the case of light vector bosons coupled to anomalous currents which are UV completed by new anomaly-canceling heavy fermions (anomalons). After the latter have been integrated out, WZ terms of the type in Eq. (1.21) are generated. On the one hand, they take care of anomaly cancellation in the IR and, on the other, they source the energy-enhanced emission of longitudinally polarized vectors, $\mathcal{X}$, which typically results in very strong bounds on $g_X/m_{\mathcal{X}} \propto 1/v_X$ whenever the decay channels $Z \to \gamma\mathcal{X}$, $B \to K\mathcal{X}$, $K \to \pi\mathcal{X}$, etc, are kinematically open [14,15]. Here, we have studied the model-dependence of such bounds, considering as a paradigmatic framework the gauging of the most general (anomalous) linear combination of SM global symmetries, $\mathrm{U}(1)_X$, with the generator X given in Eq. (1.1). To this end, we provided a UV completion including electroweak anomalons $\mathcal{L} + \mathcal{E} + \mathcal{N}$ (cf. Table 1.1) to cancel $\mathrm{U}(1)_X$ anomalies in combination with electroweak gauge factors and RH neutrinos to take care of $\mathrm{U}(1)_X$ anomalies in isolation when the lepton number generators are gauged. An extra scalar $\mathcal{S}$ provides the spontaneous breaking of the $\mathrm{U}(1)_X$ factor and gives mass to the vector $\mathcal{X}$. Then, we have computed the EFT of a light $\mathcal{X}$

when the heavy anomalons are integrated, keeping in general both electroweak symmetry breaking and preserving sources for the mass of the anomalons (see App. A for details). This allowed us to conclude (cf. e.g. Eq. (1.39)) that the bounds mentioned above on light $\mathcal{X}$ can be evaded in the limit where the mass of the electroweak anomalons comes mostly from the Higgs VEV. This condition can be neatly imposed in terms of $\mathrm{U}(1)_X$ gauge charges (so that the operators in Eq. (1.7) are allowed while those in Eq. (1.15) are forbidden) or parametrically by decoupling the vector-like masses of the exotic leptons by taking a small Yukawa and/or a small VEV for $\mathcal{S}$. On the other hand, mostly chiral exotic leptons (receiving their mass mostly from the Higgs VEV) are strongly constrained due to their non-decoupling nature by electroweak-scale phenomenology, in particular Higgs couplings and direct searches. We have reviewed in Sect. 1.3 those constraints, based on the previous analyses in [37, 38], and argued that it is possible to evade $h \to \gamma\gamma$ bounds for $\mathcal{Y} \approx 2, -1$ (including the exact cases $\mathcal{Y} = 2, -1$ allowing for mixings between anomalons and SM leptons, cf. Table 1.2). For $\mathcal{Y} \approx 2, -1$, the $h \to \gamma Z$ channel differs $\mathcal{O}(1)$ from the SM and it is in agreement with the recent measurement from ATLAS and CMS [57]. Direct searches, whose signatures depend on whether the electroweak anomalons mix or not with the SM leptons, are also very stringent and they practically push the present model beyond the edge of perturbativity.

Chapter 2

Probing right-handed neutrinos dipole operators

2.1 Introduction and framework

The see-saw mechanism [16, 17, 82–84] is arguably the simplest extension of the SM that is able to explain the observed pattern of neutrino masses and oscillations. In its simplest incarnation, it consists in adding to the SM particle content a right-handed neutrino, that is a spin 1/2 fermion, singlet under the SM gauge group, which has a Yukawa interaction with SM leptons, as well as a Majorana mass term. One of the active neutrinos acquire thus a non-vanishing mass m_ν and a mixing θ with the new sterile state, parametrically expressed by the relations

$$m_\nu \simeq \frac{y_\nu^2 v^2}{m_N} , \qquad \theta \simeq \sqrt{\frac{m_\nu}{m_N}}, \tag{2.1}$$

where y_ν and m_N are the RH neutrino Yukawa interaction and mass respectively and v is the electroweak (EW) vacuum expectation value (VEV). Since experimental data point to at least two massive neutrinos, at least two RH states must be added to obtain a realistic phenomenology. In this case the essence of the see-saw mechanism is unaltered, with the obvious promotion of y_ν and m_N to matrices in flavor space, but the relations of Eq. (2.1) turn out to be modified. In particular the mixing angles can receive an *exponential enhancement* with respect to the naive see-saw scaling case, that may drastically modify the phenomenology. This is best seen in the Casas-Ibarra parametrization [85]. From the practical point of view, this means that masses and mixings can be treated as independent parameters. Irrespective of this consideration, by fixing m_ν Eq. (2.1) doesn't uniquely point to a preferred mass range for m_N, which could lie all the way up the grand unification scale if y_ν is an $\mathcal{O}(1)$ parameter. However, in recent years RH neutrinos with mass below the EW scale have gained more and more attention in that they can explain the matter-antimatter asymmetry of the Universe via neutrino oscillations [86, 87] and, crucially, can be tested at present and future colliders and fixed-target experiments, see e.g. [88–114].

While the see-saw model is a full-fledged UV complete theory, at least in the same way as the SM is, in the case where RH neutrinos lie at the EW scale it is interesting to consider it as a low energy EFT extended with higher dimensional operators built from the SM and the RH neutrino fields. The resulting theory is called νSMEFT and is described by the following Lagrangian

$$\mathcal{L} = \mathcal{L}_{\rm SM} + i\bar{N}\partial\!\!\!/ N - \bar{L}_L Y_\nu \tilde{H} N - \frac{1}{2}\bar{N}^c M_N N + \sum_{n>4} \frac{\mathcal{O}^n}{\Lambda^{n-4}} + h.c. , \tag{2.2}$$

where N is a vector describing $\mathcal{N}_f$ flavors of RH neutrino fields and $N^c = C\bar{N}^T$, with $C = i\gamma^2\gamma^0$. Furthermore, Y_ν is the $3 \times \mathcal{N}_f$ Yukawa matrix of the neutrino sector with $\tilde{H} = i\sigma^2 H^*$, M_N is a $\mathcal{N}_f \times \mathcal{N}_f$ Majorana mass matrix for the RH neutrinos and $\mathcal{O}^n$ the Lorentz and gauge invariant operators with dimension n built out from the SM and the RH neutrino fields, with Λ parametrizing the Wilson coefficient of the operator. A complete and independent set of operators has been built up to dimension nine [20, 115, 116]. Interestingly, already at $d = 5$ two genuine νSMEFT operators appear[1]. The first is an operator coupling the RH neutrinos with the Higgs boson, $\mathcal{O}^5_{NH} = \bar{N}^c N H^\dagger H$. This triggers a new decay mode for the Higgs, with interesting consequences for collider phenomenology, both at the Large Hadron Collider (LHC) [18,19,117,118] and future colliders [119]. The second operator is a dipole with the hypercharge gauge boson[2] $\mathcal{O}^5_{NB} = \bar{N}^c \sigma^{\mu\nu} N B_{\mu\nu}$, which has so far been less investigated [21,119–123][3]. Among other effects, this operator generates the decay[4]

$$N_{\text{heavy}} \to N_{\text{light}} + \gamma \ , \quad m_{N_{\text{heavy}}} > m_{N_{\text{light}}} . \tag{2.3}$$

This interaction is the subject of our study. Our focus will be on light RH neutrinos with masses up to a few GeV. Such light states can be produced not only at high energy colliders via parton interactions, but also at fixed-target experiments, typically via meson decay. More specifically, we will analyze in detail the current bounds from colliders experiments, such as LHC, LEP and BaBar, and fixed-target experiments, such as CHARM [128], NuCal [129,130] and NA64 [131]. We will then compute the predicted sensitivity to the νSMEFT parameter space of the proposed experiments ANUBIS [132] , CODEX-b [133–135], FACET [136], FASER 2 [137, 138], MAPP [139, 140] and SHiP [141, 142]. In addition, we will also discuss constraints from cosmology and astrophysics.

Throughout this work we will consider the theory of Eq. (2.2), focusing on the $d = 5$ dipole operator. Given its symmetry properties, this operator is non-vanishing only for $\mathcal{N}_f \geq 2$. Since we are primarily interested in probing the effect of the dipole operator, we will work under the assumption that the active-sterile mixing effects are negligible for what concerns the *heavier* sterile neutrinos phenomenology, in such a way that their decay proceeds only via the dipole operator under our scrutiny through the process of Eq. (2.3). As for the lightest RH neutrino N_1, its decay pattern is completely determined by the active-sterile mixing, as in the standard see-saw case. As we are going to discuss in Sec. 2.3, the N_1 lifetime can be strongly constrained by cosmological observations, especially the ones related to the epoch of Big Bang Nucleosynthesis (BBN). A relatively safe scenario is the one in which N_1 mixes dominantly with the third generation of SM neutrinos, ν_τ. We found that this configuration can be easily obtained by choosing $\mathcal{N}_f = 3$, satisfying at the same time all other relevant constraints. Interestingly, in this case the heaviest RH neutrinos N_3 can be decoupled from the spectrum without affecting the mixing pattern for N_1, leaving only the two lightest RH neutrinos $N_{1,2}$ as dynamical states. In presenting our main findings we will thus consider a framework with only these two states living at the EW scale and interacting via the dipole operator which we normalize as

$$\mathcal{O}^5_{NB} = \frac{g_Y}{16\pi^2} \frac{e^{i\alpha}}{\Lambda} \bar{N}^c_1 \sigma^{\mu\nu} N_2 B_{\mu\nu} + h.c. \ , \tag{2.4}$$

where $m_{N_2} > m_{N_1}$, and where g_Y and $B_{\mu\nu}$ are the $U(1)_Y$ coupling and field strength tensor respectively. The loop suppression factor is explicitly introduced since this operator only arises at loop level in any weakly coupled UV completion, see *e.g.* [143, 144], while the hypercharge coupling

[1] The other $d = 5$ operator is clearly the Weinberg operator $\mathcal{O}^5_W = (\bar{L}^c \tilde{H}^*)(\tilde{H}^\dagger L)$.

[2] We define $\sigma^{\mu\nu} = i[\gamma_\mu, \gamma_\nu]/2$.

[3] Recent works on the phenomenology of d=6 operators involving sterile neutrinos at accelerators are [113, 114, 124–127]

[4] Given the mass range that we consider, the decay process in which the γ is substituted with a Z boson is kinematically closed.

is added because of the presence of $B_{\mu\nu}$. Explicit UV completions include models with additional scalar and fermions or models with additional vectors and fermions, with non-vanishing hypercharge [21,145]. We will comment later on possible strongly interacting UV completions. Since the Wilson coefficient can be complex, we show explicitly its phase α. In this scenario, $\mathcal{O}^5_{NB}$ completely governs the RH neutrinos phenomenology[5]. In particular, it dictates the heaviest neutrino N_2 total decay width. For RH neutrinos below the Z mass the dominant decay mode is $N_2 \to N_1\gamma$ whose rate reads

$$\Gamma(N_2 \to N_1\gamma) = \frac{{g_Y}^2}{(16\pi^2)^2}\frac{c_w^2}{2\pi}\frac{m_{N_1}^3}{\Lambda^2}\delta^3\left(\frac{2+\delta}{1+\delta}\right)^3 \simeq \frac{g_Y^2}{64\pi^5}c_w^2\frac{m_{N_1}^3}{\Lambda^2}\delta^3 \ , \tag{2.5}$$

where c_w is the cosine of the Weinberg angle and the last equality holds for small values of δ, which is defined as

$$\delta = \frac{m_{N_2} - m_{N_1}}{m_{N_1}} \ . \tag{2.6}$$

The three-body decay into an off-shell Z boson provides a subdominant contribution. As it is clear from Eq. (2.5), the relative mass splitting δ is crucial in determining the RH neutrino decay length, and hence its lifetime. This gives an indication on the type of experiments that can have a sensitivity to this scenario, depending on how far the detector is located with respect to the N_2 production points. For example the neutrinos N_2 could decay promptly, *i.e.* with a typical decay length smaller than $\mathcal{O}$(mm). In this case they are a primary target for standard collider searches. Their lifetime could also be longer, with corresponding decay lengths in the $\mathcal{O}(1\text{ m} - 100\text{ m})$, for which different strategies need to be envisaged. In the more extreme case, they can be stable with respect to the length scale of any terrestrial experiment and hence completely invisible for what concerns laboratory searches. We will comment upon all these possibilities in the following, mainly focusing however on a region of parameter space in which the heavier neutrino N_2 is a long-lived state with a macroscopic decay length. This choice has a twofold motivation. From one side, light new states with suppressed interactions, as the one inherited from the dipole operator, have usually a long lifetime. From the other side, the study of long-lived particles is an active field which has received a lot of attention in the last years, following the philosophy of *leaving no stones unturned* and *lighting new lampposts* in the quest of new physics beyond the SM. In this area, big experimental progresses are foreseen in the mid- and short-term.

The relative mass splitting is also important in determining the photon energy arising from the decay of Eq. (2.3). From basic kinematics in the N_2 rest frame one has

$$E_\gamma^{\rm com} = m_{N_2}\frac{\delta}{2}\frac{2+\delta}{(1+\delta)^2} \ . \tag{2.7}$$

Assuming the photon to be produced collinearly with the direction of N_2 in the laboratory frame, which maximizes the photon energy in this frame of reference, one has

$$E_\gamma^{\rm lab} = \left(P_{N_2} + \sqrt{m_{N_2}^2 + P_{N_2}^2}\right)\frac{\delta}{2}\frac{2+\delta}{(1+\delta)^2} \simeq 2P_{N_2}\delta \ , \tag{2.8}$$

where P_{N_2} is the modulus of the N_2 spatial momentum and the last equality holds for $m_{N_2}/P_{N_2} \ll 1$ and $\delta \ll 1$[6]. Thus the smaller the relative mass splitting the softer the final state photons, which

[5] Our analysis focuses on the radiative decays of N_2 induced by the dipole operator but, of course, additional signals at the experiments under study could be produced by N_1 decays, if the mixing with the active sector is not too suppressed.

[6] Notice that, for vanishing active-sterile mixing, in the $\delta \to 0$ limit the mass term in Eq. (2.2) becomes symmetric under a global SO(2) symmetry that acts on the vector $N = (N_1, N_2)^T$. It is thus technically natural to have small δ.

however should satisfy some minimal threshold requirement in order to be identified in a detector. Hence too small relative mass splittings will hardly be experimentally testable.

The rest of the chapter is organized as follows. In Sec. 2.2 we report useful formulæ for computing the decay of a QCD meson into a pair of RH neutrinos via the dipole operator. In Sec. 2.3 we review the existing limits on the dipole operator from cosmology, colliders and other type of experiments, while in Sec. 2.4 we discuss the future sensitivity of SHiP and FASER 2 on the model parameter space, wrapping up our conclusion in Sec. 2.5.

2.2 Mesons decay into RH neutrinos

For the decay $V \to N_1 N_2$ we need the following matrix element:

$$\langle 0|\bar{q}\gamma^\mu q|V(p)\rangle = f_V^q \, m_V \, \epsilon^\mu(p), \tag{2.9}$$

where m_V is the vector meson V mass, $\epsilon^\mu(p)$ its polarization vector and explicit expressions for the coefficients f_V^q can be found in Appendix A of [146]. Given the range of masses to which we are interested, in our computation we will consider only photon exchange. The explicit expression for the decay width is given by

$$\Gamma(V \to N_1 N_2) = \frac{g_Y^2}{(16\pi^2\Lambda)^2} \frac{(c_w \, Q_q \, e \, f_V^q)^2 m_V}{6\,\pi} \left(1 - \frac{(m_{N_2} - m_{N_1})^2}{m_V^2}\right)^{1/2} \left(1 - \frac{(m_{N_2} + m_{N_1})^2}{m_V^2}\right)^{1/2} \left(1 + \frac{m_{N_1}^2 + m_{N_2}^2 - 6 m_{N_1} m_{N_2} \cos(2\alpha)}{m_V^2} - 2\frac{(m_{N_2}^2 - m_{N_1}^2)^2}{m_V^4}\right), \tag{2.10}$$

where c_w is the cosine of the weak angle, Q_q the electric charge of quark q, in units of the electron's electric charge e. To produce our plots we set $\alpha = \pi/2$ to maximize the number of events, although the results remain qualitatively the same for other choices of the phase.

2.3 Current limits from cosmology, colliders and other experiments

The parameter space of the simplified scenario considered in this work is spanned by the lighter neutrino mass m_{N_1}, the relative mass splitting δ with the heavier RH neutrino, and the Wilson coefficient of the dipole operator, parametrized by Λ and its phase α. This parameter space is already constrained by laboratory data from colliders and past beam dump experiments, as well as by astrophysical and cosmological measurements. In this section we will review the most important and stringent ones. Particular care must be taken in ensuring the validity of the EFT in the various considered processes. The dipole operator in Eq. (2.4) induces $N_1 N_2$ production through the exchange of a photon or a Z boson. Following Ref. [147] and assuming couplings of order one, we identify the EFT cut-off scale with Λ, and for the EFT to be valid we require

$$\sqrt{\hat{s}} < \Lambda, \tag{2.11}$$

where $\hat{s} = (p_{N_1} + p_{N_2})^2$ is the Lorentz invariant energy that enters the vertex. One important production mechanism for light $N_{1,2}$ is via heavy meson decay, that can be copiously produced in fixed-target experiments. In this case the heavy neutrino production proceeds via an s-channel γ and we have $\hat{s} = m_M^2$, with m_M the meson mass. For higher masses direct production at collider can be relevant. In this case, $\hat{s}$ is the center of mass energy squared of the parton pair that exchange the photon or the Z boson, *e.g.* e^+e^- for LEP or $q\bar{q}$ for the LHC. Analogous considerations apply for other production modes, as for example production via photon bremsstrahlung.

2.3.1 Fixed-target experiments

We start our discussion with fixed-target experiments, for which we have considered data collected at CHARM [128], NuCal [129, 130] and NA64 [131]. We consider the production of RH neutrinos from the decay $M \to N_1 N_2$, with M a vector meson produced at these experiments. [7]

CHARM: In the CHARM experiment, a 400 GeV proton beam was dumped on a copper target. The detector, placed at a distance of 480 m from the interaction point (IP) and 5 m off the beam axis, consisted of a decay volume 35 m long and with a surface area of 9 m^2. We have modeled the detector following [148] and recast the analysis of [128], in which an axion-like particle (ALP) decaying into a pair of photons was searched for. Since the analysis required only a single electromagnetic shower, it can be applied to the decay $N_2 \to N_1 \gamma$. We compute the number of events expected at CHARM following the equations that will be described in more details in Sec. 2.4, see Eq. (2.13) and subsequent ones. In our analysis, we simulate the production of $N_1 N_2$ pairs from the decay of the mesons ρ, ω, J/Ψ and Υ using `PYTHIA 8.3` [149,150], finding the following production multiplicities: $N_\rho = 0.58$, $N_\omega = 0.57$, $N_{J/\Psi} = 4.7 \times 10^{-6}$ and $N_\Upsilon = 2.2 \times 10^{-9}$, see Sec. 2.4 for their definition. Then, we require the energy of the photon in the laboratory frame to satisfy $E_\gamma \geq 1$ GeV and, following [128], we take a signal acceptance of 51%. The number of protons-on-target (POT) is taken to be $N_{\rm POT} = 2.4 \times 10^{18}$. Since no signal events were observed in the search of [128], we set an upper limit at 95% confidence level (CL) of $N_{\rm signal} = 3$. The region excluded by the CHARM experiment is shown in Fig. 2.1 , 2.2 and Fig. 2.3.

NuCal: In the ν-calorimeter I experiment (NuCal), a 70 GeV proton beam from the U70 accelerator was dumped on an iron target. The detector consisted of a cylindrical decay volume 26 m long and with a diameter of 2.6 m, placed at 64 m from the iron target. We implement such geometry accepting N_2 events with a maximum angle of 0.014 rad from the beam axis. To set a limit on the parameter space of our scenario, we simulate $N_1 N_2$ production from ρ and ω decays[8] using `PYTHIA 8.3` obtaining the following production multiplicities: $N_\rho = 0.30$, $N_\omega = 0.30$. Then, we follow the analysis in [151], requiring the photons produced in the $N_2 \to N_1 \gamma$ decay to satisfy two conditions: their energy in the laboratory frame must be $E_\gamma \geq 3$ GeV, while their angle with respect to the beam axis must satisfy $\theta_\gamma < 0.05$ rad. After these selection cuts, 5 events were observed, with an estimated background of 3.5 events from the simulated neutrino interactions in the detector [129]. Given these numbers, assuming Poisson likelihood we set a 95% CL upper limit of $N_{\rm signal} \sim 7.1$ [151]. The region excluded by NuCal is shown in Fig. 2.1 , 2.2 and 2.3.

NA64: In the NA64 experiment, an electron beam of 100 GeV was dumped on a lead target. We have considered the analysis of [152], in which an ALP decaying into a pair of photons was searched for. Since the two photons are too collimated to be distinguished, the final state was reconstructed as a single photon, allowing us to reinterpret this search. In this case the $N_1 N_2$ pair is produced via photon bremsstrahlung. Using 2.84×10^{11} electrons-on-target [152], we find that the number of events produced at NA64 is too small to put any bound on the parameter space of the model.

2.3.2 Colliders

We now analyze the bounds enforced by collider experiments, by considering searches performed at LEP, BaBar and LHC. In this case different searches apply, depending on whether the $N_2 \to N_1 \gamma$

[7] We have checked that the amplitude for the decay $P \to N_1 N_2$ mediated by Z boson exchange and with P a pseudoscalar meson vanishes identically. Moreover, we have estimated that the decay $P \to N_1 N_2 \gamma$ provides only a marginal improvement of our sensitivities. For this reason, we do not consider this contribution.

[8] We checked that production from heavier vector meson decays is negligible.

decay is prompt, *i.e.* it happens at a distance smaller than ~ 1 mm from the IP, displaced, *i.e.* it happens within ~ 1 mm and ~ 1 m, or else is detector-stable, *i.e* when the decay happens at a distances greater than ~ 1 m. For a $2 \to 2$ scattering, in terms of $\hat{s} = (p_{N_1} + p_{N_2})^2$, we have

$$\beta_{N_2}\gamma_{N_2} = \frac{\sqrt{\hat{s}}}{2m_{N_2}}\sqrt{1 + \frac{(m_{N_2}^2 - m_{N_1}^2)^2}{\hat{s}^2} - \frac{2\,(m_{N_1}^2 + m_{N_2}^2)}{\hat{s}}}, \tag{2.12}$$

while the N_2 lifetime is given by $\tau_{N_2} = \Gamma(N_2 \to N_1\gamma)^{-1}$, with the decay width of Eq. (2.5).

In the case of prompt decays, we consider two analyses: one from LEP [153] and one from BaBar [154]. In the LEP analysis, data were taken at various center of mass energies around the Z peak. We employ the largest dataset, taken at $\sqrt{\hat{s}} = 91.26$ GeV with an integrated luminosity of 52.462 pb^{-1}. We have simulated our signal at the parton level by using `MadGraph5_aMCNLO` [65]. We enforce the analysis selections by requiring a single photon with $|\cos\theta_\gamma| < 0.7$ and considering two signal regions. In the first one a minimum energy of the photon was required $E_\gamma > 22$ GeV, and no events were observed. In the second region the cut is loosened to $E_\gamma > 3$ GeV, with 73 observed events and 72 ± 5 expected SM events. Therefore, we set a 95% CL upper limit on the number of signal events $N_{\rm signal} = 3$ for the first signal region and $N_{\rm signal} \sim 22$ for the second one. For the weakly coupled normalization of the operator shown in Eq. (2.4), the stronger bound corresponds to $\Lambda \lesssim 17 - 50$ GeV for $\delta = 0.1 - 1$. However, these values of Λ lie outside the range of validity of the EFT, implemented as in Eq. (2.11), therefore we conclude that no meaningful constraints on the cutoff scale Λ can be set.

We then move to the analysis of BaBar in Ref. [154], which derived bounds on single photon events produced in association with an invisibly decaying dark photon. The selection of signal events makes use of a multivariate Boosted Decision Tree discriminant. Given the complexity of the analysis, we adopt a simplified strategy to estimate the constraint. We use `MadGraph5_aMCNLO` to simulate a sample of $e^+e^- \to N_1N_2$ events at the center of mass energies corresponding to the $\Upsilon(2s)$, $\Upsilon(3s)$ and $\Upsilon(4s)$ resonances, considering the luminosities reported in [154]. We enforce the selections $-0.4 < \cos\theta_\gamma < 0.6$ and $E_\gamma > 3$ GeV, corresponding to the LowM region of Tab. 1 of [154]. To extract a bound, we focus on the loose $\mathcal{R}'_L$ selection of [154], and assume an equal number of observed and background events. This allows us to set an upper limit at 95% CL of $N_{\rm signal} \sim 28$. The excluded region is largely independent of m_{N_1} but depends quite strongly on δ, since for $\delta \ll 1$ the energy of the photon in the laboratory frame is too small to pass the 3 GeV cut, see Eq. (2.8). We find that, for $\delta = (0.5 - 1)$, the bound extends up to $\Lambda \sim 60$ GeV, while for $\delta < 0.5$ the bound disappears. Given the approximate nature of our computation, we do not show these results explicitly in our figures.

Turning to searches for displaced events, we have considered analyses from ALEPH, ATLAS, CDFII and DELPHI [155–158]. Their reinterpretation is generally less straightforward than the ones for prompt signatures, due to the need of cutting on additional quantities as the photon time of flight and pointing variable. We decide to firstly apply a simplified strategy, by only imposing energy threshold and angular selection cuts on the final state photon. In this way the limit that we extract will be stronger than the one obtained by a full implementation of the analysis. Using this strategy we find that the strongest bounds come from the DELPHI search [158], see also [159]. In this case we enforce $E_\gamma > 10$ GeV and $|\eta_\gamma| < 4.04$, which corresponds to the angular coverage between 2° and 178° reported in the analysis. We have once again simulated $e^+e^- \to N_1N_2$ and the subsequent $N_2 \to N_1\gamma$ decay using `MadGraph5_aMCNLO`, with center of mass energies between 180 and 209 GeV, and with the corresponding luminosities as reported in [158]. Following this approach, we obtain 95% CL limits which are in the $20 - 40$ GeV ballpark, for $\delta = 0.1 - 1$. Given these results, we avoid implementing the full selection for the displaced analysis, since the obtained limits are already to be discarded because they lie beyond the validity of the EFT.

Finally, when N_1 and N_2 are both detector-stable, we consider searches of mono-γ with missing

energy, and the LEP limits on the invisible Z width. It turns out that the strongest bound comes from the latter. By requiring $\Gamma(Z \to N_1 N_2) < 0.56$ MeV [160] we obtain $\Lambda \gtrsim 9$ GeV, which again lies beyond the validity of the EFT[9].

We conclude this section by observing that some of the searches mentioned above could put meaningful constraints on the parameter space of strongly coupled UV completions of the EFT dipole operator. Implicit in our identification of the EFT cut-off scale with Λ in Eq. (2.4), is the hypothesis that the dipole operator is generated perturbatively at one loop level by some heavy states. An alternative possibility could be for the dipole operator to be generated by some strong dynamics, similarly to what happens for the neutron in QCD. In this case, adopting the convenient parametrization of the dipole operator $\mathcal{O}^5_{NB} = 1/\Lambda' \, \bar{N}^c \sigma^{\mu\nu} N B_{\mu\nu}$, one expects the EFT cut-off scale to be of the order of $\Lambda' = \Lambda \, (16\pi^2)/g_Y$. The bounds discussed above from the LEP search [153] valid for prompt decays are simply rescaled into $\Lambda' \gtrsim (8 - 23)$ TeV for $\delta = (0.1 - 1)$, essentially independent of m_{N_1}. Analogously, the simplified approach adopted for the DELPHI search [158] for displaced decays leads to the constraint $\Lambda' \gtrsim (9 - 18)$ TeV, again for $\delta = (0.1 - 1)$, essentially independent of m_{N_1}. Clearly in this case a more thorough reinterpretation of the analysis will be needed, with respect to the simplified approach previously described. Finally, the bound from the invisible Z decay width valid for the detector-stable case would read 4 TeV. Clearly, these constraints are probing a relevant part of the parameter space lying inside the regime of validity of the EFT, i.e. $\sqrt{\hat{s}} < \Lambda'$. It is important to notice that such bounds might be quite at odds with the range of N_1 and N_2 masses to which we are interested in. For example in a QCD-like strongly coupled scenario, we expect N_1 and N_2 to emerge as baryons, with masses of order Λ' and not much lighter as it would emerge from our analysis. A possibility of having a composite state much lighter than Λ' could be envisaged in a scenario where a light baryon arises in order to match the anomaly of an unbroken global chiral symmetry in the UV, along the lines of [161, 162]. We are not aware of any realistic model realizing such a framework. For this reason, in the remainder of the chapter, we will consider only the weakly coupled scenario of Eq. (2.4).

2.3.3 Bounds from astrophysics and cosmology

In addition to the bounds presented above, limits from astrophysics and cosmology may be important for the scenario that we are considering. The constraint which is more relevant for us comes from BBN. Although in our simplified scenario the dipole operator $\mathcal{O}^5_{NB}$ completely governs the N_2 decays, the fate of N_1 is determined by its mixing with the active sector. Particularly dangerous is the situation in which the N_1 decays could potentially spoil the predictions of the standard BBN model [163–165]. There are two natural ways to avoid this bound. Either N_1 is stable on cosmological scales, or N_1 decays with $\tau_{N_1} \lesssim 10^{-2}$ s. In the first case, N_1 would be a dark matter candidate[10]. In the second case, it has been shown in [163] that the combination of limits from BBN and terrestrial experiments exclude $m_{N_1} \lesssim (0.4 - 0.5)$ GeV, for N_1 mixing dominantly with ν_e or ν_μ, while lighter masses can be allowed for mixing dominantly with ν_τ. Since in the first case an important region of parameter space that can be tested by the experiments we consider would be excluded, we turn to the case of dominant mixing with ν_τ. Can such mixing be obtained in a way which is compatible with neutrino mass generation? As shown in [164], in a scenario with

[9] Notice that in any UV completion of the dipole operator new states with masses around the EFT cut-off scale will be present, among which there will also be states with non-vanishing electroweak charges. Therefore, if their masses are small enough, additional bounds, that we are not discussing, could arise from the on-shell production of these particles.

[10] The case in which a fermionic dark matter candidate χ interacts via a dipole operator $\bar{\chi}\sigma^{\mu\nu}\chi F_{\mu\nu}$ has been studied in Refs. [160, 166]. Our case would correspond to an *inelastic dark matter* scenario in which the dipole interactions are of the form $\bar{\chi}_2\sigma^{\mu\nu}\chi_1 F_{\mu\nu}$. In the $\delta \ll 1$ limit, we expect the phenomenology generated by $\mathcal{O}^5_{NB}$ to be qualitatively similar to the one studied in [160, 166]. On the other hand, in the opposite limit $\delta \gtrsim 1$, the phenomenology can be quite different and will be studied elsewhere.

only two RH neutrinos this is possible for $m_{N_1} \gtrsim 0.5$ (0.1) GeV for normal (inverted) hierarchy. The situation becomes less constrained considering three RH neutrinos, since in this case we have explicitly checked that a dominant $N_1 - \nu_\tau$ mixing can be obtained, in a way compatible with the generation of neutrino masses, for $m_{N_1} \gtrsim 0.1$ GeV, which is the range we consider. This can be obtained also by assuming a mass hierarchy $m_{N_1} \sim m_{N_2} \ll m_{N_3}$, *i.e.* in a situation in which the phenomenology is driven by N_1 and N_2 as the one we are considering by using the simplified scenario of Eq. (2.4). In what follows, we will always implicitly suppose this to be the case. For what concerns N_2, in Figs. 2.1, 2.2, 2.3 we show contours of constant N_2 lifetime, in order to highlight the region of the parameter space where N_2 decays fast enough to avoid BBN bounds.

Limits derived from supernovæ may also be important. Light particles produced in the interior of supernovæ, which reach temperatures of several tens of MeV, can escape from the star, therefore cooling the system. From this argument, masses up to a few hundred MeV can be constrained. In the $\delta \ll 1$ limit, we expect our scenario to be qualitatively similar to the one studied in [160], where the Authors focus on a dipole operator constructed with a single new Dirac fermion playing the role of the dark matter. They obtain bounds up to masses of ~ 0.1 GeV. In the mass range $1 - 100$ MeV, these limits exclude 2 TeV $\lesssim \Lambda \lesssim$ 50 TeV. The constraints disappear for larger Λ because the production inside the supernovæ is suppressed, while for smaller Λ efficient scattering processes can partially trap the particles inside the system. For the case $\delta \gtrsim 1$ we expect the situation to be qualitatively different from the one above. For small enough values of Λ, N_2 decays quickly, thus leaving a dominant population of N_1 inside the supernovæ. The only relevant N_1 scattering process is N_1 SM $\to N_2$ SM, which however might be not kinematically allowed for large δ, possibly making the bound disappearing at small values of Λ. This scenario has been studied in the context of inelastic dark matter with a dark photon mediator in [167], albeit by using a simplified and conservative approach. Given the complexity of performing a detailed analysis of the supernovæ bounds, and the fact that we expect these limits to affect only a quite limited region of parameter space, we defer a detailed study of this problem for future work.

2.4 Projected sensitivity of the SHiP and FASER 2 experiments

In this section we study the prospects for detection of long-lived RH neutrinos at the proposed future experiments SHiP [141] and FASER 2 [137, 138]. These experimental facilities have the capability to probe long-lived particles in a variety of hidden sector models [138, 168]. SHiP is a fixed-target experiment, based on a high intensity 400 GeV proton beam dumped on a heavy target. Instead, FASER 2 is an LHC experiment, which aims at exploiting the proton collisions occurring at $\sqrt{s} = 14\,\text{TeV}$ during the High-Luminosity LHC (HL-LHC) program. In this kind of experiments, RH neutrinos can be copiously produced by the decay of mesons generated by the proton collisions. The decay of long-lived N_2 particles can then show up in dedicated detectors located around the IP of these experiments. The expected number of signal events can be computed as:

$$N_{\text{signal}} = N_{\text{prod}} \left\langle \, f_{\text{dec}} \, \epsilon_{\text{det}} \, \right\rangle \ , \tag{2.13}$$

where N_{prod} is the total number of N_2 produced, f_{dec} corresponds to the probability for N_2 to decay inside the detector volume, and ϵ_{det} accounts both for the efficiency for the reconstruction of the events, that we simply take as 100%, and selection cuts. Finally, $\langle \cdot \rangle$ indicates a statistical average, that we define in the following. We consider the production of RH neutrinos from the decay of the following mesons: $M = \rho, \omega, J/\Psi, \Upsilon$. The number of N_2 produced then reads:

$$N_{\text{prod}} = \sum_M N_{\text{POT}} \, N_M \, \text{BR}(M \to N_1 N_2), \tag{2.14}$$

where $N_{\rm POT}$ is the total number of collected protons on target, N_M is the average number of mesons M produced per proton interaction, and $\mathrm{BR}(M \to N_1 N_2)$ is the branching ratio of the decay of the meson M into RH neutrinos, computed in App. 2.2. Similarly, the number of RH neutrinos produced by the decay of mesons at the LHC is given by:

$$N_{\rm prod}^{\rm LHC} = \sum_M \sigma_{\rm ine}\, \mathcal{L}\, N_M\, \mathrm{BR}(M \to N_1 N_2), \tag{2.15}$$

where $\mathcal{L} = 3\,\mathrm{ab}^{-1}$ is the integrated luminosity at the HL-LHC, and $\sigma_{\rm ine} = 79.5\,\mathrm{mb}$ is the inelastic proton-proton cross-section [169]. The quantity $f_{\rm dec}$ is:

$$f_{\rm dec} = e^{-L_{\rm entry}/L_{N_2}} - e^{-L_{\rm exit}/L_{N_2}}, \tag{2.16}$$

where $L_{\rm entry}$ ($L_{\rm exit}$) is the distance between the IP where the N_2 particle is produced, and the point at which N_2 enters (exits) the detector. Finally, L_{N_2} is the decay length of N_2 in the laboratory frame, given by $L_{N_2} = \beta_{N_2}\gamma_{N_2} c\tau_{N_2}$. Our calculations are based on simulations of the production of mesons performed with `PYTHIA 8.3` and `EPOS-LHC` [170]. More details will be given in the following. From these simulations we obtain a sample of mesons events, and we compute the associated multiplicities N_M. Then, for each meson event in the sample, we simulate its decay in $N_1 N_2$ pairs. These data are used to statistically evaluate Eq. (2.13), averaging ($\langle\cdot\rangle$) Eq. (2.16) over all the possible kinematical configurations of the N_2 particles in our sample. Finally, we impose a minimum energy of the photon produced in the decay $N_2 \to N_1 + \gamma$. We compute the efficiency of this selection cut, $\epsilon_{\rm det}$, using the N_2 events in our sample, simulating the N_2 decays, and selecting the events for which the photon energy in the laboratory frame is larger than a threshold $E_{\rm cut}$. The procedure explained in this section has been used to compute the number of signal events also at the CHARM and NuCal experiments described in Sec. 2.3.

2.4.1 SHiP

The SHiP fixed-target experiment aims at accumulating $N_{\rm POT} = 2 \times 10^{20}$ protons on a target composed by Molybdenum and Tungsten in 5 years of operation. A description of the experiment can be found in [142]. The decay volume of the detector has a length of 50 m and it is located at ∼45 m from the proton target. A spectrometer and a particle identification system with a rectangular acceptance of $5 \times 10\,\mathrm{m}^2$ are placed behind the decay volume. The rectangular face of the decay volume closer to the IP has a size of $1.5 \times 4.3\,\mathrm{m}^2$. Following these specifics, we approximate the detector as a cylinder with an opening angle of 31.8 mrad.

The production of the different mesons at SHiP is based on simulations of proton-proton collisions performed with `PYTHIA 8.3`. For the ρ and ω mesons we obtain the production multiplicities $N_\rho = 0.58$ and $N_\omega = 0.57$, in good agreement with previous results present in the literature [146, 166, 171–173]. We assume the same production rate for proton interactions in the target material of SHiP. In principle a dependence on nuclear target is expected, however detailed simulations or measurements are needed to fully capture these effects. Instead for the J/Ψ, we normalize our simulation in order to reproduce the total number of mesons predicted by the SHiP collaboration in [174]: $N_{J/\Psi} = 2 \times X_{\bar{c}c} \times f(q \to J/\Psi) \times f_{\rm cascade}$. The $\bar{c}c$ production fraction is $X_{\bar{c}c} = 1.7 \times 10^{-3}$, the J/Ψ production fraction is $f(q \to J/\Psi) = 0.01$ and the enhancement from cascade events is $f_{\rm cascade} = 2.3$. Finally, the production rate of the Υ mesons is directly obtained using `PYTHIA 8.3`, as for the case of the ρ and ω, since detailed simulations of the production at SHiP are not available. We find[11] $N_\Upsilon = 2.2 \times 10^{-9}$.

[11] We use the same multiplicities of ρ, ω and Υ for CHARM and SHiP since the energy of the proton beam is the same and we have neglected medium dependent effects.

Currently, there are no studies of the background rates at SHiP for the single photon signature arising in our scenario. By assuming that the backgrounds can be reduced at a negligible level as it happens for other searches, see *e.g.* [174], the 95% CL upper limit on the number of signal events is $N_{\rm signal} = 3$. For a more conservative approach we follow [175], which estimated ~ 1000 background events after rescaling the background events observed at the NOMAD detector by the number of POT in the two experiments. This number will likely be reduced by vetos, as noticed in [175]. Assuming Poisson likelihood, we set a 95% CL upper limit on the number of signal events of $N_{\rm signal} \sim 63.8$. Finally, we impose a minimum energy of the photon $E_{\rm cut} = 1\,\text{GeV}$, which is a reasonable threshold for SHiP [176]. Summarizing, in Fig. 2.1 we show sensitivity contours for the two choices of signal events discussed here. This corresponds to a range between an optimistic and a conservative assumption of the background level.

2.4.2 FASER 2

The FASER collaboration has proposed to build a suite of forward detectors to be placed within the LHC environment along the beam axis, nearby the ATLAS experiment [138]. These experiments are dedicated to study several interesting topics, as the properties of neutrinos, QCD in the forward regime and new physics beyond the SM, including dark sectors. Several small size pilot detectors have already been constructed, which are FASER [137,177], FASERν [178,179] and SND@LHC [180]. However, to fully exploit the potential of the HL-LHC, a dedicated facility to host larger detectors is under study. In particular, we focus on the proposed FASER 2 detector, which is dedicated to the study of long-lived particles. According to current design, it will be placed at 620 m from the IP, and it will have a cylindrical shape, with a radius of 1 m and a length of 10 m [138].

To simulate the production of the ρ and ω mesons at the LHC, we use `EPOS-LHC`, which has been tuned to forward LHC data. For the J/Ψ and Υ mesons we again use `PYTHIA 8.3`, rescaling its rates to match the production cross-sections as measured by the LHCb experiment [181,182]. In addition, following [183], we modify the production rate as a function of the transverse momenta p_T with respect to the default setup of `PYTHIA 8.3`. Employing this procedure, we obtain a good agreement with the measured p_T distributions [181,182]. The resulting production multiplicities in one hemisphere are $N_\rho = 2.3$, $N_\omega = 2.2$, $N_{J/\Psi} = 5.0 \times 10^{-4}$ and $N_\Upsilon = 6.1 \times 10^{-6}$. In addition to the production of RH neutrinos from the decay of mesons, we include Drell-Yan processes $q\bar{q} \to \gamma/Z \to N_1 N_2$. More details are provided in App. 2.4.3. This production mechanism is however in most cases subdominant with respect the one from mesons decay.

FASER 2 will be sensitive to photon signals and, at the same time, it will have the capability to strongly reduce the relevant backgrounds, see the discussion in [184] where single photon signals have been studied in the context of a model of sterile neutrinos coupled to active neutrinos via a dipole operator[12]. Since a thorough simulation of the relevant backgrounds has not been performed yet, we decide to follow the strategy of [184], presenting our results as isocontours of $N_{\rm signal} = 3$ and $N_{\rm signal} = 30$ events. A cut on the energy of the photon $E_{\rm cut} > 100\,\text{GeV}$ has been employed in our analysis, again inspired by [184].

2.4.3 Results

Our main findings are presented in Fig. 2.1, where we fix the phase to $\alpha = \pi/2$ to maximize the production rate from meson decays, see Sec. 2.2. The results remain qualitatively the same for other choices. We show two different slices of the parameter space: either we fix the mass splitting δ and we explore the plane $m_{N_1} - \Lambda$ or we fix the mass of N_1 and we project the results on the $\delta - \Lambda$ plane. In both cases we consider three benchmark scenarios, namely $\delta = 0.01, 0.1, 1$ in the first case

[12] See also [185] for an analogous signature in the context of R-parity violating SUSY.

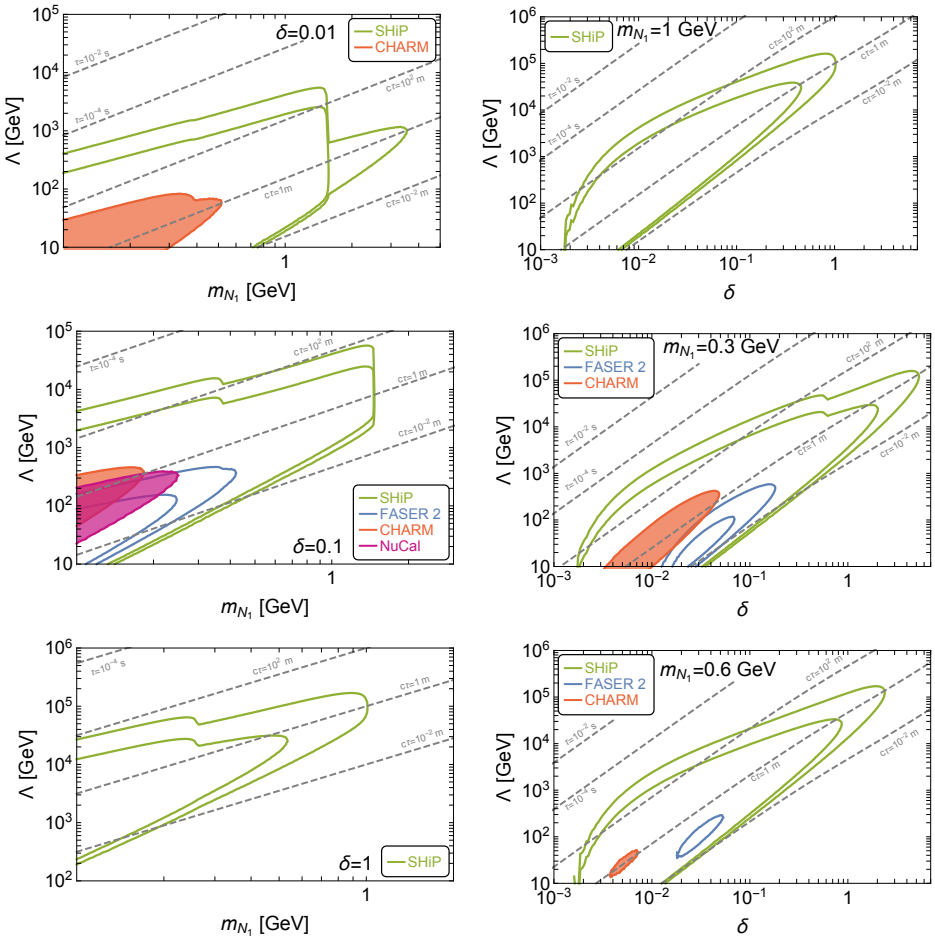

Figure 2.1: Green and blue lines are the sensitivity reach of the SHiP and FASER 2 experiments. For SHiP we show isocontours of $N_{\rm signal} = 3$ and $N_{\rm signal} = 63.8$. For FASER 2 we show isocontours of $N_{\rm signal} = 3$ and $N_{\rm signal} = 63.8$, see Sec. 2.4 for more details. The orange and magenta shaded regions are excluded by the CHARM and NuCal experiments. The dashed lines are contours of constant N_2 lifetime or proper decay length. We fix $\alpha = \pi/2$.

and $m_{N_1} = 0.3, 0.6, 1$ GeV in the second case. As explained in Sec. 2.4, the sensitivities of SHiP and FASER 2 are computed for two numbers of signal events, corresponding to different choices of the background rate at these experiments. The strategy followed to compute the regions excluded by CHARM and NuCal is detailed in Sec. 2.3. When the line associated to a specific experiment is missing in our plots, this means that the corresponding experiment has not enough sensitivity to probe the parameter space.

As evident in Fig. 2.1, for a mass splitting $\delta = 0.1$, both SHiP and FASER 2 will be able to extend the current limits from CHARM and NuCal, and probe an uncharted region of the parameter space. In particular the sensitivity of SHiP reaches N_1 masses around the kinematical threshold for production from the decay of the J/Ψ meson, *i.e.* $m_{N_1} \sim 1.5$ GeV. A more modest sensitivity is obtained for FASER 2. It is worth recalling that despite small values of Λ are formally not excluded in the EFT of Eq. (2.4), weakly coupled UV completions with $\Lambda \lesssim 100$ GeV are likely already ruled

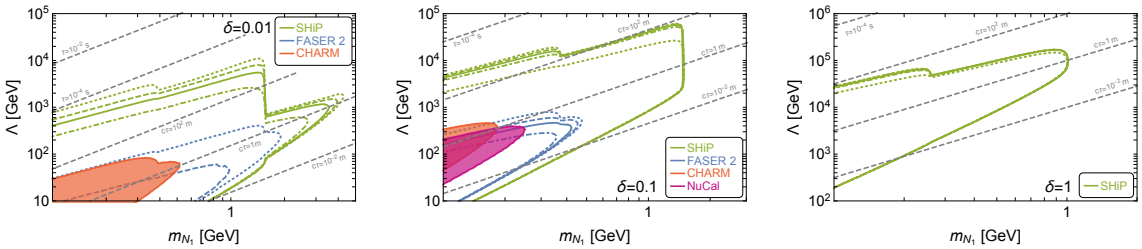

Figure 2.2: Isocontours of $N_{\rm signal} = 3$ for SHiP (green lines) and FASER 2 (blue lines). For SHiP dotted, dashed, solid, dot-dashed and dotted lines are for $E_{\rm cut} = 0.1, 0.5, 1, 2, 10$ GeV respectively while for FASER 2 dotted, dashed, solid and dot-dashed lines are for $E_{\rm cut} = 10, 50, 100, 200$ GeV respectively. The CHARM and NuCal regions and the gray lines are as in Fig. 2.1. We fix $\alpha = \pi/2$.

out from direct searches of additional EW charged states. The constraints from BBN on N_2 decays are of the order $\tau_{N_2} = \mathcal{O}(10^{-2} - 1)$ s, see Sec. 2.3.3. Looking at the isocontour of τ_{N_2} in Fig. 2.1, one can notice that these bounds are not overlapping with the sensitivities of SHiP and FASER 2. For a larger mass splitting, $\delta = 1$, the region probed by SHiP tends to shift to larger values of Λ, while FASER 2 can not probe this slice of the parameter space. This behaviour can be understood by recalling that increasing δ tends to reduce the lifetime of N_2, see Eq. (2.5). This can be compensated by increasing Λ at the price, however, of reducing the production rate of $N_1 N_2$ pairs. The correlation between δ and Λ can be appreciated in the plots with m_{N_1} fixed. The different experiments that we have studied are probing proper decay length $c\,\tau_{N_2} \sim 10^{-2} - 10^3$ m.

In the case of a smaller mass splitting, as in the case of $\delta = 0.01$, the threshold on the energy of the photon plays an important role. Small δ reduces the energy of the photon, see Eq. (2.8). This implies that at FASER 2 most of the events do not satisfy the cut $E_{\rm cut} > 100\,\text{GeV}$ and therefore no sensitivity is obtained. To highlight the role of the energy threshold, in Fig. 2.2 we show the isocontours of $N_{\rm signal} = 3$ for different values of $E_{\rm cut}$, namely $E_{\rm cut} = 0.1, 0.5, 1, 2, 10$ GeV for SHiP and $E_{\rm cut} = 10, 50, 100, 200$ GeV for FASER 2. While for $\delta = 1$ the sensitivities are almost unchanged, for smaller δ the energy threshold has a significant impact. In particular, for $E_{\rm cut} \sim 10$ GeV and provided that background can be kept negligible, FASER 2 will be able to test up to $\Lambda \sim 400$ GeV for $\delta = 0.01$, to be compared with a zero sensitivity scenario with $E_{\rm cut} \sim 100$ GeV, shown in Fig. 2.1.

Finally, before concluding, we shall mention that the RH dipole operator might also be tested by the currently operating e^+e^- collider experiment Belle II [186], and by the future neutrino experiment DUNE [187]. Dedicated analyses are in order to investigate their sensitivities.

Projected sensitivity of other future LHC experiments

In addition to FASER, several other LHC detectors dedicated to search for long-lived particles have been proposed in recent years: MATHUSLA [188, 189], CODEX-b [133–135], AL3X [190], MAPP [139, 140], ANUBIS [132] and FACET [136]. These facilities, to be placed around the LHC IP points, could potentially probe the radiative decay of the RH neutrinos that we are considering. Concretely, we focus on CODEX-b, ANUBIS, MAPP and FACET, that, in principle, can have the potential to reconstruct photons (for CODEX-b this assumes an extension of the baseline design, according to [134])[13]. For the single photon signature under scrutiny, the background rates at these experiments have not been computed, and a detailed discussion of their capability to reduce the

[13]We thank members of the MATHUSLA, ANUBIS, MAPP and FACET collaborations for discussions on this point.

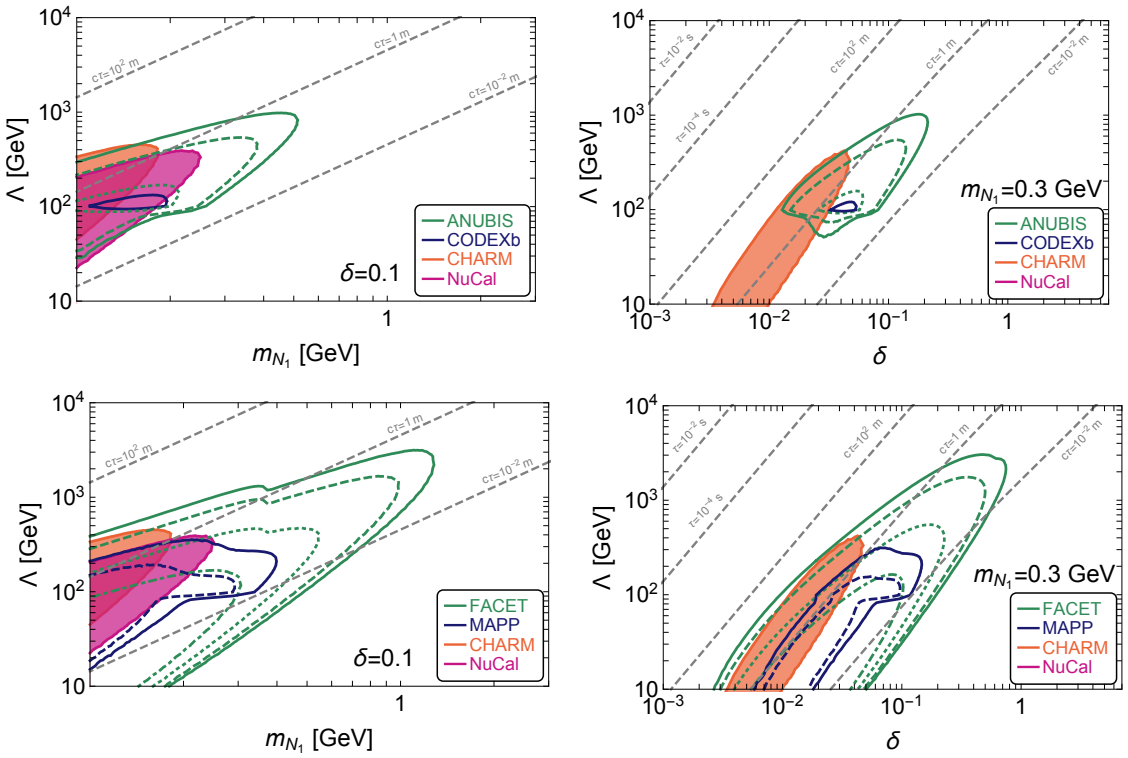

Figure 2.3: Sensitivity reach of the experiments ANUBIS, CODEX-b, CHARM and NuCal. Solid, dashed, dotted and dot-dashed lines correspond to $N_{\rm signal} = 3$, $N_{\rm signal} = 10$, $N_{\rm signal} = 100$ and $N_{\rm signal} = 1000$. The colored regions and the dashed lines are as in Fig. 2.1. We fix $\alpha = \pi/2$.

relevant backgrounds is not currently available in the literature. Given this limited information, the estimate of their sensitivity reach is quite uncertain. We show the region of the parameter space where the following numbers of signal events at these experiments are obtained: $N_{\rm signal} = 3, 10, 100, 1000$. These results are intended to give an idea of potential sensitivity reach of these proposals, if the backgrounds are reduced to the appropriate rates.

For the calculation of the signal rate we follow the same procedure described in Sec. 2.4. The geometry of the different experiments and the cut on the photon energy $E_{\rm cut}$ are the same adopted in [191]. We consider two mechanisms for the production of the RH neutrinos: meson decays, see Sec. 2.4.2 for details, and Drell-Yan processes. For the latter, we employ `MadGraph5_aMCNLO` for our simulations. A couple of comments are in order. As discussed in Sec. 2.3, we should require that the energy scale of this process is smaller than the cut-off of the EFT. Assuming a weakly coupled extension of the SM and couplings of $\mathcal{O}(1)$, we impose $\sqrt{\hat{s}} < \Lambda$, where $\hat{s}$ is the Mandelstam variable associated to the process $q\bar{q} \to \gamma/Z \to N_1 N_2$. In practice, from our `MadGraph5_aMCNLO` simulations, we select only the events satisfying this condition. In addition, we impose $\sqrt{\hat{s}} > 2\,\text{GeV}$, in order to work in the regime of perturbative QCD.

The results are shown in Fig. 2.3 for two different slices of the parameter space: fixing the mass splitting to $\delta = 0.1$ or fixing the mass of the lightest RH neutrino to $m_{N_1} = 0.3$ GeV. For some experiments, FACET and ANUBIS, $N_{\rm signal} > 10^2 - 10^3$ can be obtained in some parts of the parameter space, while more modest signal rates are obtained in other cases, as for CODEX-b and MAPP.

Experiments	POT(10^{20})	$\epsilon_{\rm eff}$	Cuts	References
SHiP	2	~ 1	$E_R \in [1,\, 20]$ GeV, $\theta_R \in [10,\, 20]$ mrad	[141, 192]
CHARM II	0.25	~ 1	$E_R \in [3,\, 24]$ GeV, $E_R\theta_R^2 \leq 3$ MeV	[193, 194]
DUNE (10 yr)	11/yr	0.5	$E_R \in [0.6,\, 15]$ GeV, $E_R\theta_R^2 \leq 1$ MeV	[195, 196]

Table 2.1: Summary of the main characteristics of the experiments that we considered. Here E_R and θ_R are the recoil energy and the recoil angle with respect to the incoming neutrino's momentum of the scattered electrons, while $\epsilon_{\rm eff}$ is the detection efficiency of the signal.

In general, we find that for the forward detector FACET and FASER 2, the production from meson decays is more relevant than the one from Drell-Yan processes. The opposite situation happens for the off-axis detectors ANUBIS and CODEX-b. In some cases the sensitivity disappears at small Λ, see the bottom left panel of Fig. 2.3 or the flattening of the curves in the other panels. This is due to the requirement $\sqrt{\hat{s}} < \Lambda$ that we impose in our simulation: for small enough Λ most of the events in the simulation are rejected.

Electron recoil searches

The dipole operator of Eq. (2.4) induces an inelastic scattering processes between RH neutrinos and electrons, namely

$$N_2\, e^- \to N_1\, e^- \tag{2.17}$$

and

$$N_1 e^- \to N_2 e^- \ . \tag{2.18}$$

Note that the latter process is kinematically open only if the center of mass energy is sufficiently large, given that $m_{N_2} \geq m_{N_1}$. Such processes can give rise to a signal in experiments sensitive to e-recoils. We have considered experimental searches at SHiP, CHARM II and DUNE and estimated present and future constraints. These are fixed-target experiments, whose number of POT, detection efficiencies and cuts enforced in the analysis are recollected in Tab. 2.1. The expected number of signal events is the sum of three contributions

$$N_{\rm sig} = N_{12} + N_{21} + N_{212}, \tag{2.19}$$

which are

- N_{12}: an N_1 particle produced by mesons decays produces an e-recoil signal in the detector through $N_1 e^- \to N_2 e^-$ scattering;
- N_{21}: an N_2 particle produced by mesons decays produces an e-recoil signal in the detector through $N_2 e^- \to N_1 e^-$ scattering;
- N_{212}: an N_1 particle produced by N_2 decay produces an e-recoil signal in the detector through $N_1 e^- \to N_2 e^-$ scattering.

Each term has been evaluated through a Montecarlo simulation of the process. The $N_{1,2}$ neutrinos have been assumed to be produced from meson decays, and the fluxes of mesons have been simulated with `PYTHIA 8.3`, as explained in the main text. The electron number density of the detectors has been obtained from the weight and the material of each experimental apparatus.

We have computed the differential cross section with respect to the recoil energy of the inelastic scattering processes, assuming initial electrons at rest. Explicitly

$$\frac{d\sigma}{dE_R}(N_2 e^- \to N_1 e^-) = \frac{m_e}{2\pi}\left(\frac{e^2}{16\pi^2\, m_e\, P_{N_2}\Lambda}\right)^2 f(m_e^2 + m_{N_2}^2 + 2m_e E_{N_2}, -2m_e E_R), \tag{2.20}$$

$$\frac{d\sigma}{dE_R}(N_1 e^- \to N_2 e^-) = \frac{m_e}{2\pi}\left(\frac{e^2}{16\pi^2\, m_e\, P_{N_1}\Lambda}\right)^2 f(m_e^2 + m_{N_1}^2 + 2m_e E_{N_1}, -2m_e E_R), \tag{2.21}$$

where $P_{N_{1,2}}$ are the moduli of the RH neutrino spacial momenta, $E_{N_{1,2}}$ their energy, the recoil energy E_R is the kinetic energy of the final electron and

$$\begin{aligned} f(s,t) = \frac{1}{t^2}\big\{&4(m_{N_1} m_{N_2} m_e)^2 - 2m_e^4 t + (t^2 + 2st)(m_{N_1}^2 + m_{N_2}^2 + 2m_e^2) \\ &- (t + 2m_e^2)(m_{N_1}^4 + m_{N_2}^4) - 2st(s+t) - 2m_{N_1} m_{N_2} t(t + 2m_e^2)\cos(2\alpha)\big\} \end{aligned} \tag{2.22}$$

with $\lambda(x,y,z) = x^2 + y^2 + z^2 - 2xy - 2yz - 2zx$.

We find the number of recoil events to be negligible for values of Λ above 1 GeV, independently of the values of m_{N_1} and δ. We then conclude that searches through electron recoils do not impose relevant constraint on the νSMEFT parameter space. In the limiting case $\delta = 0$, we reproduce existing results available in the literature, which have focused on the case of elastic scattering processes [166].

2.5 Summary

In this chapter we have studied the phenomenological consequences of a dipole operator between RH neutrino fields. This is described by the νSMEFT $d = 5$ operator $\bar{N}_2 \sigma^{\mu\nu} N_1 B_{\mu\nu}$ and triggers the decay $N_2 \to N_1 \gamma$, which is the subject of our study. Motivated by the current experimental and theoretical interest, we have focused on RH neutrino masses in the GeV range and considered the regime in which N_2 is long-lived, with a proper decay length of $\mathcal{O}(10^{-2} - 10^3\,\mathrm{m})$, while N_1 is considered to be stable on these length scales.

More in details, we have firstly considered the existing bounds on this scenario, arising from terrestrial experiments like CHARM, NuCal and colliders, as well as constraints from cosmological considerations, in particular in relation to the Big Bang Nucleosynthesis epoch.

We have subsequently investigated the sensitivity of the future proposed experiments FASER 2 and SHiP. In these facilities the RH neutrinos are produced in $N_1 N_2$ pairs through the dipole operator, either via meson decay or via direct production. Then, RH neutrinos give rise to single$-\gamma$ events through $N_2 \to N_1 \gamma$ decays, which can be detected by these experiments in a background controlled environment.

Our main results are summarized in Fig. 2.1 where we show that SHiP will be able to probe ample regions of the parameter space not yet excluded by current data, testing Wilson coefficients up to $\Lambda \sim 10^5$ GeV, while the sensitivity of FASER 2 is more limited. Given the early design stage at which these experiments are, and the preliminary nature of the background estimates for the scenario under consideration, we have then studied how different cuts on the photon energy enforced at the analysis level affect the sensitivity reach. Our results are shown in Fig. 2.2. We found that relaxing the cut on the photon energy has a limited impact on the sensitivities predicted for SHiP, while for FASER 2 ampler regions of parameter space can be reached, provided that the background can be maintained at a negligible level.

To summarize, our work provides a first realistic estimate on the reach of experiments targeting long-lived particles on the lowest dimensional effective dipole operator that appears in the minimal see-saw extension of the Standard Model.

Part II: $SM + X17$ at ATOMKI

Chapter 3

An updated view on the ATOMKI nuclear anomalies

3.1 Introduction

The possibility that New Physics will manifest itself in the form of light and weakly coupled new states is nowadays raising more and more interest. This is mainly due to the null results from the LHC in searching for signs of TeV scale BSM physics motivated by, *e.g.*, the standard paradigms of compositeness or supersymmetry. While high$-p_T$ searches will continue to investigate these scenarios and, in the case of no discovery, further constrain them, it is of paramount importance to exploit any other experiment that can test the validity of the SM and ultimately falsify it. In this respect low energy and/or high intensity experiments provide an important probe.

Among the various processes that can be investigated, rare nuclear transition can provide a good handle to observe NP appearing at the MeV scale, since they can significantly be affected by BSM physics even if this is very weakly coupled. A nuclear transition occurs when an excited nucleus decays into a lower energy level of the same nucleus. Within the SM only electromagnetic (EM) interactions can mediated nuclear transition, which can mainly proceed through the following channels

- $\gamma-$emission, where the nucleus decays emitting a real photon,
- Internal Pair Creation (IPC), where the nucleus emits a virtual photon which then decays to an e^+e^- pair.

In recent years the ATOMKI collaborations has reported various anomalous measurements in the IPC decays of excited ^{8}Be [22,197], ^{4}He [23,198] and, more recently, ^{12}C [24] nuclei. These anomalies appear as bumps for both the invariant mass and the angular opening of the e^+e^- pairs and have a high statistical significance, well above 5σ. The ATOMKI collaboration has proposed to interpret them as due to the on-shell emission of a new boson X from the excited nuclei, subsequently decaying to an e^+e^- pair. The best fit mass for the hypothetical new particles is estimated to be ~ 17 MeV. Although to this day no independent confirmation of these results has arrived, given the multitude of processes in which these anomalies have been observed the ATOMKI results have attracted a considerable attention from the particle physics community. Many theoretical interpretation of the X boson in terms of a new scalar or vector degree of freedom have been put forward, possibly unaccounted SM effects have been investigated and experimental searches have been proposed and/or are taking data with the goal of further investigating this anomaly.

In view of the latest experimental results recently released by the ATOMKI collaboration, we critically re-examine the possible theoretical interpretation of the anomaly in terms of a new BSM state. To this end we employ a multipole expansion method and give an estimate for the range of values of the nucleon couplings to the new light state in order to match the experimental observations. We will focus on the ^{8}Be and ^{4}He anomalies and comment on how the measurement of the anomalous signal in ^{12}C transitions impact our results. Our conclusions identify the axial vector state as the most promising candidate, while other spin/parity assignments seems disfavored for a combined explanation. However the axial nuclear matrix element of the ^{12}C transition is currently unknown and, as we will show, our findings regarding the compatibility of an axial vector candidate with the ^{12}C anomalous transition are based upon an order of magnitude estimate. Before being able to draw a definite and solid conclusion, the relevant matrix element must be evaluated. Intriguingly, an axial vector state can also simultaneously accommodate other experimental anomalies, *i.e.* the KTeV anomaly in $\pi^0 \to e^+e^-$ decay while being compatible with the conflicting measurements of the anomalous magnetic moment of the electron $(g-2)_e$ and other constraints on the electron couplings of the X boson. The PADME experiment will completely cover the relevant region of the parameter space, thus allowing for a strong test of the existence of the X particle.

The chapter is structured as the following. In Sec. 3.2 we review the anomalous measurement of the ATOMKI experiment and the theoretical interpretation proposed so far. In Sec. 3.3 we describe the multipole expansion formalism and in Sec. 3.4 we apply the multipole formalism to the electromagnetic case of real γ emission and IPC while in Sec. 3.5 we present the results of the decay rates of the ^{8}Be, ^{4}He and ^{12}C resonances for the various spin-parity assignment of the X boson. In Sec. 3.6 we collect the experimental bounds for the spin-1 case relevant for our study. We present our results in Sec. 3.7 and we then conclude in Sec. 2.5. We also add some appendices with more technical details. In App. B we derive the effective nuclear couplings from the X boson couplings to quarks. In App. C we present how our results change by considering also the ^{8}Be(17.64) excited state. Finally in App. D we report useful formulæ for the cross section of nuclear resonance production.

3.2 The ATOMKI anomaly

The ATOMKI experiment [199] consists in a proton beam colliding a target nucleus A at rest, with the aim of producing an excited nucleus N^* and measure its IPC transition to a ground state N, *i.e.*

$$p + A \to N^* \to N + e^+e^- \ . \tag{3.1}$$

The list of nuclei used by ATOMKI and their main properties are reported in Tab. 3.2 and Tab. 3.3. In 2015 the ATOMKI group studied the IPC decay channel from the ^{8}Be(18.15) and ^{8}Be(17.64) excited energy levels of Beryllium nuclei [22]. To populate the two states, a beam of protons was prepared in order to collider with target ^{7}Li nuclei at rest. By varying the energy of the incident proton beam, the collaboration was able to scan across the ^{8}Be resonances. As a results they observed an anomalous peak corresponding to an opening angle for the e^+e^- pairs of $\sim 140^\circ$ for the IPC correlation distribution, in striking contrast with the QED prediction of a rapidly falling one. This has been interpreted as due to the decay of a short-lived neutral particles decaying into an e^+e^- pair, which would produce the observed peak at large angles. The observed deviation had a significance of 6.8σ. In order to confirm the anomalous origin of the signal, the collaboration repeated the measurement varying the energy of the incident proton beam. They found that the anomaly disappeared off the resonance peak, leading to the conclusion that it was probably originated by the decay of the ^{8}Be excited energy level. The best fit mass for the hypothetical X neutral boson has been estimated to be $m_X = 16.70 \pm 0.35 \pm 0.5$ MeV, where the former uncertainty corresponds to the statistical error, while the latter to the systematic one. In 2018 the ATOMKI collaboration

N	N^*	S^π	I	Γ(keV)	Γ_γ(eV)
^{8}Be		0^+	0	5.57 ± 0.25	
	^{8}Be(18.15)	1^+	0^*	138 ± 6	1.9 ± 0.4
	^{8}Be(17.64)	1^+	1^*	10.7 ± 0.5	15.0 ± 1.8
^{4}He		0^+	0	Stable	
	^{4}He(21.01)	0^-	0	0.84	0
	^{4}He(20.21)	0^+	0	0.50	0
^{12}C		0^+	0	Stable	
	^{12}C(17.23)	1^-	1	1150	44

Table 3.1: Spin-parity J^π and isospin I quantum numbers, total decay widths Γ and γ-decay widths $\Gamma_\gamma = \Gamma(N^* \to N\,\gamma)$ for the nuclei used in the ATOMKI experiment: ^{8}Be [200], ^{4}He [201, 202] and ^{12}C [203, 204] nuclei. Asterisks on isospin assignments indicate states with significant isospin mixing.

repeated the experiment with an improved setup [197], which confirmed both the presence of the anomaly and the compatibility with the previous measurement.

Later in 2019 the ATOMKI group replicated the experiment using ^{4}He nuclei [23], with the aim of searching for the anomalous signal in a difference source. The excitation energy was chosen to lie between two different resonances: the ^{4}He(20.21) state, with $J^\pi = 0^+$, and the ^{4}He(21.01) state, with $J^\pi = 0^-$. In this case the decay widths of the two excited states are large enough so that they can substantially overlap, so in the experiment both the excited states were populated, although off the resonance peak. In this case the IPC process was only possible for the ^{4}He(20.21) states, while it's forbidden for the ^{4}He(21.01), because of parity conservation in electromagnetic interactions. The group again found a rather sharp bump in the e^+e^- angular opening analogously to what has been observed in the ^{8}Be case, with a significance equal to 7.2σ. Interestingly, the peak was found to be located at an angle of $\sim 115°$ which is compatible with the kinematics arising from the decay of the hypothetical X boson with a best fit mass of $m_X = 16.98 \pm 0.16 \pm 0.2$ MeV. Also the anomaly in the ^{4}He channel was later confirmed by a second measurement, at different energies of the proton beam [198]. More recently, the group has released a new analysis, where the experiment has been replicated using now ^{12}C nuclei [24]. Also in this case an anomalous signal has been observed, with a peak at a larger value of the e^+e^- opening angle $\sim 150° - 160°$, again compatible with the kinematic of the X particle, with a best fit mass of $m_X = 17.03 \pm 0.11 \pm 0.20$ MeV. In Tab. 3.1 we list all the ground and excited states considered in the ATOMKI analyses, together with their main properties: spin-parity assignment S^π, isospin I, total decay width Γ and γ-decay transition width Γ_γ.

Clearly, new and independent measurements are needed in order to confirm, or disproof, the results of the ATOMKI collaboration and test the consistency of the X particle hypothesis. The MEG II experiment [205] at PSI has the possibility to repeat the ATOMKI measurement on ^{8}Be nucleus. At present time, the first dedicated data taking has recently been completed and data analysis is ongoing [206]. A similar experiment is also being set up at the Montreal Tandem accelerator [207] with data taking that should take place in early 2023, and at the Van-de-Graaff laboratory [208]. Finally, also the PADME experiment [209, 210] in Frascati is in its data taking phase, and dedicated analyses will completely test the available parameter space for the coupling of the X boson to electrons relevant for the explanation of the ATOMKI anomalies [211, 212].

These results and the interpretation given by the ATOMKI collaboration in terms of a new BSM particle comprehensibly attracted the attention of the theory community. However there also exist the possibility that the anomalous signal is due to unknown and/or underestimated SM effects. In this respect, after the publication of the ^{8}Be measurements, an attempt has been made in order to explain the anomaly with effects arising from known nuclear physics. In [213] it has been proposed an improved nuclear physics model of the experiment, inspired by the so-called Halo Effective Field Theory (EFT) framework [214], showing that the nuclear form factor needed to explain the anomaly suggests an unrealistic large length scale on the order of 10 fm for the ^{8}Be nucleus. Other Authors investigated the possibility of new exotic bound states [215–217] as possible SM explanation of the ATOMKI anomaly while, on less exotic lines, it has been claimed in [218] that the experimental results can be reproduced within the SM by carefully considering the full set of next-to-leading-order corrections and the interference terms to the Born-level decay amplitudes, also proposing experimental improvements in order to test this hypothesis. All together it is fair to say that no firm explanation of the ATOMKI measurements in terms of SM effects has been established.

As regarding possible BSM interpretation, the observation of the ^{8}Be and ^{4}He transitions restrict the X boson to be either a vector, an axial vector or a pseudoscalar state, under the assumption of definite parity. These options have been all investigated in recent literature both from a model independent and/or effective parametrization and from a more ultraviolet (UV) completed perspective. Among all the possibilities the one of a spin-1 boson stands out as an appealing one, since it could be related to a new symmetry of Nature. This scenario has been deeply analyzed in [219–221], where, by working within an EFT framework, it has been found that a combined explanation of the ^{8}Be and ^{4}He anomalies in terms of a new vector states is possible, with the main constraint on this explanation coming from the search for a dark photon γ_D in $\pi^0 \to \gamma\,\gamma_D$ decay by the NA48/2 collaboration [222], whose non observation requires the X boson to be *protophobic*. Subsequently in [223] it has been pointed out that the contribution from a *protophobic* vector boson with mass around 17 MeV to direct proton capture processes, *i.e.* to processes which do not proceed through an intermediate resonance, would be dominant with respect to the contribution from the resonant ^{8}Be(18.15) state, in sharp contradiction with the experimental observation that the anomaly disappears off the nuclear resonance [22]. However a new experimental result from ATOMKI [224] claims to have observed the anomaly at different energies of the proton beams, opposite to their previous results. The group explains that this difference is due to a wrong estimate of the background in the previous analyses and then reopens the window for a *protophobic* vector scenario. The case of a pure axial vector has been investigated in [225] where the authors applied a multipole expansion method to the anomalous nuclear decay rates and evaluated the related nuclear matrix elements by *ab-initio* calculation using realistic nuclear forces. Their estimation concludes that the X axial coupling to quark should be order $\mathcal{O}(10^{-4} - 10^{-5})$ to explain the anomalous signal in the ^{8}Be transition. Vector with mixed parity have also attracted attention, especially in the case of more specific BSM UV construction, see *e.g.* [226–228]. Lastly, the possibility of a light pseudoscalar has been considered in [229], where the authors made a rough estimation of the range of the values of the Yukawa couplings, assuming a nuclear shell model for the ^{8}Be nucleus. The strongest constraints they reported come from flavor changing neutral current interactions as $K \to \pi X$, which however can be satisfied simultaneously explaining the ATOMKI ^{8}Be results. The interesting possibility of the QCD axion being responsible for the ATOMKI anomalies has been entertained in [230, 231], see also [232]. Here the Authors focus on a axion candidate with dominant coupling to the first generation of SM fermions and piophobic, *e.g.* with suppressed isovector coupling. It has subsequently however been pointed out in [233] that for such a scenario a large pion decay rate for $\pi \to 3X \to 3e^+3e^-$ of $\mathcal{O}(10^{-3})$ is expected, exceeding the SM double-Dalitz decay by a factor of thirty. There has been no direct measurement of this process so far, although it is reasonable to assume that such a large decay rate would have been noticed.

3.2.1 Process kinematics

The ATOMKI anomalies show simple but well defined features, which are:

- the excesses are resonant bumps located at the same e^+e^- invariant mass for all the ^{8}Be and ^{4}He transitions,
- the e^+e^- opening angles of the anomalous peaks are around 140°, 115° and 155° − 160°, respectively, for the ^{8}Be, ^{4}He and ^{12}C,
- the anomalous signal in the ^{8}Be transition have been observed only inside the kinematic region given by $|y| < 0.5$, where y is the energy asymmetry of the lepton pair, *i.e.* the ratio between the difference and the sum of their energies.

As we review below, closely following earlier results appeared in [220, 221], these features are naturally explained by the hypothesis of resonant production of a new particle.

In the experimental setup the target nucleus A is at rest in the laboratory frame, while the proton beam energy E_b is of the order of MeV, so that the colliding protons are mostly non relativistic. The Center of Mass (CM) energy $E_{\rm CM}$ is then given by

$$E_{\rm CM} = \sqrt{(m_p + m_A)^2 + 2m_A E_b} \simeq m_p + m_A + \frac{m_{pA}}{m_p} E_b \ , \tag{3.2}$$

where $m_{pA} = (m_A^{-1} + m_p^{-1})^{-1}$ is the reduce mass of the proton-target system. The experiment calibrates the beam energy in order to populate the N^* state, which is produced almost at rest in the CM frame, and then measure its IPC transition to the ground state N. We show in Table 3.2 the numerical values of the proton kinetic energy E_b, mass of the target and of the excited nucleus, reduced proton-target mass and velocity of the excited nucleus produced by the collision in the lab frame at the resonance peak ($E_{CM} = m_{N^*}$) for all the measured N^* states.

E_b [MeV]	A	m_A [MeV]	m_{pA}/m_p	N^*	m_{N^*} [MeV]	$v_{N^*}\,/\,c$
1.03	^{7}Li	6533.83	0.87	^{8}Be(18.15)	7473.01	0.0059
0.45	^{7}Li	6533.83	0.87	^{8}Be(17.64)	7472.50	0.0039
1.59	^{3}H	2808.92	0.75	^{4}He(21.01)	3748.39	0.0146
0.52	^{3}H	2808.92	0.75	^{4}He(20.21)	3747.59	0.0084
1.40	^{11}B	10252.54	0.92	^{12}C(17.23)	11192.09	0.0046

Table 3.2: Proton kinetic energy E_b, mass of the target and of the excited nucleus, reduced proton-target mass and velocity of the excited nucleus produced by the collision in the lab frame at the resonance peak ($E_{CM} = m_{N^*}$) for all the measured N^* states.

Regardless on whether the resonance is (fully) populated, the collision between the proton and the target leads to the production of the N nucleus via the emission of a boson of mass m, which could be a real or virtual photon or an hypothetical BSM particle. In the CM frame the boson energy ω is given by

$$\omega = \frac{E_{\rm CM}^2 + m^2 - m_N^2}{2E_{\rm CM}} \simeq E_{\rm th} + \frac{m_{pA}}{m_p} E_b \ , \tag{3.3}$$

where the threshold energy $E_{\rm th} = m_p + m_A - m_N$ is the energy gap between the N nucleus and the proton-target system. Note that the boson energy roughly only depends on the beam energy. Once produced the (real or virtual) boson decays into an e^+e^- pair, whose angular correlation is

the main observable measured by the ATOMKI experiment. In the CM frame the total energy of the leptons is given by $\omega = E_+ + E_-$, where $E_+(E_-)$ is the positron (electron) energy, while we label the opening angle between the leptons with $\theta_\pm$. The decay of the boson into the e^+e^- pair is controlled by the energy asymmetry

$$y = \frac{E_+ - E_-}{E_+ + E_-}, \tag{3.4}$$

while the opening angle is given by

$$\theta_\pm = \cos^{-1}\left(\frac{-1 - y^2 + \delta^2 + 2v^2}{\sqrt{(1-\delta^2+y^2)^2 - 4y^2}}\right), \tag{3.5}$$

where $\delta = 2m_e/\omega$ $(0 < \delta < 1)$ and

$$v = \sqrt{1 - \left(\frac{m}{\omega}\right)^2} \tag{3.6}$$

is the boson velocity. We show in Table 3.3 the numerical values of the threshold energy E_{th}, boson energy ω in the CM frame the velocity v_X of an hypothetical boson of mass $m_X \simeq 17$ MeV emitted in the CM frame at the resonance peak $(E_{CM} = m_{N^*})$ for all the measured N^* states.

N^*	m_N [MeV]	E_{th} [MeV]	ω [MeV]	v_X
^{8}Be(18.15)	7454.86	17.24	18.15	0.350
^{8}Be(17.64)	7454.86	17.24	17.64	0.267
^{4}He(21.01)	3727.38	19.81	21.01	0.588
^{4}He(20.21)	3727.38	19.81	20.21	0.541
^{12}C(17.23)	11174.86	15.95	17.23	0.163

Table 3.3: N mass, threshold energy E_{th}, boson energy ω in the CM frame the velocity v_X of an hypothetical boson of mass $m_X \simeq 17$ MeV emitted in the CM frame at the resonance peak $(E_{CM} = m_{N^*})$ for all the measured N^* states.

For an hypothetical X boson with mass $m_X = 17$ MeV, the maximum value of the energy asymmetry and the minimal value of the opening angle are respectively

$$y_{\max} \simeq v_X \qquad \text{and} \qquad \theta_\pm^{\min} \simeq \cos^{-1}(2v_X^2 - 1)\ . \tag{3.7}$$

In Fig. 3.1 we plot the opening angle as a function of the energy asymmetry for different values of the X boson mass around 17 MeV for all the transitions studied by ATOMKI. Note that the signal region for the ^{8}Be case is all contained in $|y| \leq 0.5$ in agreement with the ATOMKI experiment. We then show in Fig. 3.2 the normalized distribution of $\theta_\pm$, integrated over the asymmetry y, for the three nuclei considered by ATOMKI in the spin-0 boson hypotheses case, where the distribution only depends on phase space quantities. In the spin-1 case there is a dynamical dependence due to the polarization state of the X boson which can modify this distribution, which is however expected to be qualitatively similar to the spin-0 case. As we see the opening angle distributions peak at the lowest end with peak values compatible with the ones reported by the experiments. We show in Table **??** the numerical values of the maximum energy asymmetry y_{max} and minimal opening angle $\theta_\pm^{min}$ for an hypothetical boson of mass $m_X = 17$ MeV emitted in the CM frame.

Lastly, from Eq. (3.5) the invariant mass of the lepton pair reads

$$m_{ee}^2 = \frac{\omega^2}{2}\left[1 - y^2 + \delta^2 - \cos\theta_\pm\sqrt{(1-\delta^2+y^2)^2 - 4y^2}\right]\ , \tag{3.8}$$

where here $\cos\theta_\pm$ is now a free parameter independent on the energy asymmetry.

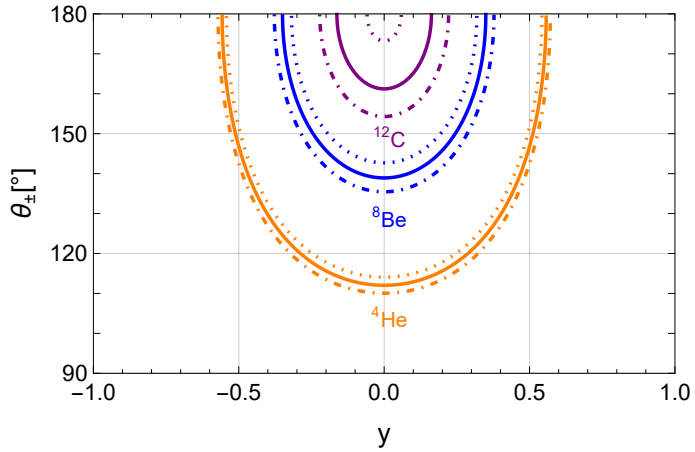

Figure 3.1: Values of the e^+e^- opening angle $\theta_\pm$ as a function of the energy asymmetry y for three values of the boson mass: $m_X = 16.8$ MeV (dot-dashed line), $m_X = 17$ MeV (solid line) and $m_X = 17.2$ MeV (dotted line) for the cases of the ^{8}Be, ^{4}He and ^{12}C transitions.

N^*	δ	$y_{\max}$	$\theta_\pm^{\min}[^\circ]$
^{8}Be(18.15)	0.056	0.351	139.0
^{8}Be(17.64)	0.058	0.267	149.0
^{4}He(21.01)	0.049	0.589	107.9
^{4}He(20.49)	0.050	0.559	112.1
^{4}He(20.21)	0.051	0.542	114.4
^{12}C(17.23)	0.059	0.163	161.2

Table 3.4: δ parameter, maximum energy asymmetry y_{max} and minimal opening angle $\theta_\pm^{min}$ for an hypothetical boson of mass $m_X = 17$ MeV emitted in the CM frame.

3.3 Signal computation: overview

In this section we describe the multipole expansion formalism used in order to estimate the anomalous nuclear decay rates relevant for the ATOMKI experiment, see also [225].

3.3.1 Nuclear states and processes

We describe the interaction of a spin s X boson to nuclear matter through the Hamiltonian

$$H^s_{\rm int} = \begin{cases} \int d^3\vec{r}\, \mathcal{S}(\vec{r}) X(\vec{r}) & \text{if } s = 0\ , \\ \int d^3\vec{r}\, \mathcal{J}_\mu(\vec{r}) X^\mu(\vec{r}) & \text{if } s = 1\ , \end{cases} \tag{3.9}$$

where the nuclear scalar density $\mathcal{S}$ and the nuclear current $\mathcal{J}^\mu = (\mathcal{J}^0, \vec{\mathcal{J}})$ are quantum operators containing all the information of the matter fields. In the case of electromagnetic interaction the nuclear current $\mathcal{J}_\mu$ is replaced by the electromagnetic current $\mathcal{J}^\gamma_\mu$, which allows for $\gamma-$emission and IPC processes. At the lowest order in the interaction picture, the nuclear matrix element for the X

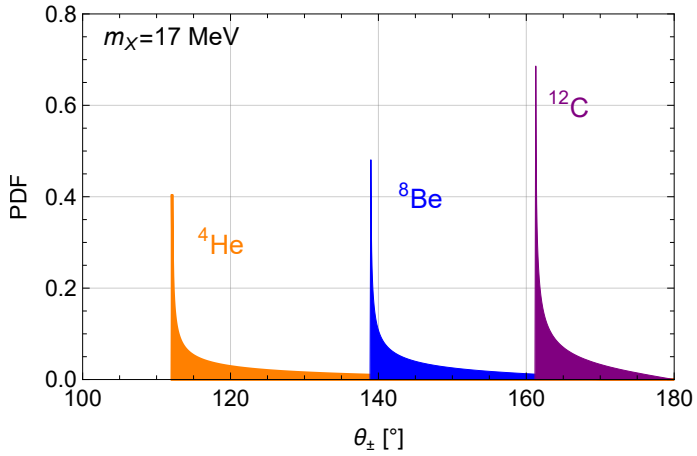

Figure 3.2: Normalized distributions of the e^+e^- opening angles from the ^{8}Be (blue), ^{4}He (orange) and ^{12}C (purple) nuclear transitions.

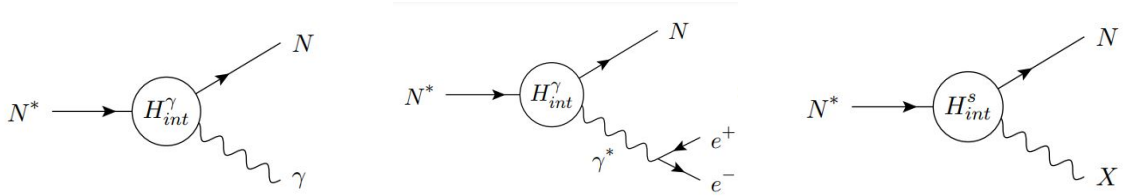

Figure 3.3: Real γ-emission (left), IPC (center) and real X-emission (right) processes for the excited N^* decay.

emission is given by

$$\mathcal{T}^s_{fi} = \langle f, X | H^s_{\rm int} | i \rangle = \begin{cases} \langle f | \int d^3\vec{r}\, \mathcal{S}(\vec{r}) e^{-i\vec{k}\cdot\vec{r}} | i \rangle & \text{if } s = 0 \ , \\ \langle f | \int d^3\vec{r}\, [\epsilon^\mu_a(\vec{k})]^* \mathcal{J}_\mu(\vec{r}) e^{-i\vec{k}\cdot\vec{r}} | i \rangle & \text{if } s = 1 \ , \end{cases} \tag{3.10}$$

where $\vec{k}$ is the boson momentum, the index $a = 0, \pm 1$ labels the polarization of the vector boson and $|i\rangle$ and $|f\rangle$ indicate the nuclear matter initial and final states which are $|f\rangle = |N; J_f M_f\rangle$ and $|i\rangle = |p + A; J_p M_p; J_A M_A; \vec{p}_{\rm CM}\rangle$, where $\vec{p}_{\rm CM}$ is the proton momentum in the CM frame. We employ the narrow width approximation and factorize the excited resonance production from its decay, thereby assuming that the initial state is described by $|i_*\rangle = |N^*; J_* M_*\rangle$. In the following we want to compute the decay widths of the excited N^* states for real X emission in order to compare to the experimental results on this quantity reported by the ATOMKI collaboration. To make the calculation, it will turn out to be useful to expand the nuclear matrix elements in terms of spherical tensor operators, which will allow to also compute the electromagnetic real γ-emission and IPC processes, which we report in App. 3.4. The diagrams for these three processes are shown in Fig. 3.3. To perform the calculation we will expand the nuclear matrix elements in terms of spherical tensor operators through a multipole expansion.

3.3.2 Multipole expansion

Spherical operators $\mathcal{O}_{JM}$ are irreducible tensor operators which satisfy the Wigner-Eckart theorem [234]

$$\langle J_f M_f | O_{J,-M} | J_i M_i \rangle = \frac{(-1)^{J_i - M_i}}{\sqrt{2J+1}} \langle J_f M_f; J_i, -M_i | J_f J_i; J, -M \rangle \langle J_f || O_J || J_i \rangle . \tag{3.11}$$

The reduced matrix element $\langle J_f || O_J || J_i \rangle$ contains all the physical information of the operator while its behavior under rotation is completely set by the Clebsh-Gordan coefficient $C^{J-M}_{J_f M_f J_i - M_i}$. We define the spherical operators[1]

$$\mathcal{G}_{JM} = \int d^3\vec{r}\, j_J(kr) Y_{JM}(\hat{r}) \mathcal{S}(\vec{r}) , \tag{3.12}$$

$$\mathcal{M}_{JM} = \int d^3\vec{r}\, j_J(kr) Y_{JM}(\hat{r}) \mathcal{J}^0(\vec{r}) , \tag{3.13}$$

$$\mathcal{L}_{JM} = \frac{i}{k} \int d^3\vec{r}\, \vec{\nabla}[j_J(kr) Y_{JM}(\hat{r})] \cdot \vec{\mathcal{J}}(\vec{r}) , \tag{3.14}$$

$$\mathcal{T}^{\rm el}_{JM} = \frac{1}{k} \int d^3\vec{r}\, \vec{\nabla} \times [j_J(kr) \mathbf{Y}_{JJM}(\hat{r})] \cdot \vec{\mathcal{J}}(\vec{r}) , \tag{3.15}$$

$$\mathcal{T}^{\rm mag}_{JM} = \int d^3\vec{r}\, [j_J(kr) \mathbf{Y}_{JJM}(\hat{r})] \cdot \vec{\mathcal{J}}(\vec{r}) , \tag{3.16}$$

where $r = |\vec{r}|$ and expand the nuclear matrix elements as a sum of reduced matrix elements of spherical operators. In the case of interest of the emission of the X boson in the process $N^* \to N + X$ one finds

$$\mathcal{T}^{s=0}_{f i_*} = \sum_{\substack{J\geq 0,\\ |M|\leq J}} (-i)^J \sqrt{4\pi} C^{J-M}_{J_f M_f J_* - M_*} \langle f || \mathcal{G}_J || i_* \rangle D^{(J)}_{-M,0}(\phi, \theta, \beta) , \tag{3.17}$$

$$\begin{aligned} \mathcal{T}^{s=1}_{f i_*} = & \sum_{\substack{J\geq 0,\\ |M|\leq J}} (-i)^J \sqrt{4\pi} \delta_{a0} C^{J-M}_{J_f M_f J_* - M_*} \langle f || \left[\frac{k}{m} \mathcal{M}_J - \frac{\omega}{m} \mathcal{L}_J \right] || i_* \rangle D^{(J)}_{-M,-a}(\phi, \theta, \beta) + \\ & - \sum_{\substack{J\geq 1,\\ |M|\leq J,\\ \lambda = \pm 1}} (-i)^J \sqrt{2\pi} \delta_{a\lambda} C^{J-M}_{J_f M_f J_* - M_*} \langle f || \left[\mathcal{T}^{el}_J + \lambda \mathcal{T}^{mag}_J \right] || i_* \rangle D^{(J)}_{-M,-a}(\phi, \theta, \beta) , \end{aligned} \tag{3.18}$$

where here the indices J and M denote the total angular momentum of the emitted boson (sum of its spin and relative angular momentum with the N nucleus) and its projection. The rotation D matrices play the role of the wave function[2], whose moduli squared give the probability for the X boson to be emitted in the (ϕ, θ) direction with β defining a rotation along this direction[3]. An

[1] Y_{JM}, $j_J(x)$ and $\mathbf{Y}_{J\ell M}(\hat{r})$ are respectively the spherical harmonics, the vector Bessel functions and the vector spherical harmonics, see [234].

[2] See [234] for the definition of the the D functions.

[3] For the emission of a real boson, the angle β is unphysical since it vanishes once the amplitudes are squared. It become physical in the IPC process.

explicit calculation for the unpolarized decays gives

$$\Gamma_X^{s=0} = \frac{2k}{2J_*+1}\left\{\sum_{J\geq 0}|\langle f||\mathcal{G}_J||i_*\rangle|^2\right\}\,, \tag{3.19}$$

$$\Gamma_X^{s=1} = \frac{2k}{2J_*+1}\left\{\sum_{J\geq 0}\left|\langle f||\left[\frac{k}{m}\mathcal{M}_J - \frac{\omega}{m}\mathcal{L}_J\right]||i_*\rangle\right|^2 + \sum_{J\geq 1}\left[\left|\langle f||\mathcal{T}_J^{el}||i_*\rangle\right|^2 + |\langle f||\mathcal{T}_J^{mag}||i_*\rangle|^2\right]\right\}\,. \tag{3.20}$$

In the case where the vector boson is coupled to a conserved current, *i.e.* $\partial^\mu \mathcal{J}_\mu = 0$, a simplification occurs. By assuming the nuclear initial and final state to be eigenstates of the nuclear Hamiltonian the continuity equation $\vec{\nabla}\cdot\vec{\mathcal{J}} = -\frac{\partial \mathcal{J}^0}{\partial t}$ yields

$$\omega\,\langle f||\mathcal{M}_J||i_*\rangle = k\,\langle f||\mathcal{L}_J||i_*\rangle\ \,, \tag{3.21}$$

and the partial width for the emission of a vector X boson then reduces to

$$\Gamma_X^{s=1} = \frac{2k}{2J_*+1}\left\{\left(\frac{m}{k}\right)^2\sum_{J\geq 0}|\langle f||\mathcal{M}_J||i_*\rangle|^2 + \sum_{J\geq 1}\left[\left|\langle f||\mathcal{T}_J^{\rm el}||i_*\rangle\right|^2 + |\langle f||\mathcal{T}_J^{\rm mag}||i_*\rangle|^2\right]\right\}\,. \tag{3.22}$$

The above results are equally useful for the electromagnetic processes once we substitute the electromagnetic current in the spherical operators and put $m_\gamma = 0$, *i.e.* $k = \omega$.

Selection rules

The angular momentum conservation law, encoded in the Clebsh-Gordan coefficient of Eq. (3.11), states that the matrix element of the spherical operators vanishes unless the following conditions are satisfied

$$\begin{aligned} &|J_f - J_*| \leq J \leq J_f + J_*\,, \\ &M = M_* - M_f\,. \end{aligned} \tag{3.23}$$

Moreover, if the X boson has a definite parity π_X, additional constraints on the matrix elements come from the requirement of parity conservation. By denoting the relative angular momentum between the boson and N as L, one has

$$\pi_* = \pi_f \pi_X (-1)^L\,. \tag{3.24}$$

We report in Tab. 3.5 the relative angular momentum between the X boson and N in the various decay processes, based on the S^π spin-parity assignments. One sees that a pure scalar solution to the ^{8}Be anomaly is excluded, while a pseudoscalar state can explain only the ^{8}Be and ^{4}He anomaly, if the latter is dominated by the ^{4}He(21.01) excited state transition, but not the ^{12}C one. On the other side a vector or axial-vector candidate can simultaneously explain all the three anomalies, but again only one of the two ^{4}He resonant states can contribute to the signal process.

3.3.3 Long wavelength approximation

The nuclear radius is approximately given by $R \simeq R_0 A^{\frac{1}{3}} \simeq 6.1\times 10^{-3} A^{\frac{1}{3}}$ MeV^{-1} [235], which implies that in all the cases of interest the nucleus size is significantly smaller than the boson wavelength $k^{-1} \sim (10\text{ MeV})^{-1}$. We can thus expand the spherical Bessel function for small kr as

$$j_J(kr) \simeq \frac{(kr)^J}{(2J+1)!!}\,, \tag{3.25}$$

Process $N^* \to N$	X **boson spin parity** $S^\pi = 1^-$	$S^\pi = 1^+$	$S^\pi = 0^-$	$S^\pi = 0^+$
^{8}Be(18.15) $\to$ ^{8}Be	1	0, 2	1	/
^{8}Be(17.64) $\to$ ^{8}Be	1	0, 2	1	/
^{4}He(21.01) $\to$ ^{4}He	/	1	0	/
^{4}He(20.21) $\to$ ^{4}He	1	/	/	0
^{12}C(17.23) $\to$ ^{12}C	0, 2	1	/	1

Table 3.5: Relative angular momentum between the X boson and N in the various decays, based on its possible parity-spin assignments. Note that parity conservation prohibits a pure scalar solution to the Beryllium anomaly.

with higher order corrections giving a contribution of order $(kr)^2 \simeq 1\%$ with respect to the leading one for the cases of interest, which can therefore be neglected. For the spherical operators $\mathcal{M}_{JM}$, $\mathcal{L}_{JM}$ and $\mathcal{G}_{JM}$ the expressions of Eq. (3.12), Eq. (3.13) and Eq. (3.14) then read

$$\mathcal{G}_{JM} \simeq \frac{k^J}{(2J+1)!!} \int d^3\vec{r}\, r^J Y_{JM} \mathcal{S}(\vec{r}) \ , \tag{3.26}$$

$$\mathcal{M}_{JM} \simeq \frac{k^J}{(2J+1)!!} \int d^3\vec{r}\, r^J Y_{JM} \mathcal{J}^0(\vec{r}), \tag{3.27}$$

$$\mathcal{L}_{JM} \simeq \frac{1}{i} \frac{k^{J-1}}{(2J+1)!!} \int d^3\vec{r}\, r^J Y_{JM} \vec{\nabla} \cdot \vec{\mathcal{J}}(\vec{r}) \ . \tag{3.28}$$

An exception occurs for the monopole case $\mathcal{L}_{00}$, since it identically vanish at this order. The first contribution thus arises at the next order in the kr expansion and is given by

$$\mathcal{L}_{00} \simeq \frac{ik}{6} \int d^3\vec{r}\, r^2 Y_{00} \vec{\nabla} \cdot \vec{\mathcal{J}}(\vec{r}) \ . \tag{3.29}$$

The second order expansion is also needed for the $\mathcal{M}_{00}$ monopole expression in the case of a conserved current. This is due to the fact that in this case the integral over space of $\mathcal{J}^0(\vec{r})$ defines the generator Q of the symmetry associated with it. Then, with $|i\rangle$ and $|f\rangle$ orthogonal eigenstates of the Hamiltonian, one as $\langle f|Q|i\rangle \propto \langle f|i\rangle = 0$. It follows that the first contribution to the operator $\mathcal{M}_{00}$ is given by

$$\mathcal{M}_{00} \simeq -\frac{k^2}{6} \int d^3\vec{r}\, r^2 Y_{00} \mathcal{J}^0(\vec{r}) \ . \tag{3.30}$$

Let's now consider the operators $\mathcal{T}^{\rm el}_{JM}$ and $\mathcal{T}^{\rm mag}_{JM}$ of Eq. (3.15) and Eq. (3.16). By using the identity

$$\mathbf{L} Y_{JM} = -i(\vec{r} \times \vec{\nabla}) Y_{JM} = \sqrt{J(J+1)} \mathbf{Y}_{JJM} \ , \tag{3.31}$$

they can be rewritten at the first order in the kr expansion as [235]

$$\mathcal{T}^{\rm mag}_{JM} \simeq \frac{ik^J}{(2J+1)!!} \sqrt{\frac{J+1}{J}} \int d^3\vec{r} \left\{ \vec{\mu}(\vec{r}) + \frac{1}{J+1} \vec{r} \times \vec{J}_{irr}(\vec{r}) \right\} \cdot \vec{\nabla}(r^J Y_{JM}), \tag{3.32}$$

$$\mathcal{T}^{\rm el}_{JM} \simeq \frac{1}{i} \frac{k^{J-1}}{(2J+1)!!} \sqrt{\frac{J+1}{J}} \int d^3\vec{r} \left\{ \vec{\nabla} \cdot \vec{J}_{\rm irr}(\vec{r}) + \frac{k^2}{J+1} \vec{\nabla} \cdot [\vec{r} \times \vec{\mu}(\vec{r})] \right\} r^J Y_{JM} \ , \tag{3.33}$$

Spin-1 case

	$\mathcal{J}^0(\vec{r})$	$\vec{\mathcal{J}}_{\rm irr}(\vec{r})$	$\vec{\mu}(\vec{r})$
$C_p\bar{p}\gamma^\mu p + C_n\bar{n}\gamma^\mu n$	$\sum_{j=1}^A C_j\delta_{\vec{r},\vec{r}_j}$	$\sum_{j=1}^A \frac{C_j}{2m_j}\{\vec{p}_j,\delta_{\vec{r},\vec{r}_j}\}$	$\sum_{j=1}^A \frac{C_j}{2m_j}\vec{\sigma}_j\delta_{\vec{r},\vec{r}_j}$
$a_p\bar{p}\gamma^\mu\gamma^5 p + a_n\bar{n}\gamma^\mu\gamma^5 n$	$\sum_{j=1}^A \frac{a_j}{2m_j}\{\vec{\sigma}_j\cdot\vec{p}_j,\delta_{\vec{r},\vec{r}_j}\}$	$\sum_{j=1}^A a_j\vec{\sigma}_j\delta_{\vec{r},\vec{r}_j}$	/
$\frac{\kappa_p}{2m_p}\partial_\nu(\bar{p}\sigma^{\mu\nu}p) + \frac{\kappa_n}{2m_n}\partial_\nu(\bar{n}\sigma^{\mu\nu}n)$	/	/	$\sum_{j=1}^A \frac{\kappa_j}{2m_j}\vec{\sigma}_j\delta_{\vec{r},\vec{r}_j}$

Spin-0 case

	$\mathcal{S}(\vec{r})$
$z_p\bar{p}p + z_n\bar{n}n$	$\sum_{j=1}^A z_j\delta_{\vec{r},\vec{r}_j}$
$h_p i\bar{p}\gamma^5 p + h_n i\bar{n}\gamma^5 n$	$\sum_{j=1}^A \frac{h_j}{2m_j}\vec{\sigma}_j\cdot\vec{\nabla}[\delta_{\vec{r},\vec{r}_j}]$

Table 3.6: Leading term of the non relativistic expansion for the relativistic vector current, the relativistic axial current and the anomalous magnetic moment terms (upper table) and for the scalar and pseudoscalar density (lower table). $\delta_{\vec{r},\vec{r}_j} = \delta(\vec{r}-\vec{r}_j)$.

where the vector current has been split into an irrotational field $\vec{\mathcal{J}}_{\rm irr}$ and a solenoidal field $\vec{\nabla}\times\vec{\mu}$ as $\vec{\mathcal{J}} = \vec{\mathcal{J}}_{\rm irr} + \vec{\nabla}\times\vec{\mu}$ in virtue of the Helmholtz's theorem. For a conserved current, the matrix element expression of $\mathcal{T}_J^{\rm el}$ can be simplified to

$$\langle f|\mathcal{T}^{\rm el}_{JM}|i_*\rangle \simeq \langle f|\frac{k^J}{(2J+1)!!}\sqrt{\frac{J+1}{J}}\int d^3\vec{r}\left\{\frac{\omega}{k}r^J Y_{JM}\mathcal{J}^0(\vec{r}) - \frac{ik}{J+1}\vec{\mu}(\vec{r})\cdot[\vec{r}\times\vec{\nabla}(r^J Y_{JM})]\right\}|i_*\rangle \ , \tag{3.34}$$

by again using the continuity equation.

3.3.4 Non relativistic expansion for nuclear operators

Through statistical considerations [236], the maximal kinetic energy $E_{\rm c}$ per nucleon in the nucleus is estimated to be around 30 MeV, implying that a nucleus can be then modeled as a quantum mechanical system of non relativistic point-like nucleons [235]. One can then take the non relativistic limit of the nuclear operator and write it in first quantization formalism. The nuclear operator is given by

$$\mathcal{O}(\vec{r}) = \sum_{i=1}^A \hat{\mathcal{O}}_i^{(1)}(\vec{r}-\vec{r}_i) \ , \tag{3.35}$$

with the single particle operator $\hat{\mathcal{O}}_i^{(1)}(\vec{r}-\vec{r}_i) \propto \delta(\vec{r}-\vec{r}_i)$ in the nucleon point-like approximation. We want to match the expression of Eq. (3.35) with its relativistic counterpart, where the nucleons are described in terms of quantum fields $p(x)$ and $n(x)$ and the nucleon operators are bilinears in $p(x)$ and $n(x)$. We report in Tab. 3.6 the leading terms of the non relativistic expansion for the vector current, axial current, anomalous magnetic moment, scalar and pseudoscalar densities. For operators which are even or odd under parity, as it is in our case, higher order terms in the expansions are of order of $\frac{p_N^2}{m_N^2} \sim 6\times10^{-2}$ with respect to the leading one, and can then be safely neglected. For the specific case of the pseudoscalar density one also has that

$$\lim_{p'\to p}\bar{u}(p')\gamma^5 u(p) = 0 \ , \tag{3.36}$$

where u are the spinors which enter the quantum field expression. Hence the non relativistic expansion of the pseudoscalar current only contains terms proportional to $\vec{k} = \vec{p} - \vec{p}'$. Since for the effective non relativistic operator it holds the substitution [235]

$$i\vec{\nabla} \to \vec{k} \tag{3.37}$$

the non relativistic expansion of the pseudoscalar density only contains operators given by a total divergence, meaning that the pseudoscalar density is a derivative coupling. The monopole operator $\mathcal{G}_{00}$ then vanishes at first order in the long-wavelength expansion and the leading contribution is then given by

$$\mathcal{G}_{00} \simeq -\frac{k^2}{6} \int d^3\vec{r}\, r^2 Y_{00} \mathcal{S}(\vec{r}) \ . \tag{3.38}$$

The techniques introduced in this section will be implemented in the next to derive the theoretical decay rates of the nuclear transitions.

3.4 Electromagnetic dynamics

With the formalism described in Sec. 3.3 we can describe the dynamics for the SM processes pictured in Fig. 3.3 of real γ emission and IPC. The nuclear electromagnetic current, including the anomalous magnetic moments, is given by

$$\mathcal{J}^{(\gamma)}_{\mu} = eQ_p \bar{p}\gamma_\mu p + eQ_n \bar{n}\gamma_\mu n + \frac{e\kappa^\gamma_p}{2m_p}\partial^\nu(\bar{p}\sigma_{\mu\nu}p) + \frac{e\kappa^\gamma_n}{2m_n}\partial^\nu(\bar{n}\sigma_{\mu\nu}n), \tag{3.39}$$

where $\kappa_p = +1.792847351(28)$, $\kappa_n = -1.9130427(5)$ [235] and $Q_{p,n}$ indicates the electric charge of the nucleon in units of the absolute electron charge. The magnetic momenta of the nucleons are

$$\mu_{p,n} = (Q_{p,n} + \kappa^\gamma_{p,n})\mu_{\mathcal{N}} \ , \tag{3.40}$$

where $\mu_{\mathcal{N}} = e/2m_{\mathcal{N}}$ is the nuclear magneton. The conservation of the electromagnetic current implies that only three independent spherical operators have to be considered, *c.f.r.* Eq. (3.21). In the non relativistic and long wavelength approximation the spherical operators with $J = 0, 1$ are given by

$$\mathcal{M}^{(\gamma)}_{00} \simeq -\frac{ek^2}{6}\rho^{(\gamma)} \ , \tag{3.41}$$

$$\mathcal{M}^{(\gamma)}_{1M} \simeq \frac{ek}{3} d^{(\gamma)}_M \ , \tag{3.42}$$

$$\mathcal{T}^{\mathrm{el}(\gamma)}_{1M} \simeq \frac{\sqrt{2}e\omega}{3} d^{(\gamma)}_M \ , \tag{3.43}$$

$$\mathcal{T}^{\mathrm{mag}(\gamma)}_{1M} \simeq \frac{i\sqrt{2}k\mu_{\mathcal{N}}}{3} \mu^{(\gamma)}_M \ , \tag{3.44}$$

where we have defined the electromagnetic monopole $\rho^{(\gamma)}$, the electric dipole $d_M^{(\gamma)}$ and the magnetic moment $\mu_M^{(\gamma)}$ operators as

$$\rho^{(\gamma)} = \frac{1}{\sqrt{4\pi}} \sum_{s=1}^{A} Q_s r_s^2 \ , \tag{3.45}$$

$$d_M^{(\gamma)} = \sqrt{\frac{3}{4\pi}} \sum_{s=1}^{A} Q_s \vec{r}_s \cdot \hat{e}_M \ , \tag{3.46}$$

$$\mu_M^{(\gamma)} = \sqrt{\frac{3}{4\pi}} \sum_{s=1}^{A} [Q_s(\vec{r}_s \times \vec{p}_s) + (Q_s + \kappa_s^{\gamma})\vec{\sigma}_s] \cdot \hat{e}_M \ . \tag{3.47}$$

3.4.1 Real γ emission

The rate for the process with a real γ emission can be readily computed from Eq. (3.22) by fixing $m_\gamma = 0$. In this case, due to the transversality of the photon, only processes with $J = 0$ are allowed which are

- electric type transitions EJ from the contribution of $\mathcal{T}_J^{\rm el}$ with parity $\pi(EJ) = (-1)^J$,
- magnetic type transitions MJ from the contribution of $\mathcal{T}_J^{\rm mag}$ with parity $\pi(MJ) = (-1)^{J+1}$.

The $E1$ and $M1$ decay rates are equal to

$$\Gamma_\gamma^{E1} = \frac{16\pi\alpha\omega^3}{9(2J_*+1)} |\langle f||d^{(\gamma)}||i_*\rangle|^2, \tag{3.48}$$

$$\Gamma_\gamma^{M1} = \frac{4\mu_N^2\omega^3}{9(2J_*+1)} |\langle f||\mu^{(\gamma)}||i_*\rangle|^2. \tag{3.49}$$

3.4.2 Internal pair creation

At lowest order the IPC process involves the emission of a virtual photon decaying into an e^+e^- pair. The differential decay rate with respect to the energy asymmetry y and the opening angle $\theta_\pm$ is given by

$$\begin{aligned} \frac{d^2\Gamma_\pm}{dy\, d\cos\theta_\pm} = \frac{2\omega}{2J_*+1}\frac{\alpha}{4\pi}\Bigg\{ & f_{\mathcal{M}}(y,\cos\theta_\pm,\delta) \sum_{J\geq 0} |\langle f||\mathcal{M}_J||i_*\rangle|^2 \\ & + f_{\mathcal{T}}(y,\cos\theta_\pm,\delta) \sum_{J\geq 1} \left[\left|\langle f||\mathcal{T}_J^{el}||i_*\rangle\right|^2 + |\langle f||\mathcal{T}_J^{mag}||i_*\rangle|^2 \right] \Bigg\} \ , \end{aligned} \tag{3.50}$$

where the $f_{\mathcal{M},\mathcal{T}}(y,\cos\theta_\pm,\delta)$ functions are

$$f_{\mathcal{M}}(y,c,\delta)=\frac{\sqrt{(1-\delta^2+y^2)^2-4y^2}\left[1-y^2-\delta^2+c\sqrt{(1-\delta^2+y^2)^2-4y^2}\right]}{\left[1+y^2-\delta^2+c\sqrt{(1-\delta^2+y^2)^2-4y^2}\right]^2}, \tag{3.51}$$

$$\begin{aligned} f_{\mathcal{T}}(y,c,\delta)=&\frac{1}{2}\frac{\sqrt{(1-\delta^2+y^2)^2-4y^2}}{\left[1+y^2-\delta^2+c\sqrt{(1-\delta^2+y^2)^2-4y^2}\right]}\times\\ \times&\frac{\left[\left(1-3y^2+3\delta^2-c\sqrt{(1-\delta^2+y^2)^2-4y^2}\right)\left(1+y^2-\delta^2+c\sqrt{(1-\delta^2+y^2)^2-4y^2}\right)+4y^2\right]}{\left[1-y^2+\delta^2-c\sqrt{(1-\delta^2+y^2)^2-4y^2}\right]^2}. \end{aligned} \tag{3.52}$$

Note that IPC processes acquire a contribution also from the longitudinal modes, absent in the real γ emission case. Hence, processes of pair production are of three types:

- longitudinal type transition LJ from the contribution of $\mathcal{M}_J$ with parity $\pi(LJ)=(-1)^J$,
- electric transition EJ from the contribution of $\mathcal{T}^{\rm el}_J$ with parity $\pi(EJ)=(-1)^J$,
- magnetic transition MJ from the contribution of $\mathcal{T}^{\rm mag}_J$ with parity $\pi(MJ)=(-1)^{J+1}$,

with differential decay rates[4]

$$\frac{d^2\Gamma^{L0}_\pm}{dy\,d\cos\theta_\pm}=\frac{\alpha^2\omega^5}{72(2J_*+1)}\zeta^2(y,\delta,\cos\theta_\pm)f_{\mathcal{M}}(y,\cos\theta_\pm,\delta)|\,\langle f||\rho^{(\gamma)}||i_*\rangle\,|^2\ , \tag{3.53}$$

$$\frac{d^2\Gamma^{L1}_\pm}{dy\,d\cos\theta_\pm}=\frac{\alpha}{16\pi}\zeta(y,\delta,\cos\theta_\pm)f_{\mathcal{M}}(y,\cos\theta_\pm,\delta)\Gamma^{E1}_\gamma\ , \tag{3.54}$$

$$\frac{d^2\Gamma^{E1}_\pm}{dy\,d\cos\theta_\pm}=\frac{\alpha}{4\pi}f_{\mathcal{T}}(y,\cos\theta_\pm,\delta)\Gamma^{E1}_\gamma\ , \tag{3.55}$$

$$\frac{d^2\Gamma^{M1}_\pm}{dy\,d\cos\theta_\pm}=\frac{\alpha}{8\pi}\zeta(y,\delta,\cos\theta_\pm)f_{\mathcal{T}}(y,\cos\theta_\pm,\delta)\Gamma^{M1}_\gamma\ . \tag{3.56}$$

We show in Fig. 3.4 the theoretical distributions of the angular correlation, obtained after integrating the above expressions over the asymmetry y.

The reduced invariant mass of the lepton pair is a function of the energy asymmetry and opening angle. Given the (normalized) distribution function $f(y,\cos\theta_\pm,\delta)$ of the pairs over the plane defined by y and $\cos\theta_\pm$, the (normalized) distribution function $g(s,\delta)$ of the reduced invariant mass is given by

$$\begin{aligned} g(s,\delta)&=\int_{-1+\delta}^{1-\delta}dy\int_{-1}^{1}d\cos\theta_\pm\,\delta\left(s-1+y^2-\delta^2+\cos\theta_\pm\sqrt{(1-\delta^2+y^2)^2-4y^2}\right)\,f(y,\cos\theta_\pm,\delta)\\ &=\int_{-\sqrt{(2-s)(s-2\delta^2)/2s}}^{\sqrt{(2-s)(s-2\delta^2)/2s}}dy\,\frac{1}{\sqrt{(1-\delta^2+y^2)^2-4y^2}}f\left(y,\frac{1-y^2+\delta^2-s}{\sqrt{(1-\delta^2+y^2)^2-4y^2}},\delta\right)\ , \end{aligned} \tag{3.57}$$

where $s=\frac{2m^2_{ee}}{\omega^2}$ $(2\delta^2\le s\le 2)$ is the reduced invariant mass. For the $J=0,1$ multipoles we calculated, the integration over the energy asymmetry is easily performed since the integrand turns

[4] $\zeta(y,\delta,\cos\theta_\pm)=1+y^2-\delta^2+\cos\theta_\pm\sqrt{(1-\delta^2+y^2)^2-4y^2}$

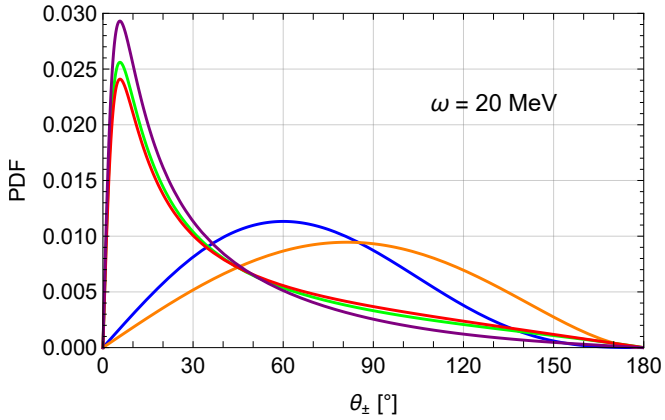

Figure 3.4: Normalized angular correlation distributions of the e^+e^- pair from the various multipole contribution to the IPC process: $L0$ (blue), $L1$ (orange), $E1$ (green), $E1+L1$ (red), $M1$ (purple).

out to be polynomial in y. Hence, one finds

$$g^{L0}(s,\delta) = \mathcal{N}_{L0}(\delta)\,(2-s)^{3/2}s^{-3/2}(s-2\delta^2)^{1/2}(s+\delta^2)$$
$$\text{with} \quad \mathcal{N}_{L0}^{-1}(\delta) = \int_{2\delta^2}^{2} dx\,(2-x)^{3/2}x^{-3/2}(x-2\delta^2)^{1/2}(x+\delta^2)\ , \tag{3.58}$$
$$g^{L1}(s,\delta) = \mathcal{N}_{L1}(\delta)\,(2-s)^{1/2}s^{-3/2}(s-2\delta^2)^{1/2}(s+\delta^2)$$
$$\text{with} \quad \mathcal{N}_{L1}^{-1}(\delta) = \int_{2\delta^2}^{2} dx\,(2-x)^{1/2}x^{-3/2}(x-2\delta^2)^{1/2}(x+\delta^2)\ , \tag{3.59}$$
$$g^{E1}(s,\delta) = \mathcal{N}_{E1}(\delta)\,(2-s)^{1/2}s^{-5/2}(s-2\delta^2)^{1/2}(s+\delta^2)$$
$$\text{with} \quad \mathcal{N}_{E1}^{-1}(\delta) = \int_{2\delta^2}^{2} dx\,(2-x)^{1/2}x^{-5/2}(x-2\delta^2)^{1/2}(x+\delta^2)\ , \tag{3.60}$$
$$g^{E1+L1}(s,\delta) = \mathcal{N}_{E1+L1}(\delta)\,(2-s)^{1/2}s^{-5/2}(s-2\delta^2)^{1/2}(s+\delta^2)(s+4)$$
$$\text{with} \quad \mathcal{N}_{E1+L1}^{-1}(\delta) = \int_{2\delta^2}^{2} dx\,(2-x)^{1/2}x^{-5/2}(x-2\delta^2)^{1/2}(x+\delta^2)(x+4)\ , \tag{3.61}$$
$$g^{M1}(s,\delta) = \mathcal{N}_{M1}(\delta)\,(2-s)^{3/2}s^{-5/2}(s-2\delta^2)^{1/2}(s+\delta^2)$$
$$\text{with} \quad \mathcal{N}_{M1}^{-1}(\delta) = \int_{2\delta^2}^{2} dx\,(2-x)^{3/2}x^{-5/2}(x-2\delta^2)^{1/2}(x+\delta^2)\ . \tag{3.62}$$

We show in Fig. 3.5 their theoretical distributions.

3.4.3 Isospin mixing and electromagnetic nuclear matrix elements

The ^{8}Be(18.15) and ^{8}Be(17.64) states, close in energy and with same spin-parity assignment, presents a significant isospin mixing. In general, given a doublet of nuclear energy levels of spin J with mixed isospin, the physical states (denoted with a and b) are given by a linear combination of states with fixed isospin

$$\Psi_a^J = \alpha_J \Psi_{I=0}^J + \beta_J \Psi_{I=1}^J, \quad \Psi_b^J = -\alpha_J \Psi_{I=1}^J + \beta_J \Psi_{I=0}^J \tag{3.63}$$

where a labels the lowest energy level between them. The coefficients α_J and β_J are real and satisfy $\alpha_J^2 + \beta_J^2 = 1$. For the ^{8}Be nucleus, the values of the mixing coefficients have been evaluated through

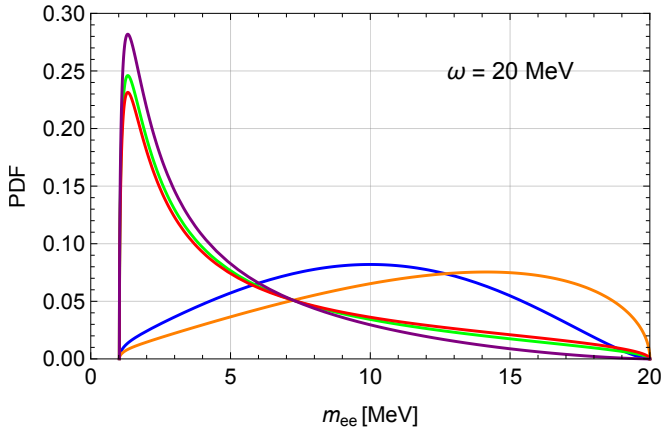

Figure 3.5: Normalized invariant mass distributions of the e^+e^- pair from the various multipole contribution to the IPC process: $L0$ (blue), $L1$ (orange), $E1$ (green), $E1 + L1$ (red), $M1$ (purple).

Quantum Monte Carlo simulation [237]. The result for the $J = 1$ doublet is

$$\alpha_1 = 0.21(3), \quad \beta_1 = 0.98(1). \tag{3.64}$$

According to this, we define the isospin magnetic strength $M1^\gamma_{I=0,1}$ by

$$\begin{aligned} \langle {}^8\text{Be}||\mu^{(\gamma)}||{}^8\text{Be}(17.64)\rangle &= \alpha_1 M1^\gamma_{I=0} + \beta_1 M1^\gamma_{I=1}, \\ \langle {}^8\text{Be}||\mu^{(\gamma)}||{}^8\text{Be}(18.15)\rangle &= -\alpha_1 M1^\gamma_{I=1} + \beta_1 M1^\gamma_{I=0}. \end{aligned} \tag{3.65}$$

whose values has been estimated to be [237]

$$M1^\gamma_{I=0} = 0.014(1), \quad M1^\gamma_{I=1} = 0.767(9). \tag{3.66}$$

At this level, a direct comparison with the experimental values of the decay lengths shows a significant discrepancies with the theoretical prediction. Following [220], we'll consider the deficiency as due to isospin breaking effects we neglected in the first attempt. The inclusion of them is obtained trough the introduction of a $\Delta I = 1$ spurion, whose effective result is to shift the nuclear matrix elements as

$$\begin{aligned} \langle {}^8\text{Be}||\mu^{(\gamma)}||{}^8\text{Be}(17.64)\rangle &= \alpha_1 M1^\gamma_{I=0} + \beta_1 M1^\gamma_{I=1} + \alpha_1 \xi M1^\gamma_{I=1}, \\ \langle {}^8\text{Be}||\mu^{(\gamma)}||{}^8\text{Be}(18.15)\rangle &= -\alpha_1 M1^\gamma_{I=1} + \beta_1 M1^\gamma_{I=0} + \beta_1 \xi M1^\gamma_{I=1}. \end{aligned} \tag{3.67}$$

The parameter ξ characterizes the strength of the spurion and its size is controlled by non-perturbative effects. One finds $\xi = 0.549$ by requiring that the resulting decay width $\Gamma({}^8\text{Be}(17.64) \to {}^8\text{Be} + \gamma)$ reproduces its experimental value. For $\xi = 0$ the isospin breaking effects are simply neglected.
Parity conservation prohibits electromagnetic interaction in the ^{4}He(21.01) transition to the ground state, thus the nuclear matrix element relative to this decay is equal to zero.
Due to the massless nature of the photon, the γ-emission decay width of the ^{4}He(20.21) transition to the ground state also vanishes but the IPC process is still possible. Pair production is mediated by the monopole operator $\rho^{(\gamma)}$, whose matrix element has been measured to be [202]

$$\sqrt{4\pi}\,\langle {}^4\text{He}||\rho^{(\gamma)}||{}^4\text{He}(20.21)\rangle = (1.10 \pm 0.16)\,\text{fm}^2, \tag{3.68}$$

with corresponding decay length, after integrating (3.53), equal to $\Gamma_\pm = (3.3 \pm 1.0) \times 10^{-4}$ eV.

The γ-emission decay length of the ^{12}C(17.23) transition to the ground state has been measured to be $\Gamma_\gamma = 44$ eV [204]. Hence, from (3.48), one finds

$$\langle {}^{12}\mathrm{C}||d^{(\gamma)}||{}^{12}\mathrm{C}(17.23)\rangle = 0.157\,\mathrm{fm}\ . \tag{3.69}$$

3.5 Signal computation: X dynamics

With the formalism described in the previous section we are now ready to describe the BSM dynamics of e^+e^- emission from the X boson, illustrated in Fig. 3.3. We refer to App. 3.4 for the details of the SM processes of real γ emission and IPC. We parametrize the interaction of the X boson with the scalar density $\mathcal{S}$ for the spin-0 case and the nuclear current $\mathcal{J}^\mu$ for the spin-1 cases in terms of effective couplings as[5,6]

$$\mathcal{L}_{S^\pi=0^+} = z_p \bar{p} p X + z_n \bar{n} n X\ , \tag{3.70}$$

$$\mathcal{L}_{S^\pi=0^-} = i h_p \bar{p}\gamma^5 p X + i h_n \bar{n}\gamma^5 n X\ , \tag{3.71}$$

$$\mathcal{L}_{S^\pi=1^-} = C_p \bar{p}\gamma^\mu p X_\mu + C_n \bar{n}\gamma^\mu n X_\mu + \frac{\kappa_p}{2m_p}\partial_\nu(\bar{p}\sigma^{\mu\nu}p)X_\mu + \frac{\kappa_n}{2m_n}\partial_\nu(\bar{n}\sigma^{\mu\nu}n)X_\mu\ , \tag{3.72}$$

$$\mathcal{L}_{S^\pi=1^+} = a_p \bar{p}\gamma^\mu\gamma^5 p X_\mu + a_n \bar{n}\gamma^\mu\gamma^5 n X_\mu\ , \tag{3.73}$$

see App. B. Although the pure scalar hypothesis is not able to explain the anomaly observed in the ^{8}Be decay, we'll present for completeness explicit expressions also in this case, since it can anyway affect the ^{4}He and ^{12}C decays, see Tab. 3.5 and it can be relevant in the mixed parity hypothesis. The effective matching between these effective interactions and the UV interactions of the X boson with quark and gluons are reported in App. B. Once the X boson is produced from the nuclear collision, it decays to an e^+e^- pair with a branching ratio which depends on the size of the X coupling to electrons.

3.5.1 Spherical operators

In the non relativistic and long wavelength approximation the spherical operators with $J = 0, 1$ for the various S^π assignment for the X boson are given by

Scalar case $S^\pi = 0^+$

For the $J = 0$ term we go here beyond the leading order in the long wavelength and non relativistic expansion since leading order term proportional to the identity gives an identically vanishing

[5] Effective nucleon operators are in principle also function of form factors $F(q^2)$. In all practical cases however the transferred momentum is much smaller than the hadron scale Λ_{QCD}, so that we approximate the form factors as constants.

[6] We neglect electric dipole moment (EDM) operators since, by naive counting analysis, they would contribute at a higher order than the axial current $\bar{\psi}\gamma^\mu\gamma^5\psi$. Moreover, they can only be generated by EDM effective quark operators, so that they will generally be suppressed by loop effects.

contribution. One has[7]

$$\mathcal{G}_{00} \simeq \frac{1}{\sqrt{4\pi}} \sum_{s=1}^{A} z_s \left[1 - \frac{p_s^2}{2m_{\mathcal{N}}^2} - \frac{k^2 r_s^2}{6} \right], \tag{3.74}$$

$$\mathcal{G}_{1M} \simeq \frac{k}{3} \sqrt{\frac{3}{4\pi}} \sum_{s=1}^{A} z_s \vec{r}_s \cdot \hat{e}_M, \tag{3.75}$$

where $z_s = z_p$ ($z_s = z_p$) if the s-th nucleon is a proton (neutron). A similar notation is adopted for the rest of the section.

Pseudoscalar case $S^\pi = 0^-$

For the pseudoscalar case the relevant spherical operators are

$$\mathcal{G}_{00} \simeq \frac{k^2}{6m_{\mathcal{N}}} \frac{1}{\sqrt{4\pi}} \sum_{s=1}^{A} h_s (\vec{r}_s \cdot \vec{\sigma}_s) \equiv \frac{k^2}{12m_{\mathcal{N}}} \frac{1}{\sqrt{4\pi}} [(h_p + h_n)\hat{d}_0^\sigma + (h_p - h_n)\hat{d}_3^\sigma] \ , \tag{3.76}$$

$$\mathcal{G}_{1M} \simeq -\frac{k}{6m_{\mathcal{N}}} \sqrt{\frac{3}{4\pi}} \sum_{s=1}^{A} h_s \vec{\sigma}_s \cdot \hat{e}_M \equiv -\frac{k}{6m_{\mathcal{N}}} \sqrt{\frac{3}{4\pi}} [h_p \hat{\sigma}_M^{(p)} + h_n \hat{\sigma}_M^{(n)}] \ , \tag{3.77}$$

where for $\mathcal{G}_{00}$ we have split the expression among the isoscalar and isovector contributions.

Vector case $S^\pi = 1^-$

In this case conservation of the vector current implies a relation between the operator $\mathcal{L}_{JM}$ and $\mathcal{M}_{JM}$, *c.f.r.* Eq. (3.21), and one has

$$\mathcal{M}_{00} \simeq -\frac{k^2}{6} \frac{1}{\sqrt{4\pi}} \sum_{s=1}^{A} C_s r_s^2 \equiv -\frac{ek^2}{6} \rho^{(X)} \ , \tag{3.78}$$

$$\mathcal{M}_{1M} \simeq \frac{k}{3} \sqrt{\frac{3}{4\pi}} \sum_{s=1}^{A} C_s \vec{r}_s \cdot \hat{e}_M \equiv \frac{ek}{3} d_M^{(X)} \ , \tag{3.79}$$

$$\mathcal{T}_{1\mathrm{M}}^{el} \simeq \frac{\sqrt{2}\omega}{3} \sqrt{\frac{3}{4\pi}} \sum_{s=1}^{A} C_s \vec{r}_s \cdot \hat{e}_M \equiv \frac{\sqrt{2}e\omega}{3} d_M^{(X)} \ , \tag{3.80}$$

$$\mathcal{T}_{1M}^{\mathrm{mag}} \simeq \frac{i\sqrt{2}k}{3} \frac{1}{2m_{\mathcal{N}}} \sqrt{\frac{3}{4\pi}} \sum_{s=1}^{A} [C_s (\vec{r}_s \times \vec{p}_s) + (C_s + \kappa_s)\vec{\sigma}_s] \cdot \hat{e}_M \equiv \frac{i\sqrt{2}k\mu_{\mathcal{N}}}{3} \mu_M^{(X)} \ . \tag{3.81}$$

[7] $\hat{e}_M = \sqrt{4\pi} Y_{1M}(\frac{\vec{r}}{r})$.

	^{8}**Be**	^{4}**He**	^{12}**C**
0^+	/	^{4}**He(20.21)** $2k(z_p+z_n)^2\left\lvert\frac{k^2}{6e}\langle\rho^{(\gamma)}\rangle+\frac{1}{2m_{\mathcal{N}}}\langle\hat{K}\rangle\right\rvert^2$	$\frac{2k^3}{27}(z_p-z_n)^2\lvert\langle\lvert\lvert d^{(\gamma)}\rvert\rvert\rangle\rvert^2$
0^-	$\frac{k^3}{72\pi m_N^2}\lvert\langle h_p\hat{\sigma}^{(p)}+h_n\hat{\sigma}^{(n)}\rangle\rvert^2$	^{4}**He(21.01)** $\frac{k^5}{228\pi m_N^2}(h_p+h_n)^2\lvert\langle\hat{d}_0^\sigma\rangle\rvert^2$	/
1^-	$\frac{4\mu_{\mathcal{N}}^2k^3}{27}\lvert\langle\mu^{(X)}\rangle\rvert^2$	^{4}**He(20.21)** $\frac{m^2k^3\alpha}{18}\lvert\langle\rho^{(X)}\rangle\rvert^2$	$\frac{16\pi\alpha k\omega^2}{27}\left(1+\frac{m^2}{2\omega^2}\right)\lvert\langle d^{(X)}\rangle\rvert^2$
1^+	$\frac{k}{18\pi}\left(2+\frac{\omega^2}{m^2}\right)\lvert\langle a_p\hat{\sigma}^{(p)}+a_n\hat{\sigma}^{(n)}\rangle\rvert^2$	^{4}**He(21.01)** $\frac{\omega^2k^3}{72\pi m^2}(a_p+a_n)^2\lvert\langle\hat{d}_0^\sigma\rangle\rvert^2$	$\frac{k^3}{144\pi}(a_p-a_n)^2\lvert\langle\hat{D}_3^\sigma\rangle\rvert^2$

Table 3.7: Decay rates for the ^{8}Be, ^{4}He and ^{12}C nuclear processes for the various spin assignment of the X boson. In the case of the Helium transition for each spin-parity possibility we indicate the ^{4}He excited state involved. In the expressions $\langle\mathcal{O}\rangle$ represents the matrix element between the ground state and the excited nucleus of the corresponding operator, *e.g.* for the ^{12}C transition in the 0^+ case $\langle||d^{(\gamma)}||\rangle=\langle^{12}\mathrm{C}||d^{(\gamma)}||^{12}\mathrm{C}(17.23)\rangle$. For the ^{4}He and ^{12}C cases we only report the non vanishing isoscalar and isovector contributions respectively.

Axial vector case $S^\pi=1^+$

Finally the spherical operators for the axial vector case read

$$\mathcal{M}_{00}\simeq\mathcal{M}_{1M}\simeq 0\,, \tag{3.82}$$

$$\mathcal{L}_{00}\simeq-\frac{ik}{3}\frac{1}{\sqrt{4\pi}}\sum_{s=1}^{A}a_s(\vec{r}_s\cdot\vec{\sigma}_s)\equiv-\frac{ik}{6}\frac{1}{\sqrt{4\pi}}[(a_p+a_n)\hat{d}_0^\sigma+(a_p-a_n)\hat{d}_3^\sigma]\,, \tag{3.83}$$

$$\mathcal{L}_{1M}\simeq\frac{i}{3}\sqrt{\frac{3}{4\pi}}\sum_{s=1}^{A}a_s\vec{\sigma}_s\cdot\hat{e}_M\equiv\frac{i}{3}\sqrt{\frac{3}{4\pi}}[a_p\hat{\sigma}_M^{(p)}+a_n\hat{\sigma}_M^{(n)}]\,, \tag{3.84}$$

$$\mathcal{T}_{1M}^{\mathrm{el}}\simeq\frac{i\sqrt{2}}{3}\sqrt{\frac{3}{4\pi}}\sum_{s=1}^{A}a_s\vec{\sigma}_s\cdot\hat{e}_M\equiv\frac{i\sqrt{2}}{3}\sqrt{\frac{3}{4\pi}}[a_p\hat{\sigma}_M^{(p)}+a_n\hat{\sigma}_M^{(n)}]\,, \tag{3.85}$$

$$\mathcal{T}_{1M}^{\mathrm{mag}}\simeq\frac{ik}{3\sqrt{2}}\sqrt{\frac{3}{4\pi}}\sum_{s=1}^{A}a_s(\vec{r}_s\times\vec{\sigma}_s)\cdot\hat{e}_M\equiv\frac{ik}{6\sqrt{2}}\sqrt{\frac{3}{4\pi}}[(a_p+a_n)\hat{D}_{0M}^\sigma+(a_p-a_n)\hat{D}_{3M}^\sigma]\,. \tag{3.86}$$

3.5.2 Decay rates

We can now express the decay rates for the various spin-parity assignment of the X boson in the case of the ^{8}Be, ^{4}He and ^{12}C transitions. We report them Tab. 3.7, expressed in function of nuclear matrix element of the relevant operators involved in the transition. Symmetry consideration allow to express these matrix elements in function of known ones. We list here the relevant relations

Beryllium matrix elements

Assuming the static quark model $\kappa_p\simeq-\kappa_n\simeq2(C_p-C_n)$, see App. B for the details. From isospin symmetry then one has

$$\langle^8\mathrm{Be}||\mu^{(X)}||^8\mathrm{Be}(17.64)\rangle=\alpha_1\left(\frac{C_p+C_n}{e}\right)M1_{I=0}^\gamma+(\beta_1+\alpha_1\xi)\left(\frac{C_p-C_n}{e}\right)M1_{I=1}^\gamma\,, \tag{3.87}$$

$$\langle^8\mathrm{Be}||\mu^{(X)}||^8\mathrm{Be}(18.15)\rangle=(-\alpha_1+\beta_1\xi)\left(\frac{C_p-C_n}{e}\right)M1_{I=1}^\gamma+\beta_1\left(\frac{C_p+C_n}{e}\right)M1_{I=0}^\gamma\,, \tag{3.88}$$

where the corresponding values are reported in App. 3.4.3, while we take from [225]

$$\begin{aligned}
&\langle \mathrm{Be}||\hat{\sigma}^{(p)}||^8\mathrm{Be}(18.15)\rangle = -0.047(29)\ , \qquad &&\langle \mathrm{Be}||\hat{\sigma}^{(n)}||^8\mathrm{Be}(18.15)\rangle = -0.132(33)\ , \\
&\langle \mathrm{Be}||\hat{\sigma}^{(p)}||^8\mathrm{Be}(17.64)\rangle = 0.102(28)\ , \qquad &&\langle \mathrm{Be}||\hat{\sigma}^{(n)}||^8\mathrm{Be}(17.64)\rangle = -0.073(29)\ .
\end{aligned} \tag{3.89}$$

Helium matrix elements

Isospin symmetry allows to relate

$$\langle {}^4\mathrm{He}||\rho^{(X)}||{}^4\mathrm{He}(20.21)\rangle = \left(\frac{C_p + C_n}{e}\right) \langle {}^4\mathrm{He}||\rho^{(\gamma)}||{}^4\mathrm{He}(20.21)\rangle\ , \tag{3.90}$$

where again the electromagnetic matrix element is reported in App. 3.4.3 while we take from [238]

$$|\,\langle {}^4\mathrm{He}||\hat{d}_0^\sigma||{}^4\mathrm{He}(21.01)\rangle\,|^2 \simeq 15.5\,\mathrm{fm}^2 \simeq 4\times 10^{-4}\,\mathrm{MeV}^{-2} \tag{3.91}$$

but no uncertainty has been given. We will arbitrarily assume a 10% error on the matrix element in our calculation. Finally, to the best of our knowledge, the matrix element of the operator $\hat{K} = \sum_s p_s^2/2m_s$ has never been evaluated so far.

Carbon matrix elements

Isospin symmetry allows to relate

$$\langle {}^{12}\mathrm{C}||d^{(X)}||{}^{12}\mathrm{C}(17.23)\rangle = \left(\frac{C_p - C_n}{e}\right) \langle {}^{12}\mathrm{C}||d^{(\gamma)}||{}^{12}\mathrm{C}(17.23)\rangle\ , \tag{3.92}$$

whose values is reported in App. 3.4.3, while the axial matrix element $\hat{D}_3^\sigma$ has not been evaluated, to the best of our knowledge.

3.6 Experimental constraints on a spin-1 boson

A light boson coupled to first generation quarks and leptons is subject to a large variety of experimental constraints. In this section we recap the most relevant ones that affects a possible explanation of the ATOMKI anomaly through a BSM degree of freedom with mass ~ 17 MeV for the spin-1 case. We parametrize the effective UV interactions of a spin-1 state X_μ with leptons and quarks as

$$\mathcal{L} = X_\mu \sum_{f=q,l\ldots} \bar{\psi}^f (C_V^f + \gamma^5 C_A^f)\psi^f = X_\mu \sum_{f=q,l\ldots} \left(C_{L,R}^f \bar{\psi}_{L,R}^f \gamma^\mu \psi_{L,R}^f\right)\ , \tag{3.93}$$

where $C_{V,A}^f = \frac{1}{2}(C_R^f \pm C_L^f)$ and we assume diagonal couplings in flavor space. The connection between the quark and nucleon couplings can be found in App. B. We list in the following the most relevant constraints for the spin-1 case coupling to the first generation of quarks and leptons.

3.6.1 $e^+e^- \to \gamma X$ scattering

By neglecting kinematic differences with respect to the pure dark photon case, we can recast the bound from the KLOE experiment at the DAΦNE collider [239] from which we obtain a bound

$$\sqrt{(C_V^e)^2 + (C_A^e)^2} \lesssim \frac{6.1\times 10^{-4}}{\sqrt{\mathrm{BR}(X\to e^+e^-)}}\ . \tag{3.94}$$

3.6.2 Parity violation

Parity violation in Møller scattering constraints the product of the vector and axial couplings. The most sensitive measurement arises from SLAC E158 [240] at $Q^2 = 160$ MeV^2. The measurement in [240] has been recast in [241] and the obtained bound reads

$$|C_V^e \times C_A^e| \lesssim 10^{-8} \ . \tag{3.95}$$

3.6.3 Beam dump experiments

Beam dump experiments look for X production via bremsstrahlung from electrons scattering off target nuclei. For the X particle not to be seen in these experiments there are two possibilities: either the particle is not produced at all, or its decay products are caught in the dump, thus setting both an upper and lower limit for the couplings of the X boson. In the first case the stronger limit comes from the E137 experiment [242], see also [243], which is independent on the X decay rate and gives

$$\sqrt{(C_V^e)^2 + (C_A^e)^2} \lesssim 1.1 \times 10^{-8} \ , \tag{3.96}$$

while in the second case the stronger limit comes from the NA64 experiment [244, 245] for which we have

$$\sqrt{(C_V^e)^2 + (C_A^e)^2} \gtrsim 3.6 \times 10^{-5} \times \sqrt{\mathrm{BR}(X \to e^+e^-)} \ . \tag{3.97}$$

3.6.4 Prompt decay in ATOMKI detector

The requirement of a prompt decay into the ATOMKI detector imposes now the constraint

$$\sqrt{(C_V^e)^2 + (C_A^e)^2} \gtrsim 3 \times 10^{-7} \times \sqrt{\mathrm{BR}(X \to e^+e^-)} \ , \tag{3.98}$$

which is weaker than the bound from NA64.

3.6.5 Atomic parity violation

In atomic system, parity violation can be observed in the case, *e.g*, of and electric dipole transition between two atomic states with the same parity. The X_μ gives additional contributions to these transitions due to the interaction between atomic electrons and the nucleus. In the effective operator

$$\mathcal{L} \supset -\frac{1}{m_X^2}\left[C_V^u C_A^e (\bar{u}\gamma^\mu u)(\bar{e}\gamma_\mu\gamma^5 e) + C_A^u C_V^e (\bar{u}\gamma^\mu\gamma^5 u)(\bar{e}\gamma_\mu e) + u \leftrightarrow d\right] \ , \tag{3.99}$$

where only the $V \times A$ part have been kept, only the $A_e \times V_{u,d}$ interaction give a relevant effect for parity violation observables. This is due to the fact this part of the interaction between the electron and the nucleus is coherent, and thus proportional to the total weak charge of the nucleus itself, while the $A_q \times V_e$ interaction adds incoherently. This effect is thus suppressed for heavy enough nuclei [246]. The BSM contribution to $A_e \times V_{u,d}$ can be expressed as a modification to the weak nuclear charge Q_W [247]

$$\delta Q_W = -\frac{2\sqrt{2}}{G_F} 3(Z+N)\frac{C_A^e C_V^{q,\mathrm{eff}}}{m_X^2} \ , \qquad C_V^{q,\mathrm{eff}} = \frac{C_V^u(2Z+N) + C_V^d(Z+2N)}{3(Z+N)} \ . \tag{3.100}$$

The most accurate prediction comes from transition of $^{133}_{55}$Cs [248] which, combined with the SM theoretical prediction [249], yields [250] $|\delta Q_W| \lesssim 0.6$ hence the bound reads

$$|C_A^e| \left|\frac{188}{399} C_V^u + \frac{211}{399} C_V^d\right| \lesssim 1.8 \times 10^{-12} \ . \tag{3.101}$$

3.7 Results

We present in this section our main results, deriving the possible range of the nucleon couplings to the X particle that can explain both the ^{8}Be and ^{4}He anomalies, further commenting on the possibility of simultaneously explain the ^{12}C one. We analyze all the scenarios where the X boson has a definite parity, which implies that the pure scalar boson case is ruled out since it cannot explain the ^{8}Be anomaly. The best fit value for the anomalous decay rate for the ^{8}Be transition is [197]

$$\frac{\Gamma(^8\text{Be}(18.15) \to {}^8\text{Be} + X)}{\Gamma(^8\text{Be}(18.15) \to {}^8\text{Be} + \gamma)} \, \text{BR}(X \to e^+e^-) = (6 \pm 1) \times 10^{-6}. \tag{3.102}$$

The ATOMKI collaboration observed no anomalous signal in the ^{8}Be(17.64) transition in the first experiment [22] but later they reported a non vanishing best fit for this anomalous decay rate in a contribution to the proceedings of *International Symposium Advances in Dark Matter and Particle Physics 2016* [251]. In the following we will consider only the ^{8}Be(18.15) anomalous decay and we present the results with both the ^{8}Be transitions in App. C. For the case of the ^{4}He transition the total cross section is given by the sum of the two states populated in the experiment

$$\frac{\sigma_X}{\sigma_{E0}} = \frac{\Gamma(^4\text{He}(20.21) \to {}^4\text{He} + X)}{\Gamma(^4\text{He}(20.21) \to {}^4\text{He} + e^+e^-)} + \frac{\sigma_-\Gamma_+}{\sigma_+\Gamma_-} \frac{\Gamma(^4\text{He}(21.01) \to {}^4\text{He} + X)}{\Gamma(^4\text{He}(20.21) \to {}^4\text{He} + e^+e^-)} \, , \tag{3.103}$$

where $\Gamma_\pm$ is the total width of the $0^\pm$ excited state of Helium nucleus and

$$\sigma_+ = \sigma(p + {}^3\text{H} \to {}^4\text{He}(20.21)), \qquad \sigma_- = \sigma(p + {}^3\text{H} \to {}^4\text{He}(21.01)) \, . \tag{3.104}$$

The ratio σ_-/σ_+ can be evaluate by the relation of Eq. (D.6) in App. D in the narrow width approximation. The ATOMKI collaboration reported $\sigma_X = 0.2 \, \sigma_{E0}$ [8], while no uncertainty is associated with this measurement. We then arbitrarily associate a relative error to the Helium best fit equal to the one from Beryllium measurement of Eq. (3.102). Different spin parity assignments contribute to the rates of the two ^{4}He excited states, see Tab. 3.5. If the X boson is a vector or a scalar state one has

$$\frac{\Gamma(^4\text{He}(20.21) \to {}^4\text{He} + X)}{\Gamma(^4\text{He}(20.21) \to {}^4\text{He} + e^+e^-)} \, \text{BR}(X \to e^+e^-) = 0.20 \pm 0.03 \, , \tag{3.105}$$

while if it's a pseudoscalar or an axial vector the best fit is

$$\frac{\Gamma(^4\text{He}(21.01) \to {}^4\text{He} + X)}{\Gamma(^4\text{He}(20.21) \to {}^4\text{He} + e^+e^-)} \, \text{BR}(X \to e^+e^-) = 0.87 \pm 0.14 \, , \tag{3.106}$$

with $\Gamma(^4\text{He}(20.21) \to {}^4\text{He} + e^+e^-) = (3.3 \pm 1.0) \times 10^{-4}$ eV [202]. For the case of the ^{12}C transition the recent results [24] find the derived branching ratio for X emission with respect to the γ one to be $\sim 3.6(3) \times 10^{-6}$, *i.e.*

$$\frac{\Gamma(^{12}\text{C}(17.23) \to {}^{12}\text{C} + X)}{\Gamma(^{12}\text{C}(17.23) \to {}^{12}\text{C} + \gamma)} \, \text{BR}(X \to e^+e^-) = 3.6(3) \times 10^{-6}. \tag{3.107}$$

We now present our findings for the regions in the effective nucleon couplings parameter space for the various spin-parity assignments for the X boson. In presenting our results we assume, for simplicity, $\text{BR}(X \to e^+e^-) = 1$. For different BR assumptions the derived allowed space in the nucleon effective couplings will be rescaled according to Eq. (3.102), Eq. (3.105) and Eq. (3.106). We stress that our analysis relies on various assumptions, as the hypothesis of narrow width approximation for the nuclear production of the excited states. Other potential contribution, as for example direct capture processes, could potentially change the conclusions of our analysis.

[8] Differently from this work, the Authors of [221] took as experimental input the ratio of decay rates calculated in the experimental paper [23].

3.7.1 Pseudoscalar and mixed parity scenario

We summarize the results for the pure pseudoscalar scenario in Fig. 3.6, where the shaded blue and orange areas represent the 1σ and 2σ compatibility regions with the ATOMKI ^{8}Be and ^{4}He anomalies respectively. We also overlay in red the region of parameter space satisfying the SINDRUM bound from $\pi^+ \to e^+\nu_e X$ decay [230, 252]. This is given in term of the pseudoscalar-pion mixing angle, linked to the isovector nucleon coupling as

$$\theta_{X\pi} = \frac{f_\pi (h_p - h_n)}{2 g_A m_{p,n}} \,, \tag{3.108}$$

where $g_A \sim 1.27$ is axial nucleon factor and $f_\pi \sim 93$ MeV is the pion decay constant, and reads

$$|\theta_{X\pi}| \lesssim \frac{10^{-4}}{\sqrt{\mathrm{BR}(X \to e^+e^-)}} \,. \tag{3.109}$$

All together we see that the ^{8}Be and ^{4}He anomalies can be simultaneously satisfied for a range of effective nuclear coupling $h_{n,p}$ of $\mathcal{O}(10^{-2})$. However, the recent observation of an anomalous signal in the ^{12}C transition would, if confirmed, exclude by itself the pure pseudoscalar scenario, see again Tab. 3.5. It's then interesting to entertain the possibility that the scalar X boson has both scalar and pseudoscalar couplings. As already mentioned, because of parity conservation the scalar contribution to the ^{8}Be transitions vanishes, so the latter processes only set a constraint on the range of the pseudoscalar couplings, which as we have shown in Fig. 3.6 are required to be of order of $\mathcal{O}(10^{-2})$. On the other side the ^{4}He decays acquire a contribution from both the spin-parity state, although related to different nuclear resonances, see Tab. 3.5. As discussed in Sec. 3.5.2 the value of the matrix element $\langle {}^4\mathrm{He}||\hat{K}||{}^4\mathrm{He}(20.21)\rangle$ is unknown. By neglecting its contribution one finds that the pure scalar contribution is dominant over the pseudoscalar one with a similar value for nucleon couplings $z_{p,n}$ $h_{p,n} \simeq 10^{-2}$, *i.e.*

$$\Gamma({}^4\mathrm{He}(20.21) \to {}^4\mathrm{He} + X) \simeq\ 6 \times 10^{-4}\mathrm{eV} \left(\frac{z_p + z_n}{10^{-2}}\right)^2 \,, \tag{3.110}$$

$$\Gamma({}^4\mathrm{He}(21.01) \to {}^4\mathrm{He} + X) \simeq\ 9.7 \times 10^{-6}\mathrm{eV} \left(\frac{h_p + h_n}{10^{-2}}\right)^2 \,, \tag{3.111}$$

so that the theoretical predictions for the ^{4}He transition is too large to match the ATOMKI results. We expect that this assertion holds even once $\langle {}^4\mathrm{He}||\hat{K}||{}^4\mathrm{He}(20.21)\rangle$ is also included. Hence, one is forced to conclude that the scalar isoscalar coupling $z_p + z_n$ is suppressed, at least respect the pseudoscalar one, leaving us with almost the same configurations as the pure pseudoscalar one of Fig. 3.6. This conclusion is in agreement with earlier results [221]. On the other side for the ^{12}C transition, the scalar isovector coupling would give

$$\frac{\Gamma({}^{12}\mathrm{C}(17.23) \to {}^{12}\mathrm{C} + X)}{\Gamma({}^{12}\mathrm{C}(17.23) \to {}^{12}\mathrm{C} + \gamma)} \simeq 2.4 \times 10^{-6} \left(\frac{z_p - z_n}{10^{-2}}\right)^2 \,, \tag{3.112}$$

in agreement with the order of magnitude of the ATOMKI fit (3.107) if $z_p - z_n \simeq h_{p,n} \simeq \mathcal{O}(10^{-2})$ and all the three anomalous measurements can be simultaneously satisfied.

3.7.2 Vector and axial vector scenarios

We summarize the results for the spin-1 cases in Fig. 3.7, with the same color code as Fig. 3.6 for the regions satisfying the ATOMKI anomalies. In the upper panels we show the results for the

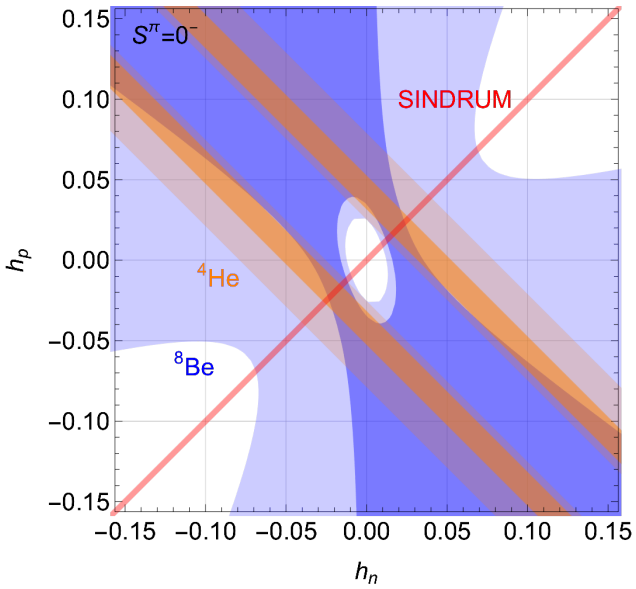

Figure 3.6: Regions of the $h_{n,p}$ effective nuclear couplings of a pure pseudoscalar states where the ^{8}Be (blue) and ^{4}He (orange) anomalous ATOMKI transition can be explained at 1σ or 2σ. Inside the red region the SINDRUM bound is satisfied.

$S^\pi = 1^-$ assignment for the X boson. Here in the left and right plot we assume $\xi = 0$ and $\xi = 0.549$ respectively, where ξ represents non perturbative contribution to isospin breaking effects in the ^{8}Be case, see [220] and App. 3.4.3 for details. For the vector case the strongest bound comes from the non observation from the NA48 experiment of the $\pi^0 \to \gamma X$ decay in dark photon searches [253]. This process receives two different contributions. One from the axial anomaly and a non anomalous one. The non anomalous contributions is proportional to the small quark masses [254, 255] and can be neglected, while the anomalous one is proportional to the anomaly trace factor. One gets the bound

$$|C_p| \times \sqrt{\mathrm{BR}(X \to e^+e^-)} \lesssim 2.5 \times 10^{-4} \,, \tag{3.113}$$

which implies a *protophobic* nature for the X boson. We show in Fig. 3.7 in red the region of parameter space where the *protophobia* constraint is satisfied. Another relevant bound comes from observations of the angular dependence of neutron-lead scattering. The exchange of new, weakly-coupled boson produces a Yukawa potential[9] acting on the neutron, whose contribution has been constrained for the ^{208}Pb-n scattering as [256]

$$|C_n| \left| \frac{126}{208} C_n + \frac{82}{208} C_p \right| \lesssim 3.6 \times 10^{-5} \,. \tag{3.114}$$

We show in Fig. 3.7 in gray the region of parameter space where the ^{208}Pb-n scattering constraint is satisfied. As it can be seen for the $\xi = 0.549$ assignment, a combined explanation of the ^{8}Be, blue region, and ^{4}He, orange region, anomalies at 1σ is in tension with the NA48 constraint, while it is possible at the 2σ level. Regarding the ^{12}C ATOMKI anomaly in the case of a $S^\pi = 1^-$ state the

[9] The non-relativistic limit of the vector bilinears is spin independent, see Tab. 3.6, so the nucleon contributions of a nuclear state are added coherently, while they are spin dependent and are added incoherently for the axial and pseudoscalar cases. We then expect negligible contributions for the $S^\pi = 0^-, 1^+$ cases, especially when considering a nucleus with null spin like ^{208}Pb.

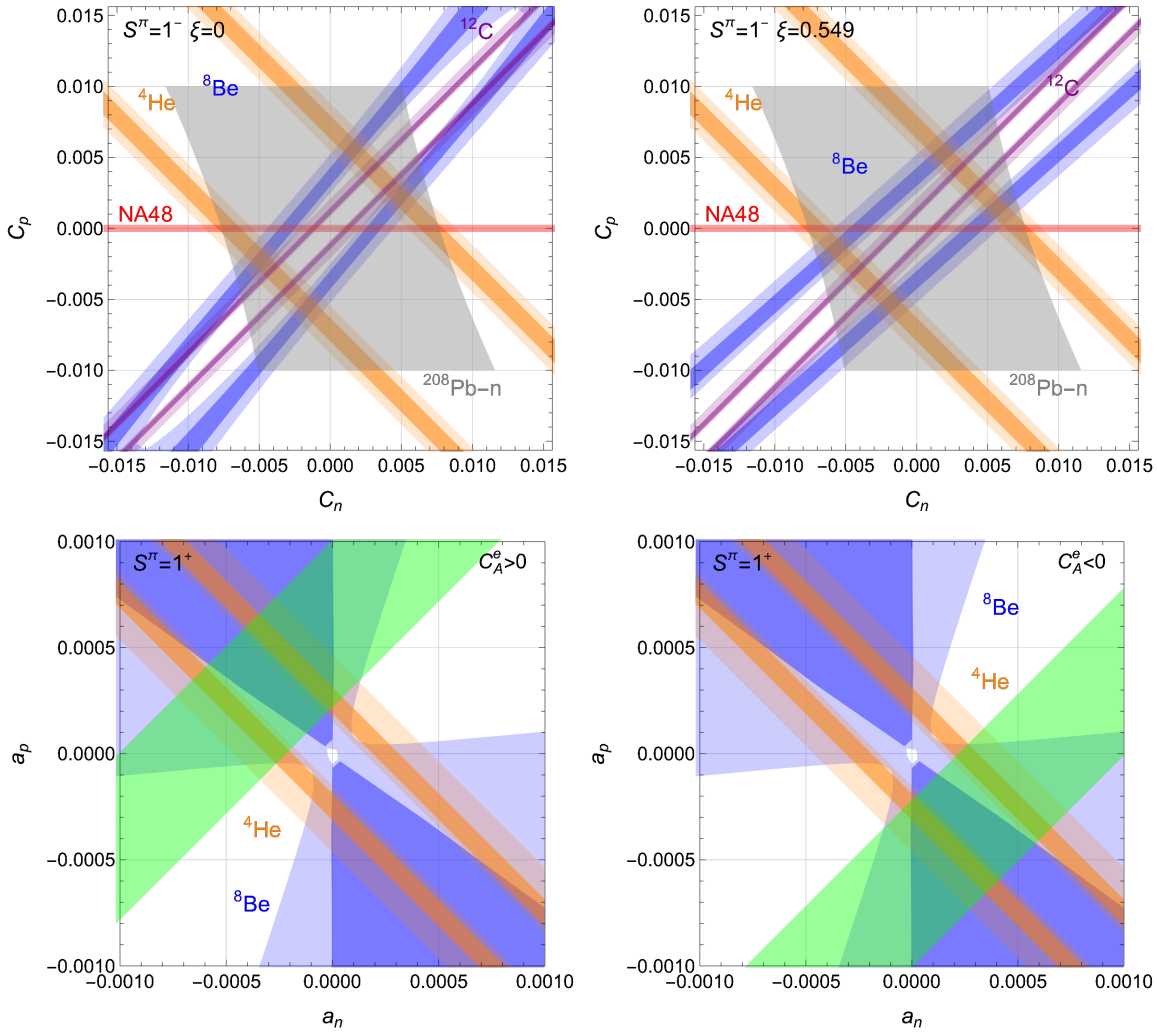

Figure 3.7: *Upper panels:* Regions of the $C_{n,p}$ effective nuclear couplings of a pure vector state where the ^{8}Be (blue), ^{4}He (orange) and ^{12}C (purple) anomalous ATOMKI transition can be explained at 1σ or 2σ. Inside the red and the gray region, respectively, the NA48 and the ^{208}Pb-n scattering bound are satisfied. In the left and right panel we assume $\xi = 0$ and $\xi = 0.549$ respectively, see App. 3.4.3 for details. *Lower panels:* Regions of the $a_{n,p}$ effective nuclear couplings of a pure axial vector state where the ^{8}Be (blue) and ^{4}He (orange) anomalous ATOMKI transition can be explained at 1σ or 2σ. In the green region the KTeV anomaly in $\pi \to e^+e^-$ decay can be satisfied, by assuming a positive (left panel) and negative (right panel) value for the C_A^e axial coupling of the X boson to electrons that can explain the anomalous $(g-2)_e$, see main text for more details.

relevant matrix element is known. In this case one then gets

$$\frac{\Gamma(^{12}\mathrm{C}(17.23) \to {}^{12}\mathrm{C} + X)}{\Gamma(^{12}\mathrm{C}(17.23) \to {}^{12}\mathrm{C} + \gamma)} \simeq 2.64 \times 10^{-6} \left(\frac{C_p - C_n}{10^{-3}}\right)^2 , \tag{3.115}$$

in agreement with the order of magnitude of the ATOMKI fit (3.107) if $C_p - C_n \simeq \mathcal{O}(10^{-3})$. The 1σ and 2σ bands related to the ^{12}C transition are shown in purple in the upper panels of Fig. 3.7.

Note that, if confirmed, the ^{12}C ATOMKI anomaly is in tension with a combined explanation of the ^{8}Be and ^{4}He anomalies and the *protophobia* constraint. In addition, a recent work [257] pointed out that the SINDRUM bound for a vector spin-1 X would be so strong that if combined with our results, it exclude the vector explanation.

On the other side an axial vector $S^\pi = 1^+$ state can explain both the ^{8}Be and ^{4}He ATOMKI anomalies, as shown in the lower panels of Fig. 3.7, with axial couplings to the nucleon of $\mathcal{O}(10^{-4})$. Within the green shaded area the KTeV anomaly in $\pi^0 \to e^+e^-$ decay can be explained for positive and negative values for the axial X coupling to electrons C_A^e, see Sec. 3.7.2 for details. If one includes the SINDRUM bound for a axial spin-1 X as done by [257], the axial solution still works but with a smaller allowed region. As regarding the possibility of also explaining the ^{12}C ATOMKI anomaly the relevant nuclear matrix element, see Tab. 3.7, is currently unknown. While no definite claim can be made until it becomes available, we can make an order of magnitude estimate on the size of the $\hat{D}_3^\sigma$ and speculate on the possibility of a combined explanation of all the three ATOMKI anomalies with an axial vector state. We can expect that the isovector spin dipole would be of the order of the nuclear radius times the number of nucleons inside the nucleus. We can then estimate

$$\langle {}^{12}\mathrm{C}||\hat{D}_3^\sigma||{}^{12}\mathrm{C}(17.23)\rangle \simeq A \times R \simeq 12 \times 2.75\,\mathrm{fm} \simeq 1.7 \times 10^{-1}\,\mathrm{MeV}^{-1}. \tag{3.116}$$

For a range of nucleon parameters $a_{p,n} \simeq \mathcal{O}(10^{-4})$, as suggested by Fig. 3.7, one get an estimate for the anomalous ^{12}C transition mediated by an axial X boson of

$$\frac{\Gamma({}^{12}\mathrm{C}(17.23) \to {}^{12}\mathrm{C} + X)}{\Gamma({}^{12}\mathrm{C}(17.23) \to {}^{12}\mathrm{C} + \gamma)} \simeq \mathcal{O}(10^{-6})\ , \tag{3.117}$$

which is in order of magnitude accord with the ATOMKI result which predicts a value of $3.6(3) \times 10^{-6}$ for this rate [24]. We stress again that this conclusion strongly depends on our order of magnitude estimate of the $\hat{D}_3^\sigma$ matrix element, which seems to indicate that an axial vector state might be favored for a combined explanation. However to properly test its consistency with the ^{12}C anomalous transition, the relevant matrix element must be properly computed. Until then no definite conclusions can be drawn. In a general scenario where both vector and axial couplings to nucleons are present, the decay width for the real X emission is the direct sum of the two contributions. Assuming vector and axial couplings of the same order of magnitude, the axial contribution would typically dominate over the vector one.

Intriguingly, for the case a pure axial boson $S^\pi = 1^+$, in the parameter space where the ^{4}He and ^{8}Be anomalies can be explained, other experimental anomalies can be simultaneously satisfied, while being compatible with current constraints on the electron couplings of the X boson. This is the case of the KTeV anomaly in $\pi^0 \to e^+e^-$ decay [258], inside the green region in Fig. 3.7, and the anomalous magnetic moment of the electron $(g-2)_e$, as we will explain in the following.

KTeV anomaly and anomalous $(g-2)_e$

The lowest SM contribution to this decay is a one loop process with two photons as intermediate states. The KTeV-E779 Collaboration reports the measured value [259]

$$\mathrm{BR}(\pi^0 \to e^+e^-)_{\mathrm{exp}} = (7.48 \pm 0.29 \pm 0.25) \times 10^{-8}, \tag{3.118}$$

where they extrapolated from a selected kinematic region to the entire one. The most recent calculation of SM prediction is [260]

$$\mathrm{BR}(\pi^0 \to e^+e^-)_{\mathrm{SM}} = (6.25 \pm 0.03) \times 10^{-8}. \tag{3.119}$$

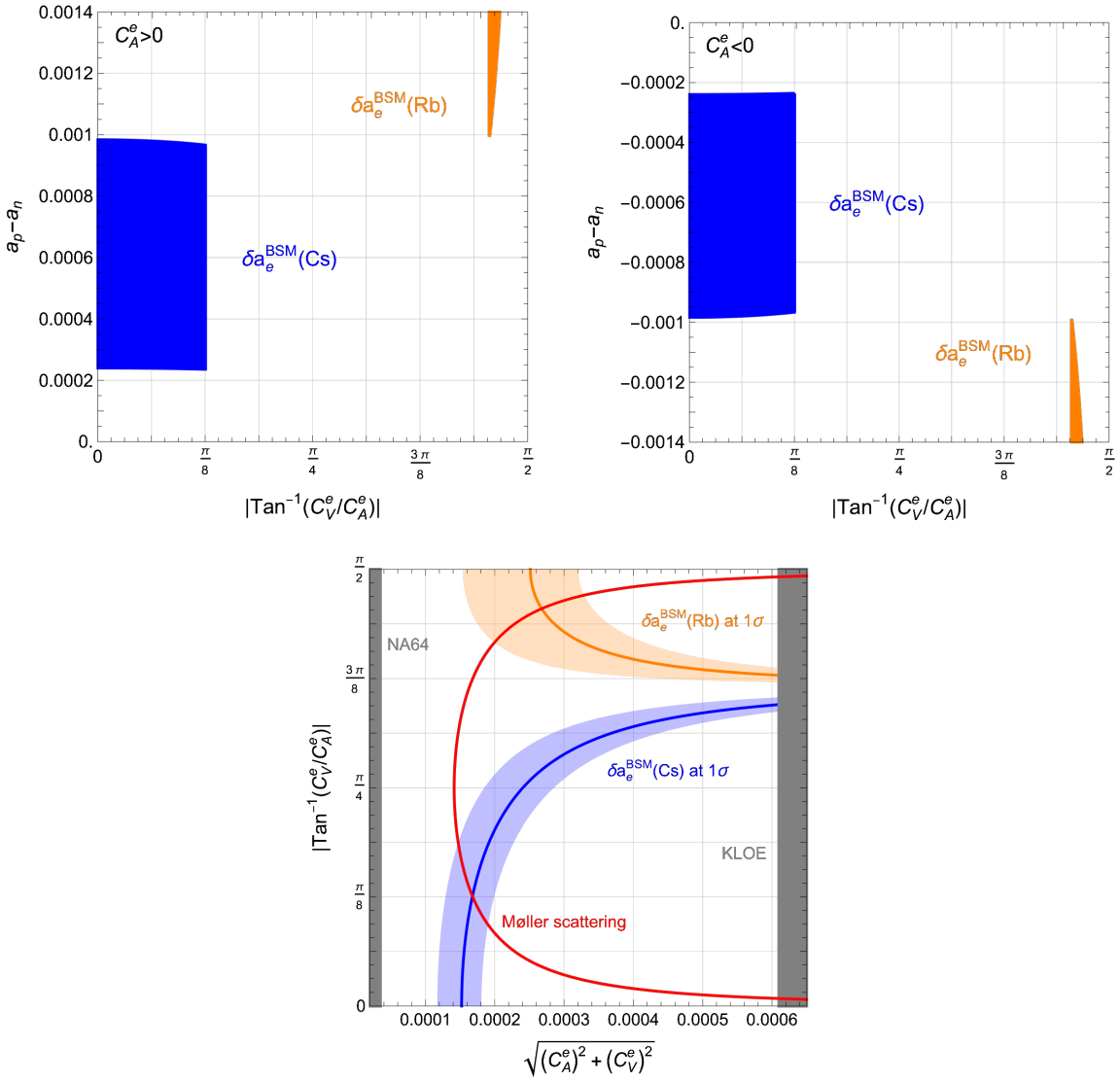

Figure 3.8: *Upper panels:* Values of the isovector nucleon axial coupling $a_p - a_n$ able to explain the KTeV anomaly at 1σ varying the ratio of vector and axial electron coupling for the two distinct cases $C_A^e > 0$ and $C_A^e < 0$. *Lower panel:* Bounds on the vector and axial couplings of the electron to a spin-1 boson with mass $m_X \sim 17$ MeV. The gray regions are excluded by NA64 and KLOE searches, while the region inside the red contour is excluded by Møller scattering. Here we assume $\mathrm{BR}(X \to e^+e^-) = 1$.

The discrepancy of 3.2σ[10] could be explained assuming a BSM contribution from a light axial boson [263]. The actual best fit from the data reads as [260]

$$\frac{(a_p - a_n)C_A^e}{g_A m_X^2} = 2.60^{+1.50}_{-1.60} \times 10^{-10}\ \mathrm{MeV}^{-2}\ , \tag{3.120}$$

[10]Using the latest radiative corrections from [261, 262], the full branching ratio extrapolated from the KTeV measurement is $\mathrm{BR}(\pi^0 \to e^+e^-)_{\mathrm{exp}} = (6.85 \pm 0.27 \pm 0.23) \times 10^{-8}$, thus reducing the discrepancy to 1.8σ.

where C_A^e is the axial coupling of the X boson to the electron, see Eq. (3.93). A light vector contributes to the anomalous magnetic moment of the electron. The SM prediction from the measurement of the fine structure constant α from Cs atoms [264] and the more recent prediction based on the measurement of α from Rb atoms [265] are in contradiction among themselves. By asking that the BSM contribution from the X boson given by [266]

$$\delta a_l^{\rm BSM} = \frac{C_V^2}{4\pi^2}\frac{m_\ell^2}{m_X^2}\frac{1}{2}\int_0^1 {\rm d}z\ \frac{2m_X^2 z^2(z-1)}{m_X^2(z-1)-m_\ell^2 z^2} + \frac{C_A^2}{4\pi^2}\frac{m_\ell^2}{m_X^2}\frac{1}{2}\int_0^1 {\rm d}z\ \frac{4z^3 m_\ell^2 + 2z m_X^2(4-5z+z^2)}{m_X^2(z-1)-m_\ell^2 z^2}\ , \tag{3.121}$$

doesn't overshoot the discrepancy between the central values of the SM prediction and the experimental measurement [267] one obtains two different constraints, depending on the choice of the SM prediction

$$\delta a_e^{\rm BSM}(Rb) \simeq 7.6\times 10^{-6} {C_V^e}^2 - 3.80\times 10^{-5} {C_A^e}^2 \in [0 - 0.48\times 10^{-12}]\ , \tag{3.122}$$

$$\delta a_e^{\rm BSM}(Cs) \simeq 7.6\times 10^{-6} {C_V^e}^2 - 3.80\times 10^{-5} {C_A^e}^2 \in [-0.88\times 10^{-12} - 0]\ . \tag{3.123}$$

The Cs atoms SM prediction naturally suggests a pure axial boson and the discrepancy observed in the electron anomalous magnetic moment would be resolved at 1σ with an electron coupling

$$C_A^e = \pm(1.52 \pm 0.31)\times 10^{-4}\ . \tag{3.124}$$

By fixing this value for C_A^e, we have shown in Fig. 3.7 the parameter space of the nucleon couplings which can explain the KTeV anomaly see Eq. (3.120), for the two distinct cases $C_A^e > 0$ and $C_A^e < 0$.

Allowing instead for both a vector and axial contribution to the electron coupling, in the upper panel of Fig 3.8 we show the values of the isovector nucleon axial coupling $a_p - a_n$ able to explain the KTeV anomaly at 1σ and assuming the discrepancy observed in the electron anomalous magnetic moment to be resolved for the Cs atoms (blue) and Rb atoms (orange) SM prediction for the two distinct cases $C_A^e > 0$ and $C_A^e < 0$. In the lower panel of the same figure we show instead the most relevant bounds on this scenario with generic X vector couplings to electrons, again for ${\rm BR}(X \to e^+e^-) = 1$, which arise from the measurement of e^+e^- scattering from the KLOE experiment at DAΦNe collider [239], measurements on parity violation in Møller scattering at SLAC [240] and beam dump experiment at NA64 [244,245], see App. 3.6 for details. Interestingly, the PADME experiment will completely cover the region between the NA64 and the KLOE exclusions thus allowing for a strong test of the existence of the X boson [211, 212].

3.7.3 Minimal SM extension with a new $U(1)$ gauge symmetry

A common proposal in order to include a light vector X in a SM extension is by enlarging its gauge group $G_{\rm SM} = SU(3)_c \times SU(2)_W \times U(1)_Y$ with a new abelian symmetry $U(1)_X$[11]. In a minimal scenario, it is natural to assume that the SM Lagrangian is symmetric under $U(1)_X$. It follows that the $U(1)_X$ charges are a linear combination of the hypercharge Y and all the accidental symmetries of the SM: the baryon number B and the three lepton family numbers $L_{e,\mu,\tau}$. When the gauge group $G_{\rm SM} \times U(1)_X$ is broken to $SU(3)_c \times U(1)_Q$, the X field mixes with the other neutral gauge bosons in order to compose the physical states: the photon γ, the Z^0 boson and the light boson X. Moreover, once the symmetry is broken, the X charges acquire a contribution from the diagonal weak isospin T_{W_3}. In the quark sector, the X couplings are then a linear combination of three independent charge assignments: B, $Y = Q - T_{W_3}$ and T_{W_3}. The baryon number B and the electric

[11] The resulting model is typically not anomaly free, leading at low energy to stringent constraints for a light vector boson [14, 15]. A possible way out has been described in [1].

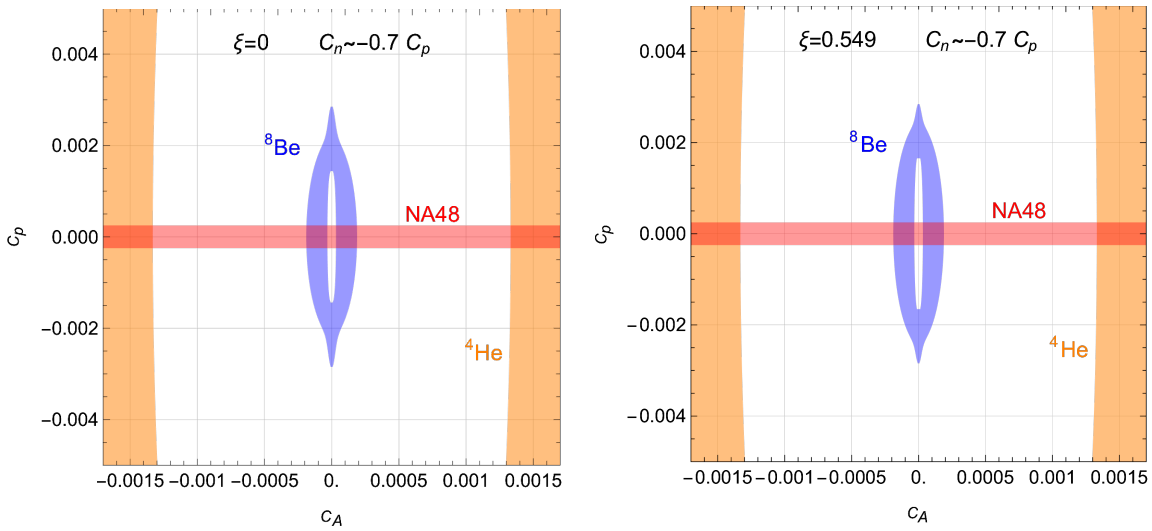

Figure 3.9: Regions of the $C_p - C_A$ couplings for the minimal SM extension with a new $U(1)_X$ symmetry where the ^{8}Be (blue) and ^{4}He (orange) anomalous ATOMKI transition can be explained at 1σ. Inside the red region the NA48 bound is satisfied. In the left and right panel we assume $\xi = 0$ and $\xi = 0.549$ respectively, see App. 3.4.3 for details.

charge Q are vector symmetries so only the weak isospin T_{W_3} induces an axial coupling. Thus, the axial couplings of the light quarks satisfy

$$C_A^u = -C_A^d = -C_A^s = -C_A^e \equiv C_A \tag{3.125}$$

while the vector coupling for up and down quarks are independent. The nucleon couplings are obtained from the quark ones by Eq. (B.3) and Eq. (B.11). However, the results from atomic parity violation experiments [248], see App. 3.6, strongly constrain these couplings, and require for them (product of) values so small that the ATOMKI anomalies cannot be explained, see Eq. (3.101). A way to avoid this bound is to assume somehow a magical cancellation between the up and down vector couplings, which is

$$C_V^d = -\frac{188}{211} C_V^u \ , \tag{3.126}$$

thus

$$C_n = -\frac{55}{78} C_p \simeq -0.7\, C_p \ . \tag{3.127}$$

Hence, we are left with two independent couplings, C_p and C_A. However, as we show in Fig. 3.9, there is no possible simultaneously explanation of the ^{8}Be and ^{4}He anomalies in the minimal BSM scenario considered here for both choices of the isospin breaking parameter ξ, which produce almost indistinguishable results.

Conclusion

Differently from new physics at the TeV scale or above, weakly-interacting light new physics could be found at the "low-energy frontier". Experiments that use intense beams of photons, charged particles, and/or sensitive detectors may be used to directly produce and study new, feebly-interacting particles that lie well below the Weak scale. Existing facilities and technologies and small-size experiments enable the exploration of dark sectors. A rich, diverse, and low-cost experimental program is already underway that has the potential for one or more game-changing discoveries. Current ideas for extending the searches to smaller couplings and higher masses increase this potential markedly. In the previous chapters, we explore different scenarios of the rich phenomenology of weakly-interacting light new physics. To do so, we investigate a $SM + X$ scenario in a EFT framework where X is a light new state which can range from a gauge boson to RHNs with masses at the GeV scale.

For the first case, we have revisited the case of light vector bosons coupled to anomalous currents which are UV completed by new anomaly-canceling heavy fermions (anomalons). After the latter have been integrated out, WZ terms of the type in Eq. (1.21) are generated. On the one hand, they take care of anomaly cancellation in the IR and, on the other, they source the energy-enhanced emission of longitudinally polarized vectors, $\mathcal{X}$, which typically results in very strong bounds on $g_X/m_{\mathcal{X}} \propto 1/v_X$ whenever the decay channels $Z \to \gamma\mathcal{X}$, $B \to K\mathcal{X}$, $K \to \pi\mathcal{X}$, etc, are kinematically open [14,15]. Here, we have studied the model-dependence of such bounds, considering as a paradigmatic framework the gauging of the most general (anomalous) linear combination of SM global symmetries, $\mathrm{U}(1)_X$, with the generator X given in Eq. (1.1). To this end, we provided a UV completion including electroweak anomalons $\mathcal{L} + \mathcal{E} + \mathcal{N}$ (cf. Table 1.1) and conclude (cf. e.g. Eq. (1.39)) that the bounds mentioned above on light $\mathcal{X}$ can be evaded in the limit where the mass of the electroweak anomalons comes mostly from the Higgs VEV. We show that such anomalon fields predict a $h \to Z\gamma$ rate in agreement with the recent measurement of ATLAS and CMS but the updated direct search for non-decoupling charged leptons push the model beyond the edge of perturbativity.

For the second case, we have studied the phenomenological consequences of a dipole operator between RH neutrino fields. This is described by the νSMEFT $d = 5$ operator $\bar{N}_2\sigma^{\mu\nu}N_1B_{\mu\nu}$ and triggers the decay $N_2 \to N_1\gamma$, which is the subject of our study. Motivated by the current experimental and theoretical interest, we have focused on RH neutrino masses in the GeV range and considered the regime in which N_2 is long-lived, with a proper decay length of $\mathcal{O}(10^{-2} - 10^3\,\mathrm{m})$, while N_1 is considered to be stable on these length scales. In the facilities at intensity-frontier the RH neutrinos are produced in N_1N_2 pairs through the dipole operator, either via meson decay or via direct production. Then, RH neutrinos give rise to single$-\gamma$ events through $N_2 \to N_1\gamma$ decays, which can be detected by these experiments in a background controlled environment. Our main results are summarized in Fig. 2.1 where we show that SHiP will be able to probe ample regions of the parameter space not yet excluded by current data, testing Wilson coefficients up to $\Lambda \sim 10^5$ GeV, while the sensitivity of FASER 2 is more limited.

Finally in the last part of the thesis, motivated by the latest experimental results recently released

by the ATOMKI collaboration, we have critically re-examined the possible theoretical interpretation of the observed anomalies in ^{8}Be, ^{4}He and ^{12}C anomalies in terms of a BSM boson X with mass ~ 17 MeV. After having reviewed the current status of the ATOMKI results and the kinematic of the observed excesses we have employed a multipole expansion formalism to compute the anomalous decay rate for the decay of the excited nuclei into an e^+e^- pair via an intermediate on-shell BSM state. Our results identify an axial vector state as the most promising candidate to simultaneously explain all the three anomalous nuclear decay, while the other spin/parity assignments seems disfavored for a combined explanation. However, the axial nuclear matrix element of the ^{12}C transition is currently unknown and our conclusions are based on an order of magnitude estimate for its value. Before being able to make a definite claim regarding the possibility of combined explanation of the ATOMKI anomalies with an axial vector state, this matrix elements need to be evaluated. Intriguingly, the hypothesis of an axial vector state can also simultaneously accommodate other experimental anomalies, as the one observed by the KTeV experiment in $\pi^0 \to e^+e^-$ decay, while being compatible with the conflicting measurements of the anomalous magnetic moment of the electron $(g-2)_e$ and other experimental constraints. The independent experiments that will be performed by the MEG II experiment [205] at PSI and the by the Montreal Tandem accelerator [207] will definitely probe the ATOMKI anomalies and also the PADME experiment [209, 210] in Frascati will test the available parameter space for the coupling of the X boson to electrons relevant for the explanation of the ATOMKI anomalies [211, 212]. Thus it will be soon understood whether these anomalies are merely due to unaccounted SM and/or experimental effects or else are the first signs of the long sought new physics beyond the Standard Model.

Appendix A

Calculation of the Wess-Zumino terms

In this Appendix we present the calculation of the effective WZ terms involving gauge and Goldstone bosons that arise after integrating out heavy fermionic degrees of freedom. In particular, we focus on the 3-point vertices involving the epsilon tensor $\epsilon^{\alpha\beta\mu\nu}$ (with $\epsilon^{0123} = 1$) which are related to anomaly cancellation in the EFT when the heavy fermions are integrated out.

Toy model

We assume a toy model with a set of gauge bosons G^A_μ related to the generators Q^A of the gauge symmetry group $\mathcal{G}$ (that can be in general semi-simple). The model contains a fermionic sector, whose fields are labeled as ψ_i, that acquire a mass term $\mathcal{M}_{ij}$ after a spontaneously symmetry breaking (SSB) mechanism. The $(\frac{1}{2}, 0)$ and $(0, \frac{1}{2})$ Lorentz components of the ψ field are separately (reducible) representations of $\mathcal{G}$ and the generators act on them as

$$Q^A \psi_i = \sum_j (Q^A_L)_{ij} \psi_{jL} + \sum_j (Q^A_R)_{ij} \psi_{jR} \,, \tag{A.1}$$

where $(Q^A_{L,R})_{ij}$ are the matrix representation of the gauge multiplets $\psi_{L,R} \equiv P_{L,R}\psi$. We restrict ourselves to models with a $\mathrm{U}(1)_\psi$ symmetry corresponding to the fermionic number of the ψ fields ($\psi_i \to e^{i\phi}\psi_i$). The real scalar Higgs fields, responsible for the SSB mechanism, are labeled as $H_a = (H_a)^*$ and belong to a (reducible) representation of the gauge group $\mathcal{G}$. By performing an infinitesimal transformation of angle α_A along the Q^A generator, the H_a fields transform like

$$\delta H_a = \sum_b g_A \alpha_A (i Q^A_H)_{ab} H_b \,, \tag{A.2}$$

where $(iQ^A_H)_{ab}$ is a real and antisymmetric matrix. Hence,

$$\mathcal{L}_{\text{toy model}} \supset \sum_i \bar{\psi}_i i \partial\!\!\!/ \psi_i - \sum_{a,i,j} H_a (\bar{\psi}_{iL} \mathcal{Y}^a_{ij} \psi_{jR} + \text{h.c.}) - \sum_A g_A G^A_\mu J^{\mu A} \,, \tag{A.3}$$

with

$$J^{\mu A} = \sum_{i,j} \Big[\bar{\psi}_{iL} \gamma^\mu (Q^A_L)_{ij} \psi_{jL} + \bar{\psi}_{iR} \gamma^\mu (Q^A_R)_{ij} \psi_{jR} \Big] \,. \tag{A.4}$$

The Yukawa couplings must preserve gauge invariance and hence they satisfy

$$\sum_k \mathcal{Y}^a_{ik}(Q^A_R)_{kj} - \sum_k (Q^A_L)_{ik}\mathcal{Y}^a_{kj} + \sum_b \mathcal{Y}^b_{ij}(Q^A_H)_{ba} = 0\,. \tag{A.5}$$

The Higgs fields acquire the VEVs $\langle H_a\rangle = v_a$ which break the gauge group, leaving an unbroken subgroup $\mathcal{G}_0$. Then, the mass matrix of the ψ fields is given by

$$\mathcal{M}_{ij} = \sum_a \mathcal{Y}^a_{ij} v_a\,, \tag{A.6}$$

leading to

$$\begin{aligned}\mathcal{L}_{\text{toy model}} \supset & \sum_i \bar\psi_i i\partial\!\!\!/\psi_i - \sum_{i,j}(\bar\psi_{iL}\mathcal{M}_{ij}\psi_{jR} + \text{h.c.}) \\ & - \sum_{a,i,j}\tilde H_a(\bar\psi_{iL}\mathcal{Y}^a_{ij}\psi_{jR} + \text{h.c.}) - \sum_A g_A G^A_\mu J^{\mu A}\,,\end{aligned} \tag{A.7}$$

where $\tilde H_a = H_a - v_a$ are the Higgs fluctuations around the vacuum.

In order to go in the mass basis, the mass matrix $\mathcal{M}$ is diagonalized via the bi-unitary transformations $\psi_R \to U_R\,\psi_R$ and $\psi_L \to U_L\,\psi_L$, which by construction satisfy $U_L^\dagger \mathcal{M} U_R = \text{diag}(m_1, m_2, ...)$. This yields

$$\mathcal{L}_{\text{toy model}} \supset \sum_i \bar\psi_i(i\partial\!\!\!/ - m_i)\psi_i - \sum_A g_A G^A_\mu J^{\mu A}_U - \sum_{a,i,j}\tilde H_a\bar\psi_i(\hat{\mathcal{Y}}^a_R P_R + \hat{\mathcal{Y}}^a_L P_L)_{ij}\psi_j\,, \tag{A.8}$$

where $\hat{\mathcal{Y}}^a_R = U_L^\dagger \mathcal{Y}^a U_R = (\hat{\mathcal{Y}}^a_L)^\dagger$, while the gauge currents in the mass basis are equal to

$$J^{\mu A}_U = \sum_{i,j}\Big[\bar\psi_{iL}\gamma^\mu (U_L^\dagger Q^A_L U_L)_{ij}\psi_{jL} + \bar\psi_{iR}\gamma^\mu(U_R^\dagger Q^A_R U_R)_{ij}\psi_{jR}\Big]\,. \tag{A.9}$$

After integrating out the heavy fermion fields, we get EFT operators of the type

$$\begin{aligned}\mathcal{L}_{\text{toy model}} \supset & \sum_{A,B,C}\frac{g_A g_B g_C}{48\pi^2} C^{ABC}\epsilon^{\alpha\mu\nu\beta} G^A_\alpha G^B_\mu \partial_\beta G^C_\nu \\ & - \sum_{a,B,C}\frac{g_B g_C}{48\pi^2} D^{aBC}\epsilon^{\mu\nu\alpha\beta}\tilde H_a \partial_\alpha G^B_\mu \partial_\beta G^C_\nu\,,\end{aligned} \tag{A.10}$$

in terms of the EFT coefficients $C^{ABC} = -C^{BAC}$ and $D^{aBC} = D^{aCB}$ that we want to compute. Moreover, integrating by parts the term on the first line of Eq. (A.10), one also obtains

$$C^{ABC} + C^{CAB} + C^{BCA} = 0\,. \tag{A.11}$$

γ_5 in dimensional regularization

Dimensional regularization allows to regularize the divergences arising from loop calculations in 4 dimensions, while explicitly preserving Lorentz covariance and gauge invariance. In the d-dimensional spacetime, the mass dimensions of the quantum fields are equal to

$$[\psi] = \frac{d-1}{2}\,, \qquad [H] = [G_\mu] = \frac{d-2}{2}\,. \tag{A.12}$$

Hence, in order to keep the gauge couplings dimensionless, one introduces the renormalization scale μ by the substitution

$$g \to \mu^{\frac{4-d}{2}} g \tag{A.13}$$

in the Lagrangian. The use of dimensional regularization poses some potential problems in calculations where the γ^5 matrix is involved. In fact, γ^5 (or equivalently the antisymmetric tensor $\epsilon^{\alpha\beta\mu\nu}$) is a quantity whose definition is strictly connected to the fact that space-time is four dimensional, and a definition in d dimensions requires special care. Here, we adopt the Breitenlohner-Maison-'t Hooft-Veltman (BMHV) scheme, which is able to reproduce the chiral anomaly (see [268] for a recent review).

We decompose all matrices into a four-dimensional (denoted by bars) and an extra-dimensional (also called "evanescent", denoted by hats) component:

$$\gamma^\mu = \bar{\gamma}^\mu + \hat{\gamma}^\mu \,, \tag{A.14}$$

where $\bar{\gamma}^\mu$ is non-zero only when μ takes the ordinary values $0, 1, 2, 3$ and $\hat{\gamma}^\mu$ vanishes for $\mu = 0, 1, 2, 3$. Correspondingly, the matrix tensor $g_{\mu\nu}$ has a four-dimensional and an extra-dimensional part,

$$g_{\mu\nu} = \bar{g}_{\mu\nu} + \hat{g}_{\mu\nu} \,, \tag{A.15}$$

while mixed components vanish. The gamma matrices satisfy

$$\{\bar{\gamma}^\mu, \bar{\gamma}^\nu\} = 2\bar{g}^{\mu\nu} \,, \qquad \{\hat{\gamma}^\mu, \hat{\gamma}^\nu\} = 2\hat{g}^{\mu\nu} \,, \qquad \{\bar{\gamma}^\mu, \hat{\gamma}^\nu\} = 0 \,. \tag{A.16}$$

Then, we simply define γ^5 as in four dimensions, that is

$$\gamma^5 = i\bar{\gamma}^0\bar{\gamma}^1\bar{\gamma}^2\bar{\gamma}^3 \,. \tag{A.17}$$

It is easy to check that the definition in Eq. (A.17) implies

$$\{\gamma^5, \bar{\gamma}^\mu\} = 0 \,, \qquad [\gamma^5, \hat{\gamma}^\mu] = 0 \,, \tag{A.18}$$

$$\mathrm{Tr}\, \gamma^5\gamma^\alpha\gamma^\beta\gamma^\mu\gamma^\nu = \mathrm{Tr}\, \gamma^5\bar{\gamma}^\alpha\bar{\gamma}^\beta\bar{\gamma}^\mu\bar{\gamma}^\nu = 4i\epsilon^{\alpha\beta\mu\nu} \,, \tag{A.19}$$

which is the correct four-dimensional result.

In a general chiral gauge theory, the fermion fields are introduced as Weyl spinors whose formalism is intrinsically tied to 4-dimensional space. In d dimensions, we replace the Weyl spinors by projections of Dirac spinors, which can be generalized to arbitrary dimensions. The right and left projections are $P_{R,L} = \frac{1}{2}(1 \pm \gamma_5)$, as in the 4-dimensional space. Then, there are three possible inequivalent choices for the d-dimensional extension of the right-handed chiral current $\bar{\psi}_{iR}\gamma^\mu\psi_{jR}$ coupled to gauge bosons, which are

$$\bar{\psi}_i P_L \gamma^\mu \psi_j \,, \qquad \bar{\psi}_i \gamma^\mu P_R \psi_j \,, \qquad \bar{\psi}_i P_L \gamma^\mu P_R \psi_j \,. \tag{A.20}$$

They are different because $P_L\gamma^\mu \neq \gamma^\mu P_R$ in d dimensions. Each of these does lead to valid d-dimensional extensions of the model that are perfectly renormalizable using dimensional regularization and the BMHV scheme. However, the intermediate calculations and the final d-dimensional results will differ, depending on the choice for this interaction term. Our choice for this work is to use the third option, that is

$$\bar{\psi}_i P_L \gamma^\mu P_R \psi_j = \bar{\psi}_{iR} \bar{\gamma}^\mu \psi_{jR} \,, \tag{A.21}$$

is the most symmetric one, and leads to the simplest expressions. Similar considerations hold for the left-handed chiral current $\bar{\psi}_{iL}\gamma^\mu\psi_{jL}$. A different choice has to be taken instead for the kinetic terms

$\bar{\psi}_{iR} i\partial\!\!\!/ \psi_{iR}$ and $\bar{\psi}_{iL} i\partial\!\!\!/ \psi_{iL}$. Indeed, in order to properly regularize the theory, we need to consider the full Dirac fermion kinetic term $\bar{\psi}_i i\partial\!\!\!/ \psi_i$, including the evanescent terms.

Once the regulated amplitude is well-defined, we can perform all the necessary subtractions of the divergences of its sub-diagrams and the resulting finite expression is interpreted in the physical 4-dimensional space by setting all quantities to their 4-dimensional values, i.e. first taking the $d \to 4$ limit and then, setting all remaining evanescent terms to zero.

1-loop matching

The epsilon tensor structure occurs in the 3-point functions $\Gamma^{\alpha\mu\nu}_{ABC}(x,y,z)$ and $\Gamma^{\mu\nu}_{aBC}(x,y,z)$ at 1-loop through fermionic triangle diagrams (see Fig. A.1). The amplitudes in momentum space are defined via

$$\int \mathrm{d}^4x\, \mathrm{d}^4y\, \mathrm{d}^4z\, e^{i(xq_1+yq_2+zq_3)}\, \Gamma^{\alpha\mu\nu}_{ABC}(x,y,z)|_{\text{1-loop}} = (2\pi)^4\delta^{(4)}(q_1+q_2+q_3)\, \mu^{\frac{4-d}{2}}\, iM^{\alpha\mu\nu}_{ABC}(q_1,q_2,q_3)\,, \tag{A.22}$$

and

$$\int \mathrm{d}^4x\, \mathrm{d}^4y\, \mathrm{d}^4z\, e^{i(xq_1+yq_2+zq_3)}\, \Gamma^{\mu\nu}_{aBC}(x,y,z)|_{\text{1-loop}} = (2\pi)^4\delta^{(4)}(q_1+q_2+q_3)\, \mu^{\frac{4-d}{2}}\, iM^{\mu\nu}_{aBC}(q_1,q_2,q_3)\,, \tag{A.23}$$

which yield

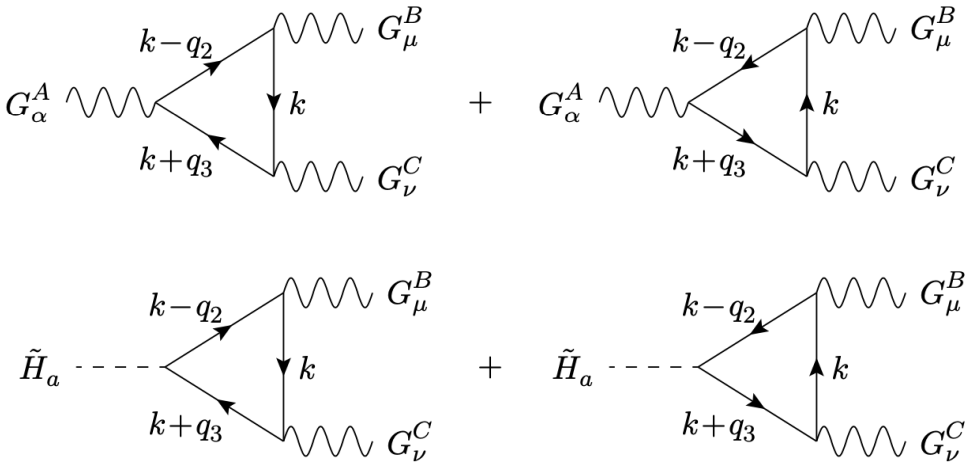

Figure A.1: Feynman diagrams relative to the 3-point functions in Eqs. (A.22)–(A.23).

$$
\begin{aligned}
M^{\alpha\mu\nu}_{ABC} = & \sum_{\substack{i,j,k\\ \chi_1,\chi_2,\chi_3}} g_A g_B g_C (U^\dagger_{\chi_1} Q^A_{\chi_1} U_{\chi_1})_{jk} (U^\dagger_{\chi_2} Q^B_{\chi_2} U_{\chi_2})_{ki} (U^\dagger_{\chi_3} Q^C_{\chi_3} U_{\chi_3})_{ij} \\
& \qquad \times i\mu^{4-d} \int \frac{\mathrm{d}^d k}{(2\pi)^d} \frac{\mathrm{Tr_D}[\bar\gamma^\mu P_{\chi_2} (\not k + m_i) \bar\gamma^\nu P_{\chi_3} (\not k + \not q_3 + m_j) \bar\gamma^\alpha P_{\chi_1} (\not k - \not q_2 + m_k)]}{[k^2 - m_i^2]\,[(k+q_3)^2 - m_j^2]\,[(k-q_2)^2 - m_k^2]} \\
& + \sum_{\substack{i,j,k\\ \chi_1,\chi_2,\chi_3}} g_A g_C g_B (U^\dagger_{\chi_1} Q^A_{\chi_1} U_{\chi_1})_{kj} (U^\dagger_{\chi_3} Q^C_{\chi_3} U_{\chi_3})_{ji} (U^\dagger_{\chi_2} Q^B_{\chi_2} U_{\chi_2})_{ik} \\
& \qquad \times i\mu^{4-d} \int \frac{\mathrm{d}^d k}{(2\pi)^d} \frac{\mathrm{Tr_D}[\bar\gamma^\nu P_{\chi_3} (\not k + m_i) \bar\gamma^\mu P_{\chi_2} (\not k + \not q_2 + m_k) \bar\gamma^\alpha P_{\chi_1} (\not k - \not q_3 + m_j)]}{[k^2 - m_i^2]\,[(k+q_2)^2 - m_k^2]\,[(k-q_3)^2 - m_j^2]} \,,
\end{aligned}
\tag{A.24}
$$

and

$$
\begin{aligned}
M^{\mu\nu}_{aBC} = & \sum_{\substack{i,j,k\\ \chi_1,\chi_2,\chi_3}} g_B g_C (\hat{\mathcal{Y}}^a_{\chi_1})_{jk} (U^\dagger_{\chi_2} Q^B_{\chi_2} U_{\chi_2})_{ki} (U^\dagger_{\chi_3} Q^C_{\chi_3} U_{\chi_3})_{ij} \\
& \qquad \times i\mu^{4-d} \int \frac{\mathrm{d}^d k}{(2\pi)^d} \frac{\mathrm{Tr_D}[\bar\gamma^\mu P_{\chi_2} (\not k + m_i) \bar\gamma^\nu P_{\chi_3} (\not k + \not q_3 + m_j) P_{\chi_1} (\not k - \not q_2 + m_k)]}{[k^2 - m_i^2]\,[(k+q_3)^2 - m_j^2]\,[(k-q_2)^2 - m_k^2]} \\
& + \sum_{\substack{i,j,k\\ \chi_1,\chi_2,\chi_3}} g_B g_C (\hat{\mathcal{Y}}^a_{\chi_1})_{kj} (U^\dagger_{\chi_3} Q^C_{\chi_3} U_{\chi_3})_{ji} (U^\dagger_{\chi_2} Q^B_{\chi_2} U_{\chi_2})_{ik} \\
& \qquad \times i\mu^{4-d} \int \frac{\mathrm{d}^d k}{(2\pi)^d} \frac{\mathrm{Tr_D}[\bar\gamma^\nu P_{\chi_3} (\not k + m_i) \bar\gamma^\mu P_{\chi_2} (\not k + \not q_2 + m_k) P_{\chi_1} (\not k - \not q_3 + m_j)]}{[k^2 - m_i^2]\,[(k+q_2)^2 - m_k^2]\,[(k-q_3)^2 - m_j^2]} \,.
\end{aligned}
\tag{A.25}
$$

Since we have regularized the theory, the loop integrals over momentum k are convergent and can be evaluated with the usual well-known techniques. Next, we perform the traces over the Dirac indices to extract the terms involving the epsilon tensor structure we are interested on. One finds that such terms are finite, i.e. they do not contain $1/(d-4)$ poles, and are independent from the renormalization scale μ. Hence, we can send $d \to 4$ and set the evanescent components to zero.

In order to obtain the EFT coefficients in Eq. (A.10), we have to match the expressions that we have calculated above to the EFT matrix elements in the limit of heavy fermion masses, i.e.

$$
\lim_{\substack{m^2_{i,j,k} \gg \\ q_2^2, q_3^2, q_2 q_3}} M^{\alpha\mu\nu}_{ABC}|_{\epsilon-tensor} = \frac{g_A g_B g_C}{24\pi^2} \epsilon^{\alpha\mu\nu\beta} (C^{ABC} i q_3 + C^{CAB} i q_2 + C^{BCA} i q_1)_\beta \,, \tag{A.26}
$$

and

$$
\lim_{\substack{m^2_{i,j,k} \gg \\ q_2^2, q_3^2, q_2 q_3}} M^{\mu\nu}_{aBC}|_{\epsilon-tensor} = \frac{g_B g_C}{24\pi^2} D^{aBC} \epsilon^{\mu\nu\alpha\beta} q_{2\alpha} q_{3\beta} \,. \tag{A.27}
$$

Thus we get

$$
\begin{aligned}
C^{ABC} = \int_0^{+\infty}\mathrm{d}s\int_0^1\mathrm{d}x\int_0^1\mathrm{d}y\int_0^1\mathrm{d}z\,2\,\delta(1-x-y-z)\times \\
\times\,\mathrm{Re}\Big\{ 3y\,\mathrm{Tr}\Big[e^{-sy\mathcal{M}^\dagger\mathcal{M}}Q_R^A\mathcal{M}^\dagger e^{-sz\mathcal{M}\mathcal{M}^\dagger}Q_L^B e^{-sx\mathcal{M}\mathcal{M}^\dagger}Q_L^C\mathcal{M}\Big] \\
-3y\,\mathrm{Tr}\Big[e^{-sy\mathcal{M}^\dagger\mathcal{M}}Q_R^B\mathcal{M}^\dagger e^{-sz\mathcal{M}\mathcal{M}^\dagger}Q_L^A e^{-sx\mathcal{M}\mathcal{M}^\dagger}Q_L^C\mathcal{M}\Big] \\
+3y\,\mathrm{Tr}\Big[e^{-sy\mathcal{M}\mathcal{M}^\dagger}Q_L^B\mathcal{M}e^{-sz\mathcal{M}^\dagger\mathcal{M}}Q_R^A e^{-sx\mathcal{M}^\dagger\mathcal{M}}Q_R^C\mathcal{M}^\dagger\Big] \\
-3y\,\mathrm{Tr}\Big[e^{-sy\mathcal{M}\mathcal{M}^\dagger}Q_L^A\mathcal{M}e^{-sz\mathcal{M}^\dagger\mathcal{M}}Q_R^B e^{-sx\mathcal{M}^\dagger\mathcal{M}}Q_R^C\mathcal{M}^\dagger\Big] \\
+y\,\mathrm{Tr}\Big[e^{-sy\mathcal{M}^\dagger\mathcal{M}}\mathcal{M}^\dagger\mathcal{M}Q_R^A e^{-sz\mathcal{M}^\dagger\mathcal{M}}Q_R^B e^{-sx\mathcal{M}^\dagger\mathcal{M}}Q_R^C\Big] \\
-x\,\mathrm{Tr}\Big[e^{-sy\mathcal{M}^\dagger\mathcal{M}}Q_R^A e^{-sz\mathcal{M}^\dagger\mathcal{M}}Q_R^B e^{-sx\mathcal{M}^\dagger\mathcal{M}}\mathcal{M}^\dagger\mathcal{M}Q_R^C\Big] \\
+x\,\mathrm{Tr}\Big[e^{-sy\mathcal{M}\mathcal{M}^\dagger}Q_L^A e^{-sz\mathcal{M}\mathcal{M}^\dagger}Q_L^B e^{-sx\mathcal{M}\mathcal{M}^\dagger}\mathcal{M}\mathcal{M}^\dagger Q_L^C\Big] \\
-y\,\mathrm{Tr}\Big[e^{-sy\mathcal{M}\mathcal{M}^\dagger}\mathcal{M}\mathcal{M}^\dagger Q_L^A e^{-sz\mathcal{M}\mathcal{M}^\dagger}Q_L^B e^{-sx\mathcal{M}\mathcal{M}^\dagger}Q_L^C\Big]\Big\},
\end{aligned}
\tag{A.28}
$$

and

$$
\begin{aligned}
D^{aBC} = \int_0^{+\infty}\mathrm{d}s\int_0^1\mathrm{d}x\int_0^1\mathrm{d}y\int_0^1\mathrm{d}z\,6\,\delta(1-x-y-z)\times \\
\times\,\mathrm{Im}\Big\{ x\,\mathrm{Tr}\Big[e^{-sz\mathcal{M}^\dagger\mathcal{M}}Q_R^B\mathcal{M}^\dagger e^{-sx\mathcal{M}\mathcal{M}^\dagger}Q_L^C e^{-sy\mathcal{M}\mathcal{M}^\dagger}\mathcal{Y}^a\Big] \\
+x\,\mathrm{Tr}\Big[e^{-sz\mathcal{M}^\dagger\mathcal{M}}Q_R^C\mathcal{M}^\dagger e^{-sx\mathcal{M}\mathcal{M}^\dagger}Q_L^B e^{-sy\mathcal{M}\mathcal{M}^\dagger}\mathcal{Y}^a\Big] \\
+y\,\mathrm{Tr}\Big[e^{-sy\mathcal{M}^\dagger\mathcal{M}}\mathcal{M}^\dagger Q_L^C e^{-sx\mathcal{M}\mathcal{M}^\dagger}Q_L^B e^{-sz\mathcal{M}\mathcal{M}^\dagger}\mathcal{Y}^a\Big] \\
+y\,\mathrm{Tr}\Big[e^{-sy\mathcal{M}^\dagger\mathcal{M}}\mathcal{M}^\dagger Q_L^B e^{-sx\mathcal{M}\mathcal{M}^\dagger}Q_L^C e^{-sz\mathcal{M}\mathcal{M}^\dagger}\mathcal{Y}^a\Big] \\
+y\,\mathrm{Tr}\Big[e^{-sz\mathcal{M}^\dagger\mathcal{M}}Q_R^B e^{-sx\mathcal{M}^\dagger\mathcal{M}}Q_R^C\mathcal{M}^\dagger e^{-sy\mathcal{M}\mathcal{M}^\dagger}\mathcal{Y}^a\Big] \\
+y\,\mathrm{Tr}\Big[e^{-sz\mathcal{M}^\dagger\mathcal{M}}Q_R^C e^{-sx\mathcal{M}^\dagger\mathcal{M}}Q_R^B\mathcal{M}^\dagger e^{-sy\mathcal{M}\mathcal{M}^\dagger}\mathcal{Y}^a\Big]\Big\}.
\end{aligned}
\tag{A.29}
$$

Reproducing the chiral anomaly in the EFT

A consistent gauge theory must be anomaly free and hence the chiral anomaly needs to cancel when we sum over all the fermion fields of the theory. If we integrate out a heavy fermionic sector of the complete UV model, the corresponding chiral anomaly is reproduced in the EFT action $\mathcal{S}_{eff}$ thanks to the WZ effective operators in Eq. (A.10). To show this, we make an infinitesimal transformation of angle α_A along the Q^A generator. The gauge fields G_μ^B and the Higgs fields $\tilde{H}_a$ transform like

$$
\delta\tilde{H}_a = \sum_b \alpha_A (iQ_H^A)_{ab} v_b \,+\, \text{linear terms}\,, \tag{A.30}
$$

$$
\delta G_\mu^B = -\delta_{AB}\,(\partial_\mu\alpha_B)/g_B \,+\, \text{linear terms}\,, \tag{A.31}
$$

which, from the variation of the effective Lagrangian in Eq. (A.10), yields

$$\begin{aligned}\delta\mathcal{S}_{eff} &= \sum_{BC}\frac{g_B g_C}{48\pi^2}\left[C^{ABC}+C^{ACB}+D^{aBC}(iQ_H^A)_{ab}v_b\right]\int \mathrm{d}^4x\,\alpha_A\partial_\alpha G_\mu^B\partial_\beta G_\nu^C\epsilon^{\mu\nu\alpha\beta}\\ &= \sum_{BC}\frac{g_B g_C}{48\pi^2}\left[\mathrm{Tr}\,Q_R^A\{Q_R^B,Q_R^C\}-\mathrm{Tr}\,Q_L^A\{Q_L^B,Q_L^C\}\right]\int \mathrm{d}^4x\,\alpha_A\partial_\alpha G_\mu^B\partial_\beta G_\nu^C\epsilon^{\alpha\mu\beta\nu}\,.\end{aligned} \tag{A.32}$$

WZ terms for massive vector bosons and Goldstone bosons

The VEVs of the Higgs fields contribute to the mass matrix $\mathcal{M}^2_{gauge}$ for the gauge bosons G_μ^A with elements

$$(\mathcal{M}^2_{gauge})_{AB} = \sum_{a,b,c} g_A(iQ_H^A)_{ca}v_a g_B(iQ_H^B)_{cb}v_b\,. \tag{A.33}$$

Since the matrix is real and symmetric, we can diagonalize it through an orthogonal matrix O_{AB} such that

$$\sum_{A,B} O_{DB}O_{CA}(\mathcal{M}^2_{gauge})_{AB} = m_C^2\delta_{CD}\,. \tag{A.34}$$

The massive eigenstates are then defined by

$$Z_\mu^A = \sum_B O_{AB}\,G_\mu^B\,, \tag{A.35}$$

with corresponding symmetry generator

$$\tilde{g}_A T^A = \sum_B O_{AB}\,g_B Q^B\,. \tag{A.36}$$

There are two scenarios for each generator T^A:

- $(iT_H^A)_{ab}v_b = 0$, if T^A belongs to the unbroken subgroup $\mathcal{G}_0$, such that the corresponding vector boson Z_μ^A is then massless, i.e. $m_A = 0$;
- $(iT_H^A)_{ab}v_b \neq 0$, if T^A is spontaneously broken by the Higgs VEVs. The corresponding Nambu-Goldstone boson η^A is given by

$$\eta^A = \sum_a t_a^A\tilde{H}_a\,, \tag{A.37}$$

  where $t_a^A = \tilde{g}_A(iT_H^A)_{ab}v_b/m_A$ are a (incomplete) set of orthogonal vectors in the Higgs space, i.e. $\sum_a t_a^A t_a^B = \delta_{AB}$. The Goldstone field is then eaten by the vector boson Z_μ^A which acquires a mass m_A.

The $\tilde{H}_a$ contains the Goldstone modes along the t_a^A directions while the remaining modes, orthogonal to the Goldstones, are all physical, i.e.

$$\tilde{H}_a = \sum_{\text{NG modes}} t_a^A\eta^A + \dots\,. \tag{A.38}$$

The interaction terms between the ψ fields and the Goldstone bosons are given by

$$\sum_a \mathcal{Y}_{ij}^a t_a^A = \frac{i\tilde{g}_A}{m_A}\sum_k\left[(T_L^A)_{ik}\mathcal{M}_{kj} - \mathcal{M}_{ik}(T_R^A)_{kj}\right]\,, \tag{A.39}$$

because of the gauge invariance of the Yukawa couplings. Upon an infinitesimal transformation of angle α_A along a broken T^A generator, the Goldstone field η^A transform like

$$\delta\eta^A = \alpha_A m_A + \text{linear terms}\,. \tag{A.40}$$

Finally, the effective operators in Eq. (A.10) written in terms of the Z_μ^A and η^A fields are

$$\sum_{A,B,C} \frac{\tilde{g}_A\tilde{g}_B\tilde{g}_C}{48\pi^2} C_Z^{ABC}\epsilon^{\alpha\mu\nu\beta} Z_\alpha^A Z_\mu^B \partial_\beta Z_\nu^C - \sum_{A,B,C} \frac{\tilde{g}_A\tilde{g}_B\tilde{g}_C}{48\pi^2} D_\eta^{ABC}\epsilon^{\mu\nu\alpha\beta} \frac{\eta^A}{m_A} \partial_\alpha Z_\mu^B \partial_\beta Z_\nu^C + \dots, \tag{A.41}$$

where the dots contain the interaction terms with the Higgs physical modes. The rotated EFT coefficients are equal to

$$\begin{aligned}
C_Z^{ABC} = \int_0^{+\infty}\mathrm{d}s \int_0^1 \mathrm{d}x \int_0^1 \mathrm{d}y \int_0^1 \mathrm{d}z\, 2\,\delta(1-x-y-z)\times \\
\times \mathrm{Re}\Big\{ 3y\,\mathrm{Tr}\Big[e^{-sy\mathcal{M}^\dagger\mathcal{M}} T_R^A \mathcal{M}^\dagger e^{-sz\mathcal{M}\mathcal{M}^\dagger} T_L^B e^{-sx\mathcal{M}\mathcal{M}^\dagger} T_L^C \mathcal{M}\Big] \\
-3y\,\mathrm{Tr}\Big[e^{-sy\mathcal{M}^\dagger\mathcal{M}} T_R^B \mathcal{M}^\dagger e^{-sz\mathcal{M}\mathcal{M}^\dagger} T_L^A e^{-sx\mathcal{M}\mathcal{M}^\dagger} T_L^C \mathcal{M}\Big] \\
+3y\,\mathrm{Tr}\Big[e^{-sy\mathcal{M}\mathcal{M}^\dagger} T_L^B \mathcal{M} e^{-sz\mathcal{M}^\dagger\mathcal{M}} T_R^A e^{-sx\mathcal{M}^\dagger\mathcal{M}} T_R^C \mathcal{M}^\dagger\Big] \\
-3y\,\mathrm{Tr}\Big[e^{-sy\mathcal{M}\mathcal{M}^\dagger} T_L^A \mathcal{M} e^{-sz\mathcal{M}^\dagger\mathcal{M}} T_R^B e^{-sx\mathcal{M}^\dagger\mathcal{M}} T_R^C \mathcal{M}^\dagger\Big] \\
+y\,\mathrm{Tr}\Big[e^{-sy\mathcal{M}^\dagger\mathcal{M}} \mathcal{M}^\dagger\mathcal{M} T_R^A e^{-sz\mathcal{M}^\dagger\mathcal{M}} T_R^B e^{-sx\mathcal{M}^\dagger\mathcal{M}} T_R^C\Big] \\
-x\,\mathrm{Tr}\Big[e^{-sy\mathcal{M}^\dagger\mathcal{M}} T_R^A e^{-sz\mathcal{M}^\dagger\mathcal{M}} T_R^B e^{-sx\mathcal{M}^\dagger\mathcal{M}} \mathcal{M}^\dagger\mathcal{M} T_R^C\Big] \\
+x\,\mathrm{Tr}\Big[e^{-sy\mathcal{M}\mathcal{M}^\dagger} T_L^A e^{-sz\mathcal{M}\mathcal{M}^\dagger} T_L^B e^{-sx\mathcal{M}\mathcal{M}^\dagger} \mathcal{M}\mathcal{M}^\dagger T_L^C\Big] \\
-y\,\mathrm{Tr}\Big[e^{-sy\mathcal{M}\mathcal{M}^\dagger} \mathcal{M}\mathcal{M}^\dagger T_L^A e^{-sz\mathcal{M}\mathcal{M}^\dagger} T_L^B e^{-sx\mathcal{M}\mathcal{M}^\dagger} T_L^C\Big]\Big\},
\end{aligned} \tag{A.42}$$

and

$$\begin{aligned}
D_\eta^{ABC} = \int_0^{+\infty}\mathrm{d}s \int_0^1 \mathrm{d}x \int_0^1 \mathrm{d}y \int_0^1 \mathrm{d}z\, 6\,\delta(1-x-y-z)\times \\
\times \mathrm{Re}\Big\{ x\,\mathrm{Tr}\Big[e^{-sz\mathcal{M}^\dagger\mathcal{M}} T_R^B \mathcal{M}^\dagger e^{-sx\mathcal{M}\mathcal{M}^\dagger} T_L^C e^{-sy\mathcal{M}\mathcal{M}^\dagger} (T_L^A\mathcal{M} - \mathcal{M}T_R^A)\Big] \\
+x\,\mathrm{Tr}\Big[e^{-sz\mathcal{M}^\dagger\mathcal{M}} T_R^C \mathcal{M}^\dagger e^{-sx\mathcal{M}\mathcal{M}^\dagger} T_L^B e^{-sy\mathcal{M}\mathcal{M}^\dagger} (T_L^A\mathcal{M} - \mathcal{M}T_R^A)\Big] \\
+y\,\mathrm{Tr}\Big[e^{-sy\mathcal{M}^\dagger\mathcal{M}} \mathcal{M}^\dagger T_L^C e^{-sx\mathcal{M}\mathcal{M}^\dagger} T_L^B e^{-sz\mathcal{M}\mathcal{M}^\dagger} (T_L^A\mathcal{M} - \mathcal{M}T_R^A)\Big] \\
+y\,\mathrm{Tr}\Big[e^{-sy\mathcal{M}^\dagger\mathcal{M}} \mathcal{M}^\dagger T_L^B e^{-sx\mathcal{M}\mathcal{M}^\dagger} T_L^C e^{-sz\mathcal{M}\mathcal{M}^\dagger} (T_L^A\mathcal{M} - \mathcal{M}T_R^A)\Big] \\
+y\,\mathrm{Tr}\Big[e^{-sz\mathcal{M}^\dagger\mathcal{M}} T_R^B e^{-sx\mathcal{M}^\dagger\mathcal{M}} T_R^C \mathcal{M}^\dagger e^{-sy\mathcal{M}\mathcal{M}^\dagger} (T_L^A\mathcal{M} - \mathcal{M}T_R^A)\Big] \\
+y\,\mathrm{Tr}\Big[e^{-sz\mathcal{M}^\dagger\mathcal{M}} T_R^C e^{-sx\mathcal{M}^\dagger\mathcal{M}} T_R^B \mathcal{M}^\dagger e^{-sy\mathcal{M}\mathcal{M}^\dagger} (T_L^A\mathcal{M} - \mathcal{M}T_R^A)\Big]\Big\}.
\end{aligned} \tag{A.43}$$

Properties of the WZ coefficients

In general, the expressions (A.42) and (A.43) involve non-trivial integrations which are difficult to compute. Special simplifications occur if the fermion mass term $\bar{\psi}_{Li}\mathcal{M}_{ij}\psi_{Rj}$ is invariant under any of the symmetry generators T^A. If so, the mass matrix $\mathcal{M}$ satisfies

$$\sum_k \mathcal{M}_{ik}(T_R^A)_{kj} - \sum_k (T_L^A)_{ik}\mathcal{M}_{kj} = 0\,. \tag{A.44}$$

Alternatively, the invariance of the mass term reads

$$\sum_{a,b} \mathcal{Y}_{ij}^a (T_H^A)_{ab} v_b = 0\,, \tag{A.45}$$

which could occur if T^A belongs to $\mathcal{G}_0$ or some Yukawa coupling vanishes. Then, one finds

$$C_Z^{ABC} = \begin{cases} \operatorname{Tr} T_R^A\{T_R^B, T_R^C\} - \operatorname{Tr} T_L^A\{T_L^B, T_L^C\} & \text{if} \quad \sum_{a,b}\mathcal{Y}_{ij}^a (T_H^{B,C})_{ab} v_b = 0\ , \\ \operatorname{Tr} T_L^A\{T_L^B, T_L^C\} - \operatorname{Tr} T_R^A\{T_R^B, T_R^C\} & \text{if} \quad \sum_{a,b}\mathcal{Y}_{ij}^a (T_H^{A,C})_{ab} v_b = 0\ , \\ 0 & \text{if} \quad \sum_{a,b}\mathcal{Y}_{ij}^a (T_H^{A,B})_{ab} v_b = 0\ . \end{cases} \tag{A.46}$$

and

$$D_\eta^{ABC} = 3\left[\operatorname{Tr} T_L^A\{T_L^B, T_L^C\} - \operatorname{Tr} T_R^A\{T_R^B, T_R^C\}\right] \qquad \text{if} \quad \sum_{a,b}\mathcal{Y}_{ij}^a (T_H^{B,C})_{ab} v_b = 0\,. \tag{A.47}$$

Note that D_η^{ABC} vanishes if

$$\sum_{a,b} \mathcal{Y}_{ij}^a (T_H^A)_{ab} v_b = 0\,, \tag{A.48}$$

i.e. if the fermion mass term is invariant under symmetry generator T^A.

Consider now an unbroken generator $Q \in \mathcal{G}_0$, hence satisfying

$$\sum_k \mathcal{M}_{ik}(Q_R)_{kj} - \sum_k (Q_L)_{ik}\mathcal{M}_{kj} = 0\,, \tag{A.49}$$

with the commutation rules

$$[Q, T^A] = \sum_B q_{AB} T^B\,. \tag{A.50}$$

Thanks to (A.49) and the cyclic property of the trace, the expression

$$C_Z^{ABC}|_{T^A \to [Q,T^A]} + C_Z^{ABC}|_{T^B \to [Q,T^B]} + C_Z^{ABC}|_{T^C \to [Q,T^C]} = 0 \tag{A.51}$$

is identically zero. Then, we find that the EFT coefficients satisfy

$$\sum_D (q_{AD} C_Z^{DBC} + q_{BD} C_Z^{ADC} + q_{CD} C_Z^{ABD}) = 0\,. \tag{A.52}$$

The same argument yields

$$\sum_D (q_{AD} D_\eta^{DBC} + q_{BD} D_\eta^{ADC} + q_{CD} D_\eta^{ABD}) = 0\,. \tag{A.53}$$

Appendix B

Nucleon effective couplings

We report in this section the matching between the effective interaction of the X boson with the nuclear matter and its interactions with the fundamental SM degrees of freedom, quark and gluons. Since nucleons are spin 1/2 particles, for an operator $\mathcal{O}$ composed by quark fields one has

$$\langle N, p'|\mathcal{O}|N, p\rangle = \bar{u}_{p'}\Gamma(p', p)u_p \ , \tag{B.1}$$

where Γ is a matrix with spinor indices and u_p is the solution of the free Dirac equation[1]. Lorentz invariance as well C, P and CPT symmetries impose further constraints on this matrix element. As mentioned in the main text, since the transferred momentum in the considered processes is generally much smaller than $\Lambda_{\rm QCD}$ we approximated the form factors that are in general present in these expressions as constants.

Vector interaction

In the UV an X vector boson interacts with a quark current of the form $C_V^q \bar{q}\gamma^\mu q$, which gives an effective interaction

$$\mathcal{L} = C_N \bar{N}\gamma^\mu N X_\mu + \frac{\kappa_N}{2m_N}\partial_\nu(\bar{N}\sigma^{\mu\nu}N)X_\mu + \frac{g_N}{m_N}\partial^\mu(\bar{N}N)X_\mu \ . \tag{B.2}$$

Conservation of the vector current implies $g_N = 0$, while symmetry considerations fix

$$C_p = 2C_V^u + C_V^d \ , \quad C_n = C_V^u + 2C_V^d \ . \tag{B.3}$$

Symmetry considerations don't allow to simplify the expression for the magnetic moments of the nucleons

$$\mu_N^{(X)} = \frac{(C_N + \kappa_N)}{e}\,\mu_{\mathcal{N}} \ , \tag{B.4}$$

where $\mu_{\mathcal{N}}$ is the Bohr magneton, since even the sea quarks can give a contribution to these quantities. However by using the static quark model one can make an estimation [269]. Working under the assumption that the valence quarks of the nucleons have mass equal to $m_u \simeq m_d \simeq m_{\mathcal{N}}/3$[2], at lowest order the magnetic moment of each quark is given only by its charge and effective mass, *i.e.*

$$\mu_q = \frac{C_V^q}{2m_q} \ . \tag{B.5}$$

[1] This leaves the matrix element unchanged upon the substitution $\Gamma(p', p) \to \frac{\not{p}'+m}{2m}\Gamma(p', p)\frac{\not{p}+m}{2m}$.

[2] Here we are considering the effective mass of the quarks when they are bounded together by gluons, not their real mass.

In the static quark model one thus finds

$$\mu_p^{(X)} = \langle p|\mu|p\rangle = \frac{4}{3}\mu_u^{(X)} - \frac{1}{3}\mu_d^{(X)} \simeq \frac{4C_V^u - C_V^d}{e}\,\mu_{\mathcal{N}} = \frac{3C_p - 2C_n}{e}\,\mu_{\mathcal{N}}\ , \tag{B.6}$$

$$\mu_n^{(X)} = \langle n|\mu|n\rangle = -\frac{1}{3}\mu_u^{(X)} + \frac{4}{3}\mu_d^{(X)} \simeq \frac{-C_V^u + 4C_V^d}{e}\,\mu_{\mathcal{N}} = \frac{-2C_p + 3C_n}{e}\,\mu_{\mathcal{N}}\ . \tag{B.7}$$

For the electromagnetic couplings, $C_p = +e$ and $C_n = 0$, one obtains values close to the experimental ones, $\mu_p^{\rm em}|_{\rm exp} \simeq +2.792\,\mu_{\mathcal{N}}$ and $\mu_n^{\rm em}|_{\rm exp} \simeq -1.913\,\mu_{\mathcal{N}}$, within a 10%. The interaction between quarks and the X particle might also come from an effective magnetic moment interaction $\mathcal{L} = \frac{\kappa_q}{\Lambda}\partial_\nu(\bar{q}\sigma^{\mu\nu}q)X_\mu$ generated, *e.g.*, at loop level by integrating out some heavy particle in the low energy limit. This effective operator contributes to the magnetic moment of the nucleons through the substitution

$$\partial_\nu(\bar{q}\sigma^{\mu\nu}q) \to \delta_q^{(N)}\partial_\nu(\bar{N}\sigma^{\mu\nu}N) \tag{B.8}$$

where $N = p, n$, which shifts $\kappa_N \to \kappa_N + \frac{2m_N}{\Lambda}\delta_q^{(N)}$ for each q. By lattice computation [270, 271], it has been estimated

$$\delta_u^{(p)} = \delta_d^{(n)} = 0.84\ , \quad \delta_d^{(p)} = \delta_u^{(n)} = -0.23\ , \quad \delta_s^{(p)} = \delta_s^{(n)} = -0.046 \tag{B.9}$$

for the light quarks contributions.

Axial interaction

In the UV an X axial vector boson interacts with a quark current of the form $C_V^q\bar{q}\gamma^\mu\gamma^5 q$ which brings to an effective nucleon current

$$\mathcal{L} = a_N\bar{N}\gamma^\mu\gamma^5 N X_\mu + \frac{b_N}{m_N}\partial^\mu(i\bar{N}\gamma^5 N)X_\mu + \frac{d_N}{2m_N}\partial_\nu(i\bar{N}\sigma^{\mu\nu}\gamma^5 N)X_\mu\ . \tag{B.10}$$

CP conservation in QCD interactions forces $d_N = 0$, while the term proportional to b_N doesn't contribute to the considered processes when one has on-shell X[3]. The nucleon axial couplings a_N are given by the sum of quark coupling a_q weight by the fraction of the spin of the nucleon $\Delta_q^{(N)}$,

$$a_N = \sum_q \Delta_q^{(N)} C_A^q\ . \tag{B.11}$$

These fractions are given by integrals of helicity-dependent parton distributions and can be measured in lepton nucleon scattering. Their values are equal to [225, 272]

$$\Delta_u^{(p)} = \Delta_d^{(n)} = 0.897(27)\ , \quad \Delta_d^{(p)} = \Delta_u^{(n)} = -0.367(27)\ , \quad \Delta_s^{(p)} = \Delta_s^{(n)} = -0.026(4)\ , \tag{B.12}$$

while the contributions from heavy quark are small and can be neglected. As for the vector case, it's possible that the interaction between quarks and the X boson comes from an effective interaction like $\mathcal{L} = \frac{d_q}{\Lambda}\partial_\nu(i\bar{q}\sigma^{\mu\nu}\gamma^5 q)X_\mu$. This effective operator generates an electric dipole for the nucleons through the substitution

$$\partial_\nu(i\bar{q}\sigma^{\mu\nu}\gamma^5 q) \to \delta_{q5}^{(N)}\partial_\nu(i\bar{N}\sigma^{\mu\nu}\gamma^5 N) \tag{B.13}$$

where $N = p, n$, which again shifts the d_N value as before. Unfortunately the values of $\delta_{q5}^{(N)}$ are difficult to be measured and are poor known. Only recently [273] it has been measured the light quark contribution to the proton at $Q^2 = 0.8$ GeV^2

$$\delta_{u5}^{(p)} = 0.54^{+0.09}_{-0.22}\ , \quad \delta_{d5}^{(p)} = -0.23^{+0.09}_{-0.16}\ . \tag{B.14}$$

[3]This can be seen by performing and integration by parts.

Scalar interaction

The scalar interaction between quarks and a spin 0 particle is given by the scalar density operator $\bar{q}q$. The matching with the nucleon effective coupling is linked to the generation of nucleon masses [274]. From trace anomaly, the mass of the nucleons is given by

$$m_N = \langle N| \left[\sum_q m_q \bar{q}q \, + \, \frac{\beta}{4\alpha_s} G_{\mu\nu} G^{\mu\nu} \right] |N\rangle \tag{B.15}$$

where the β function at lowest order is $\beta = -\alpha_s^2/2\pi(11 - 2n_f/3)$ and α_s is the strong coupling constant. The heavy quark fields $Q = c, b, t$ can be integrated out trough the expansion [275]

$$m_Q \bar{Q}Q \to -\frac{2}{3}\frac{\alpha_s}{8\pi} G_{\mu\nu} G^{\mu\nu} \ , \tag{B.16}$$

so that

$$m_N = \langle N| \left[\sum_{q=u,d,s} m_q \bar{q}q \, - \, \frac{9\alpha_s}{8\pi} G_{\mu\nu} G^{\mu\nu} \right] |N\rangle \ . \tag{B.17}$$

We can now define the fractions of nucleon mass as

$$\begin{aligned} f_{Tq}^{(N)} &= \frac{\langle N| m_q \bar{q}q |N\rangle}{m_N}, \\ f_{TG}^{(N)} &= 1 - \sum_{q=u,d,s} f_{Tq}^{(N)}. \end{aligned} \tag{B.18}$$

We consider a scalar interaction term with the X particle defined by

$$\mathcal{L} = X \sum_q C_S^q \frac{m_q}{v} \bar{q}q \, + \, C_S^g \frac{\alpha_s}{8\pi v} X G_{\mu\nu} G^{\mu\nu} \ , \tag{B.19}$$

where $v = 246$ GeV is the Higgs vacuum expectation value. The last one is an effective interaction term that can be generated at loop level by massive particles in the low energy limit. The nucleon effective interaction reads

$$\mathcal{L} = X \sum_{N=p,n} z_N \bar{N} N \tag{B.20}$$

where

$$z_N = \frac{m_N}{v} \left[\sum_{q=u,d,s} C_S^q f_{Tq}^{(N)} \, - \, \frac{1}{9} f_{TG}^{(N)} \left(C_S^g - \frac{2}{3} \sum_{q=c,b,t} C_S^q \right) \right] \tag{B.21}$$

are the effective scalar couplings of the nucleons. The values of the fractions of nucleon mass are given by [276]

$$\begin{aligned} &f_{Tu}^{(p)} = 0.020 \pm 0.004, \quad f_{Td}^{(p)} = 0.026 \pm 0.005, \quad f_{Ts}^{(p)} = 0.118 \pm 0.062 \ , \\ &f_{Tu}^{(n)} = 0.014 \pm 0.003, \ f_{Td}^{(n)} = 0.036 \pm 0.008, \quad f_{Ts}^{(n)} = 0.118 \pm 0.062 \ . \end{aligned} \tag{B.22}$$

Pseudoscalar interaction

The pseudoscalar density $i\bar{q}\gamma^5 q$ is proportional to the divergence of the axial current $\bar{q}\gamma^\mu\gamma^5 q$. The matching with the nucleon effective operator is then done with the same $\Delta_q^{(N)}$ parameters already used. For the light quark contribution, we have

$$\langle N| m_q i\bar{q}\gamma^5 q |N\rangle = m_N \Delta_q^{(N)} \, - \, \langle N| \frac{\alpha_s}{8\pi} G_{\mu\nu} \tilde{G}^{\mu\nu} |N\rangle \ , \tag{B.23}$$

while for the heavy quark fields it's enough to expand them as [275]

$$m_Q i\bar{Q}\gamma^5 Q \to -\frac{\alpha_s}{8\pi} G_{\mu\nu}\tilde{G}^{\mu\nu} \ . \tag{B.24}$$

The nucleon matrix element for the pseudoscalar gluon operator is given by [277]

$$\langle N|\frac{\alpha_s}{8\pi} G_{\mu\nu}\tilde{G}^{\mu\nu}|N\rangle = m_N \bar{m}\left(\frac{\Delta_u^{(N)}}{m_u} + \frac{\Delta_d^{(N)}}{m_d} + \frac{\Delta_s^{(N)}}{m_s}\right) \ , \tag{B.25}$$

where $\bar{m}^{-1} = m_u^{-1} + m_d^{-1} + m_s^{-1}$. By considering an interaction term for quarks and gluons given by

$$\mathcal{L} = X\sum_q C_P^q \frac{m_q}{v} i\bar{q}\gamma^5 q \ - \ C_P^g \frac{\alpha_s}{8\pi v} X G_{\mu\nu}\tilde{G}^{\mu\nu} \ , \tag{B.26}$$

which is equivalent to

$$\mathcal{L} = -\frac{\partial_\mu X}{2v}\sum_q C_P^q \bar{q}\gamma^\mu\gamma^5 q \ - \ C_P^{gg} \frac{\alpha_s}{8\pi v} X G_{\mu\nu}\tilde{G}^{\mu\nu} \ , \tag{B.27}$$

with $C_P^{gg} = C_P^g + \sum_q C_P^q$, the effective nucleon interaction then reads

$$\mathcal{L} = X\sum_{N=p,n} h_N i\bar{N}\gamma^5 N \ , \tag{B.28}$$

where

$$h_N = \frac{m_N}{v}\sum_{q=u,d,s} \Delta_q^{(N)}\left(C_P^q - \frac{\bar{m}}{m_q} C_P^{gg}\right) \tag{B.29}$$

are the effective pseudoscalar couplings of the nucleons.

Appendix C

Combined analysis with both ^{8}Be(18.15) and ^{8}Be(17.64) energy levels

As discussed in Sec. 3.7 in a later publication [251] the ATOMKI collaboration reported the observation of the anomalous signal also in the ^{8}Be(17.64) transition, which was absent in their first analysis [22, 197]. In this section we show how our results are modified by considering both the the^{8}Be(18.15) and ^{8}Be(17.64) excited states. The best fit value for the anomalous decay rate for the ^{8}Be(17.64) transition is [251]

$$\frac{\Gamma(^8\text{Be}(17.64) \to {}^8\text{Be} + X)}{\Gamma(^8\text{Be}(17.64) \to {}^8\text{Be} + \gamma)} \, \text{BR}(X \to e^+e^-) = 4.0 \times 10^{-6} \, . \tag{C.1}$$

We will associate a relative error to this best fit, not provided by ATOMKI collaboration, equal to the one from the ^{8}Be(18.15) measurement of Eq. (3.102).

Pseudoscalar scenario

We summarize the results for the pure pseudoscalar scenario in Fig. C.1, where the shaded blue and orange areas represent the 1σ and 2σ compatibility regions with the ATOMKI ^{8}Be and ^{4}He anomalies respectively, where the former is a combination arising from both the ^{8}Be energy levels. We also overlay in red the region of parameter space satisfying the SINDRUM bound from $\pi^+ \to e^+\nu_e X$ decay [230, 252]. Note that a combined explanation of the ^{8}Be and ^{4}He anomalies is not anymore possible, once we include the constraint from the ^{8}Be(17.64) transition.

Vector and axial scenarios

We summarize the results for the spin-1 cases in Fig. C.2, with the same color code as Fig. C.1 for the regions satisfying the ATOMKI anomalies. In the upper panels we show the results for the $S^\pi = 1^-$ assignment for the X boson. As it can be seen for both ξ assignments, a combined explanation of the ^{8}Be, blue region, and ^{4}He, orange region, anomalies at 1σ is in tension with the NA48 constraint, while it is possible at the 2σ level. The 1σ and 2σ bands related to the ^{12}C transition are shown in purple in the upper panels of Fig. 3.7. Note that, if confirmed, the ^{12}C

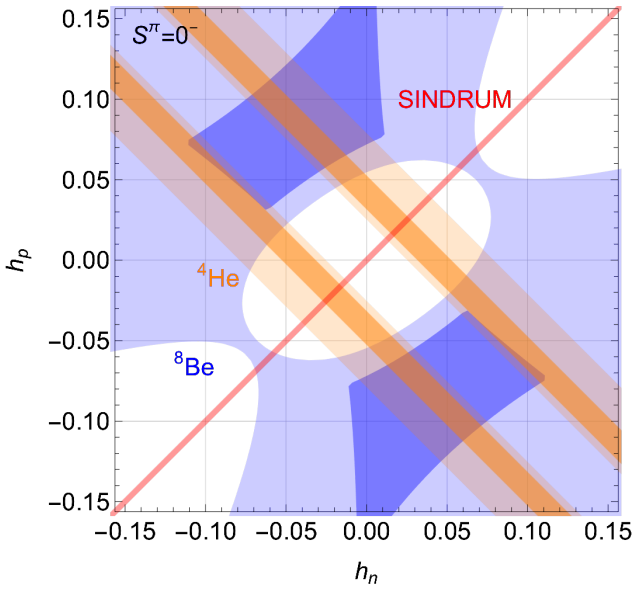

Figure C.1: Regions of the $h_{n,p}$ effective nuclear couplings of a pure pseudoscalar states where the ^{8}Be (blue) and ^{4}He (orange) anomalous ATOMKI transition can be explained at 1σ or 2σ. Inside the red region the SINDRUM bound is satisfied. Here both the ^{8}Be(18.15) and the ^{8}Be(17.64) transitions are considered.

ATOMKI anomaly is in tension with a combined explanation of the ^{8}Be and ^{4}He anomalies and the *protophobia* constraint. On the other side an axial vector $S^\pi = 1^+$ state can explain both the ^{8}Be and ^{4}He ATOMKI anomalies at 2σ, as shown in the lower panels of Fig. C.2, with axial couplings to the nucleon of $\mathcal{O}(10^{-4})$. Thus the inclusion of the ^{8}Be(17.64) transition does not change drastically the conclusion for the spin-1 cases.

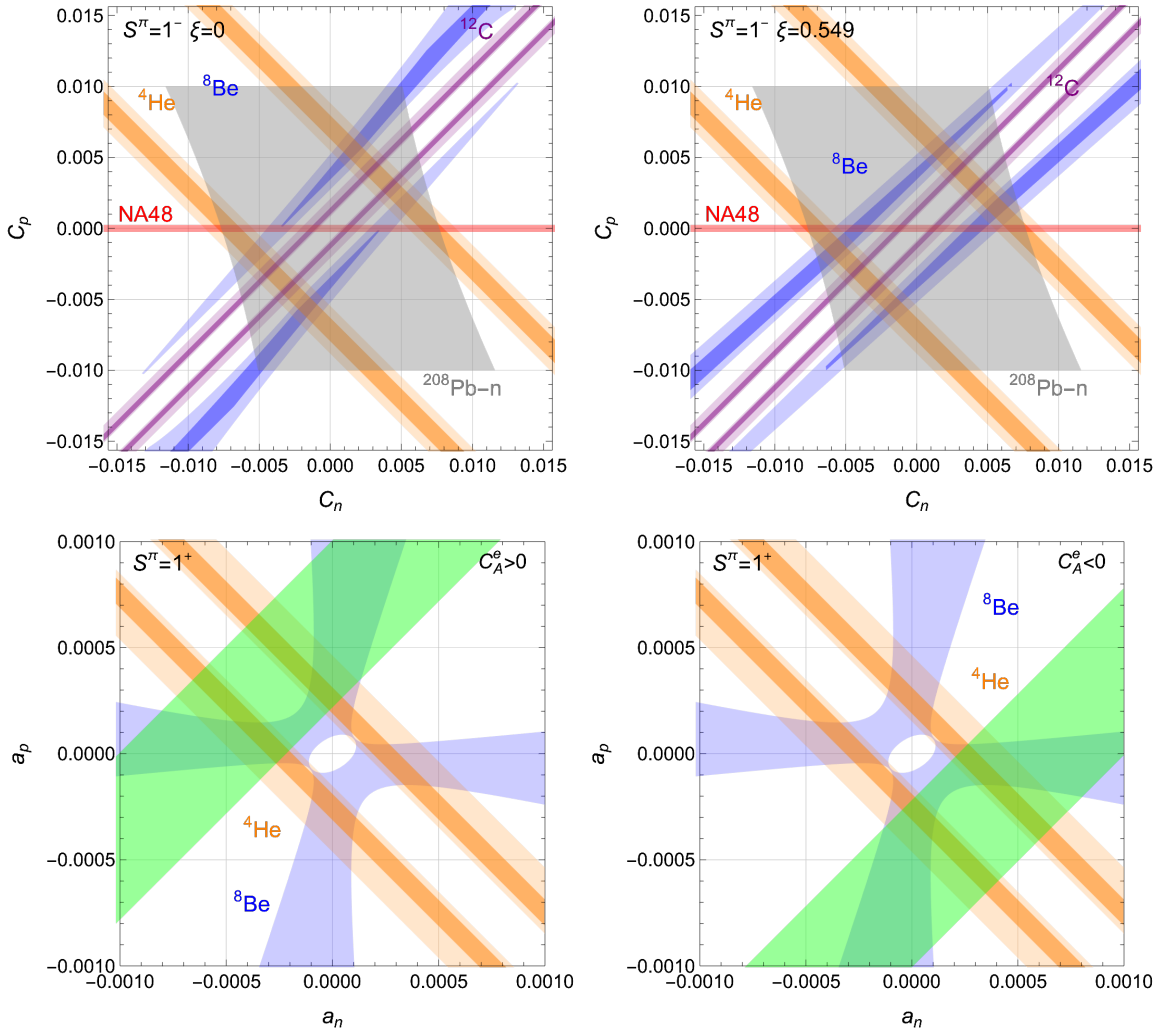

Figure C.2: *Upper panels:* Regions of the $C_{n,p}$ effective nuclear couplings of a pure vector state where the ^{8}Be (blue), ^{4}He (orange) and ^{12}C (purple) anomalous ATOMKI transition can be explained at 1σ or 2σ. Inside the red and the gray region, respectively, the NA48 and the ^{208}Pb-n scattering bound are satisfied. In the left and right panel we assume $\xi = 0$ and $\xi = 0.549$ respectively, see App. 3.4.3 for details. *Lower panels:* Regions of the $a_{n,p}$ effective nuclear couplings of a pure axial vector state where the ^{8}Be (blue) and ^{4}He (orange) anomalous ATOMKI transition can be explained at 1σ or 2σ. In the green region the KTeV anomaly in $\pi \to e^+e^-$ decay can be satisfied, by assuming a positive (left panel) and negative (right panel) value for the C_A^e axial coupling of the X boson to electrons that can explain the anomalous $(g-2)_e$. In all figures both the ^{8}Be(18.15) and the the ^{8}Be(17.64) transitions are considered, see main text for more details.

Appendix D

Cross section for resonance production

For resonance production $p + A \to N^*$, the unpolarized cross section expression is given by

$$\begin{aligned}
&\sigma(p + A \to N^*) = \\
&= \frac{1}{(2J_p+1)(2J_A+1)} \frac{1}{4m_A E_p v_p} \int \frac{d^3p_*}{(2\pi)^3 2E_*} (2\pi)^4 \delta(p_* - p_A - p_p) \sum_{pol.} |\mathcal{M}(p + A \to N^*)|^2 = \\
&= \frac{1}{(2J_p+1)(2J_A+1)} \frac{(2\pi)\delta(E_{CM}^2 - m_*^2)}{4m_A E_p v_p} \sum_{pol.} |\mathcal{M}(p + A \to N^*)|^2 \ , \qquad \text{(D.1)}
\end{aligned}$$

where $E_{CM}^2 = (p_A + p_p)^2$. Here we have treated the excited state N^* as a bound states of p and A with mass m_* and spin J_*. The reverse process defines the decay width

$$\begin{aligned}
&\Gamma(N^* \to p + A) = \\
&= \frac{1}{(2J_*+1)} \frac{1}{2m_*} \int \frac{d^3p_p}{(2\pi)^3 2E_p} \int \frac{d^3p_A}{(2\pi)^3 2E_A} (2\pi)^4 \delta(p_* - p_A - p_p) \sum_{pol.} |\mathcal{M}(N^* \to p + A)|^2 = \\
&= \frac{1}{(2J_*+1)} \frac{\sqrt{\lambda(m_*^2, m_A^2, m_p^2)}}{16\pi m_*^3} \sum_{pol.} |\mathcal{M}(N^* \to p + A)|^2 \qquad \text{(D.2)}
\end{aligned}$$

where $\lambda(x, y, z) = x^2 + y^2 + z^2 - 2xy - 2xz - 2yz$. The angular integration is trivial because the unpolarized squared matrix element of three momentum is just a function of the masses. Since the nuclear force, which mediate the interaction, is invariant under time reversal, it follows that

$$\mathcal{M}(N^* \to p + A) = \mathcal{M}(p + A \to N^*) \ . \qquad \text{(D.3)}$$

By that, one has

$$\sigma(p + A \to N^*) = \frac{(2J_*+1)}{(2J_p+1)(2J_A+1)} \frac{8\pi^2 m_*^3}{m_A E_p v_p} \frac{\Gamma(N^* \to p + A)}{\sqrt{\lambda(m_*^2, m_A^2, m_p^2)}} \delta(E_{CM}^2 - m_*^2) \ . \qquad \text{(D.4)}$$

For an off-shell state, since the excited nucleus is unstable, one should broaden the δ-function into a resonance peak by taking the narrow width approximation

$$\delta(E_{CM}^2 - m_*^2) \to \frac{1}{\pi} \frac{m_* \Gamma_*}{(E_{CM}^2 - m_*^2)^2 + m_*^2 \Gamma_*^2} \ , \qquad \text{(D.5)}$$

finally obtaining

$$\sigma(p + A \to N^*) = \frac{(2J_* + 1)}{(2J_p + 1)(2J_A + 1)} \frac{8\pi m_*^3}{m_A E_p v_p} \frac{\Gamma(N^* \to p + A)}{\sqrt{\lambda(m_*^2, m_A^2, m_p^2)}} \frac{m_* \Gamma_*}{(E_{CM}^2 - m_*^2)^2 + m_*^2 \Gamma_*^2}. \quad \text{(D.6)}$$

Bibliography

[1] L. Di Luzio, M. Nardecchia, and C. Toni, Phys. Rev. D **105**, 115042 (2022), 2204.05945.

[2] D. Barducci, L. Di Luzio, M. Nardecchia, and C. Toni, (2023), 2311.10130.

[3] D. Barducci, E. Bertuzzo, M. Taoso, and C. Toni, (2022), 2209.13469.

[4] D. Barducci and C. Toni, JHEP **02**, 154 (2023), 2212.06453, [Erratum: JHEP 07, 168 (2023)].

[5] ATLAS, G. Aad *et al.*, Phys. Lett. B **716**, 1 (2012), 1207.7214.

[6] S. Weinberg, Phys. Rev. Lett. **19**, 1264 (1967).

[7] W. A. Barletta *et al.*, Planning the Future of U.S. Particle Physics (Snowmass 2013): Chapter 6: Accelerator Capabilities, in *Snowmass 2013: Snowmass on the Mississippi*, 2014, 1401.6114.

[8] B. Holdom, Phys. Lett. B **166**, 196 (1986).

[9] M. Goodsell, J. Jaeckel, J. Redondo, and A. Ringwald, JHEP **11**, 027 (2009), 0909.0515.

[10] M. Cicoli, M. Goodsell, J. Jaeckel, and A. Ringwald, JHEP **07**, 114 (2011), 1103.3705.

[11] R. D. Peccei and H. R. Quinn, Phys. Rev. Lett. **38**, 1440 (1977).

[12] S. Weinberg, Phys. Rev. Lett. **40**, 223 (1978).

[13] J. Feng, Talk at *"Shedding light on X17"* workshop.

[14] J. A. Dror, R. Lasenby, and M. Pospelov, Phys. Rev. Lett. **119**, 141803 (2017), 1705.06726.

[15] J. A. Dror, R. Lasenby, and M. Pospelov, Phys. Rev. D **96**, 075036 (2017), 1707.01503.

[16] R. N. Mohapatra and G. Senjanovic, Phys. Rev. Lett. **44**, 912 (1980).

[17] T. Yanagida, Conf. Proc. **C7902131**, 95 (1979).

[18] M. L. Graesser, (2007), 0705.2190.

[19] M. L. Graesser, Phys. Rev. **D76**, 075006 (2007), 0704.0438.

[20] F. del Aguila, S. Bar-Shalom, A. Soni, and J. Wudka, Phys. Lett. B **670**, 399 (2009), 0806.0876.

[21] A. Aparici, K. Kim, A. Santamaria, and J. Wudka, Phys. Rev. D **80**, 013010 (2009), 0904.3244.

[22] A. J. Krasznahorkay *et al.*, Phys. Rev. Lett. **116**, 042501 (2016), 1504.01527.

[23] A. Krasznahorkay *et al.*, (2019), 1910.10459.

[24] A. J. Krasznahorkay *et al.*, Phys. Rev. C **106**, L061601 (2022), 2209.10795.

[25] R. Foot, Mod. Phys. Lett. A **6**, 527 (1991).

[26] X. G. He, G. C. Joshi, H. Lew, and R. R. Volkas, Phys. Rev. D **43**, 22 (1991).

[27] X.-G. He, G. C. Joshi, H. Lew, and R. R. Volkas, Phys. Rev. D **44**, 2118 (1991).

[28] A. Greljo, Y. Soreq, P. Stangl, A. E. Thomsen, and J. Zupan, (2021), 2107.07518.

[29] E. D'Hoker and E. Farhi, Nucl. Phys. B **248**, 59 (1984).

[30] E. D'Hoker and E. Farhi, Nucl. Phys. B **248**, 77 (1984).

[31] J. Preskill, Annals Phys. **210**, 323 (1991).

[32] F. Feruglio, A. Masiero, and L. Maiani, Nucl. Phys. B **387**, 523 (1992).

[33] A. Ismail and A. Katz, JHEP **04**, 122 (2018), 1712.01840.

[34] L. Michaels and F. Yu, JHEP **03**, 120 (2021), 2010.00021.

[35] J. Davighi, JHEP **08**, 101 (2021), 2105.06918.

[36] G. D. Kribs, G. Lee, and A. Martin, (2022), 2204.01755.

[37] N. Bizot and M. Frigerio, JHEP **01**, 036 (2016), 1508.01645.

[38] Q. Bonnefoy, L. Di Luzio, C. Grojean, A. Paul, and A. N. Rossia, JHEP **07**, 189 (2021), 2011.10025.

[39] Muon g-2, B. Abi *et al.*, Phys. Rev. Lett. **126**, 141801 (2021), 2104.03281.

[40] M. Duerr, P. Fileviez Perez, and M. B. Wise, Phys. Rev. Lett. **110**, 231801 (2013), 1304.0576.

[41] M. Duerr and P. Fileviez Perez, Phys. Lett. B **732**, 101 (2014), 1309.3970.

[42] B. A. Dobrescu and C. Frugiuele, Phys. Rev. Lett. **113**, 061801 (2014), 1404.3947.

[43] B. A. Dobrescu, (2015), 1506.04435.

[44] P. Fileviez Pérez, E. Golias, R.-H. Li, C. Murgui, and A. D. Plascencia, Phys. Rev. D **100**, 015017 (2019), 1904.01017.

[45] P. Fileviez Pérez, C. Murgui, and A. D. Plascencia, Phys. Rev. D **100**, 035041 (2019), 1905.06344.

[46] P. Fileviez Perez and M. B. Wise, JHEP **08**, 068 (2011), 1106.0343.

[47] P. Fileviez Perez, S. Ohmer, and H. H. Patel, Phys. Lett. B **735**, 283 (2014), 1403.8029.

[48] A. Wulzer, Nucl. Phys. B **885**, 97 (2014), 1309.6055.

[49] E. Izaguirre, T. Lin, and B. Shuve, Phys. Rev. Lett. **118**, 111802 (2017), 1611.09355.

[50] K. Asai, Eur. Phys. J. C **80**, 76 (2020), 1907.04042.

[51] W. Altmannshofer, J. Davighi, and M. Nardecchia, Phys. Rev. D **101**, 015004 (2020), 1909.02021.

[52] T. Araki, K. Asai, J. Sato, and T. Shimomura, Phys. Rev. D **100**, 095012 (2019), 1909.08827.

[53] Gfitter, Constraints on the oblique parameters and related theories, http://project-gfitter.web.cern.ch/project-gfitter/Oblique_Parameters/.

[54] CDF, T. Aaltonen *et al.*, Science **376**, 170 (2022).

[55] A. Djouadi, Phys. Rept. **457**, 1 (2008), hep-ph/0503172.

[56] ATLAS, G. Aad *et al.*, Phys. Rev. D **101**, 012002 (2020), 1909.02845.

[57] CMS, ATLAS, G. Aad *et al.*, (2023), 2309.03501.

[58] M. Cepeda *et al.*, CERN Yellow Rep. Monogr. **7**, 221 (2019), 1902.00134.

[59] ATLAS, G. Aad *et al.*, (2023), 2303.13613.

[60] CMS, V. Khachatryan *et al.*, Phys. Rev. D **94**, 112004 (2016), 1609.08382.

[61] Particle Data Group, R. L. Workman *et al.*, PTEP **2022**, 083C01 (2022).

[62] ATLAS, M. Aaboud *et al.*, Eur. Phys. J. C **78**, 199 (2018), 1710.09748.

[63] A. Alloul, N. D. Christensen, C. Degrande, C. Duhr, and B. Fuks, Comput. Phys. Commun. **185**, 2250 (2014), 1310.1921.

[64] C. Degrande *et al.*, Comput. Phys. Commun. **183**, 1201 (2012), 1108.2040.

[65] J. Alwall *et al.*, JHEP **07**, 079 (2014), 1405.0301.

[66] A. L. Read, Modified frequentist analysis of search results (The CL(s) method), in *Workshop on Confidence Limits*, pp. 81–101, 2000.

[67] A. L. Read, J. Phys. G **28**, 2693 (2002).

[68] L. Allwicher, P. Arnan, D. Barducci, and M. Nardecchia, JHEP **10**, 129 (2021), 2108.00013.

[69] E. C. G. Stueckelberg, Helv. Phys. Acta **11**, 225 (1938).

[70] E. C. G. Stueckelberg, Helv. Phys. Acta **11**, 299 (1938).

[71] R. Contino, The Higgs as a Composite Nambu-Goldstone Boson, in *Theoretical Advanced Study Institute in Elementary Particle Physics: Physics of the Large and the Small*, pp. 235–306, 2011, 1005.4269.

[72] L. D. Faddeev and V. N. Popov, Phys. Lett. B **25**, 29 (1967).

[73] R. Delbourgo, S. Twisk, and G. Thompson, Int. J. Mod. Phys. A **3**, 435 (1988).

[74] C. Becchi, A. Rouet, and R. Stora, Phys. Lett. B **52**, 344 (1974).

[75] C. Becchi, A. Rouet, and R. Stora, Commun. Math. Phys. **42**, 127 (1975).

[76] J. H. Lowenstein and B. Schroer, Phys. Rev. D **6**, 1553 (1972).

[77] M. Picariello and A. Quadri, Int. J. Theor. Phys. **41**, 393 (2002), hep-th/0101167.

[78] H. van Hees, (2003), hep-th/0305076.

[79] A. Proca, J. Phys. Radium **7**, 347 (1936).

[80] H. Ruegg and M. Ruiz-Altaba, Int. J. Mod. Phys. A **19**, 3265 (2004), hep-th/0304245.

[81] J. Heeck, Phys. Lett. B **739**, 256 (2014), 1408.6845.

[82] P. Minkowski, Phys. Lett. **67B**, 421 (1977).

[83] M. Gell-Mann, P. Ramond, and R. Slansky, Conf. Proc. C **790927**, 315 (1979), 1306.4669.

[84] J. Schechter and J. W. F. Valle, Phys. Rev. D **25**, 2951 (1982).

[85] J. A. Casas and A. Ibarra, Nucl. Phys. **B618**, 171 (2001), hep-ph/0103065.

[86] E. K. Akhmedov, V. A. Rubakov, and A. Y. Smirnov, Phys. Rev. Lett. **81**, 1359 (1998), hep-ph/9803255.

[87] T. Asaka and M. Shaposhnikov, Phys. Lett. B **620**, 17 (2005), hep-ph/0505013.

[88] W.-Y. Keung and G. Senjanovic, Phys. Rev. Lett. **50**, 1427 (1983).

[89] A. Ferrari *et al.*, Phys. Rev. **D62**, 013001 (2000).

[90] F. del Aguila and J. A. Aguilar-Saavedra, Nucl. Phys. **B813**, 22 (2009), 0808.2468.

[91] P. S. Bhupal Dev, R. Franceschini, and R. N. Mohapatra, Phys. Rev. **D86**, 093010 (2012), 1207.2756.

[92] J. C. Helo, M. Hirsch, and S. Kovalenko, Phys. Rev. D **89**, 073005 (2014), 1312.2900, [Erratum: Phys.Rev.D 93, 099902 (2016)].

[93] FCC-ee study Team, A. Blondel, E. Graverini, N. Serra, and M. Shaposhnikov, Nucl. Part. Phys. Proc. **273-275**, 1883 (2016), 1411.5230.

[94] A. Abada, V. De Romeri, S. Monteil, J. Orloff, and A. M. Teixeira, JHEP **04**, 051 (2015), 1412.6322.

[95] Y. Cui and B. Shuve, JHEP **02**, 049 (2015), 1409.6729.

[96] S. Antusch and O. Fischer, JHEP **05**, 053 (2015), 1502.05915.

[97] A. M. Gago, P. Hernández, J. Jones-Pérez, M. Losada, and A. Moreno Briceño, Eur. Phys. J. **C75**, 470 (2015), 1505.05880.

[98] S. Antusch, E. Cazzato, and O. Fischer, JHEP **12**, 007 (2016), 1604.02420.

[99] V. De Romeri, M. J. Herrero, X. Marcano, and F. Scarcella, Phys. Rev. D **95**, 075028 (2017), 1607.05257.

[100] A. Caputo, P. Hernandez, M. Kekic, J. López-Pavón, and J. Salvado, Eur. Phys. J. C **77**, 258 (2017), 1611.05000.

[101] A. M. Gago, P. Hernández, J. Jones-Pérez, M. Losada, and A. M. Briceño, Nucl. Part. Phys. Proc. **273-275**, 2693 (2016).

[102] A. Abada, V. De Romeri, M. Lucente, A. M. Teixeira, and T. Toma, JHEP **02**, 169 (2018), 1712.03984.

[103] S. Antusch, E. Cazzato, and O. Fischer, Phys. Lett. B **774**, 114 (2017), 1706.05990.

[104] A. Das, P. S. B. Dev, and C. Kim, Phys. Rev. D **95**, 115013 (2017), 1704.00880.

[105] A. Abada, N. Bernal, M. Losada, and X. Marcano, JHEP **01**, 093 (2019), 1807.10024.

[106] G. Cottin, J. C. Helo, and M. Hirsch, Phys. Rev. D **98**, 035012 (2018), 1806.05191.

[107] J. C. Helo, M. Hirsch, and Z. S. Wang, JHEP **07**, 056 (2018), 1803.02212.

[108] G. Cottin, J. C. Helo, and M. Hirsch, Phys. Rev. D **97**, 055025 (2018), 1801.02734.

[109] P. Hernández, J. Jones-Pérez, and O. Suarez-Navarro, Eur. Phys. J. C **79**, 220 (2019), 1810.07210.

[110] D. Dercks, H. K. Dreiner, M. Hirsch, and Z. S. Wang, Phys. Rev. D **99**, 055020 (2019), 1811.01995.

[111] J. Jones-Pérez, J. Masias, and J. Ruiz-Álvarez, Eur. Phys. J. C **80**, 642 (2020), 1912.08206.

[112] M. Hirsch and Z. S. Wang, Phys. Rev. D **101**, 055034 (2020), 2001.04750.

[113] G. Zhou, J. Y. Günther, Z. S. Wang, J. de Vries, and H. K. Dreiner, JHEP **04**, 057 (2022), 2111.04403.

[114] J. De Vries, H. K. Dreiner, J. Y. Günther, Z. S. Wang, and G. Zhou, JHEP **03**, 148 (2021), 2010.07305.

[115] Y. Liao and X.-D. Ma, Phys. Rev. D **96**, 015012 (2017), 1612.04527.

[116] H.-L. Li, Z. Ren, M.-L. Xiao, J.-H. Yu, and Y.-H. Zheng, JHEP **11**, 003 (2021), 2105.09329.

[117] A. Caputo, P. Hernandez, J. Lopez-Pavon, and J. Salvado, JHEP **06**, 112 (2017), 1704.08721.

[118] J. M. Butterworth, M. Chala, C. Englert, M. Spannowsky, and A. Titov, Phys. Rev. D **100**, 115019 (2019), 1909.04665.

[119] D. Barducci, E. Bertuzzo, A. Caputo, P. Hernandez, and B. Mele, (2020), 2011.04725.

[120] S. Balaji, M. Ramirez-Quezada, and Y.-L. Zhou, JHEP **12**, 090 (2020), 2008.12795.

[121] D. Barducci, E. Bertuzzo, A. Caputo, and P. Hernandez, JHEP **06**, 185 (2020), 2003.08391.

[122] W. Cho, K.-Y. Choi, and O. Seto, Phys. Rev. D **105**, 015016 (2022), 2108.07569.

[123] F. Delgado, L. Duarte, J. Jones-Perez, C. Manrique-Chavil, and S. Peña, (2022), 2205.13550.

[124] J. Alcaide, S. Banerjee, M. Chala, and A. Titov, JHEP **08**, 031 (2019), 1905.11375.

[125] T. Han, J. Liao, H. Liu, and D. Marfatia, JHEP **07**, 207 (2020), 2004.13869.

[126] R. Beltrán *et al.*, (2021), 2110.15096.

[127] G. Cottin, J. C. Helo, M. Hirsch, A. Titov, and Z. S. Wang, (2021), 2105.13851.

[128] CHARM, F. Bergsma *et al.*, Phys. Lett. B **157**, 458 (1985).

[129] J. Blumlein *et al.*, Z. Phys. C **51**, 341 (1991).

[130] J. Blumlein *et al.*, Int. J. Mod. Phys. A **7**, 3835 (1992).

[131] NA64, Physics Beyond Collider Conventional Beams working group, J. Bernhard, J. Phys. Conf. Ser. **1468**, 012023 (2020).

[132] M. Bauer, O. Brandt, L. Lee, and C. Ohm, (2019), 1909.13022.

[133] V. V. Gligorov, S. Knapen, M. Papucci, and D. J. Robinson, Phys. Rev. D **97**, 015023 (2018), 1708.09395.

[134] G. Aielli *et al.*, Eur. Phys. J. C **80**, 1177 (2020), 1911.00481.

[135] G. Aielli *et al.*, (2022), 2203.07316.

[136] S. Cerci *et al.*, (2021), 2201.00019.

[137] J. L. Feng, I. Galon, F. Kling, and S. Trojanowski, Phys. Rev. D **97**, 035001 (2018), 1708.09389.

[138] J. L. Feng *et al.*, (2022), 2203.05090.

[139] MoEDAL, M. Staelens, Recent Results and Future Plans of the MoEDAL Experiment, in *Meeting of the Division of Particles and Fields of the American Physical Society*, 2019, 1910.05772.

[140] J. L. Pinfold, Phil. Trans. Roy. Soc. Lond. A **377**, 20190382 (2019).

[141] SHiP, M. Anelli *et al.*, (2015), 1504.04956.

[142] SHiP, C. Ahdida *et al.*, Eur. Phys. J. C **82**, 486 (2022), 2112.01487.

[143] W. Buchmuller and D. Wyler, Nucl. Phys. B **268**, 621 (1986).

[144] N. Craig, M. Jiang, Y.-Y. Li, and D. Sutherland, JHEP **08**, 086 (2020), 2001.00017.

[145] A. Aparici, A. Santamaria, and J. Wudka, J. Phys. G **37**, 075012 (2010), 0911.4103.

[146] E. Bertuzzo and M. Taoso, JHEP **03**, 272 (2021), 2011.04735.

[147] D. Racco, A. Wulzer, and F. Zwirner, JHEP **05**, 009 (2015), 1502.04701.

[148] B. Döbrich, J. Jaeckel, F. Kahlhoefer, A. Ringwald, and K. Schmidt-Hoberg, JHEP **02**, 018 (2016), 1512.03069.

[149] T. Sjostrand, S. Mrenna, and P. Z. Skands, Comput. Phys. Commun. **178**, 852 (2008), 0710.3820.

[150] C. Bierlich *et al.*, (2022), 2203.11601.

[151] J. Blumlein and J. Brunner, Phys. Lett. B **701**, 155 (2011), 1104.2747.

[152] NA64, D. Banerjee *et al.*, Phys. Rev. Lett. **125**, 081801 (2020), 2005.02710.

[153] DELPHI, P. Abreu *et al.*, Z. Phys. C **74**, 577 (1997).

[154] BaBar, J. P. Lees *et al.*, Phys. Rev. Lett. **119**, 131804 (2017), 1702.03327.

[155] ALEPH, A. Heister *et al.*, Eur. Phys. J. C **28**, 1 (2003).

[156] ATLAS, ATLAS-CONF-2022-017 (2022).

[157] CDF, A. Abulencia *et al.*, Phys. Rev. Lett. **99**, 121801 (2007), 0704.0760.

[158] DELPHI, J. Abdallah *et al.*, Eur. Phys. J. C **38**, 395 (2005), hep-ex/0406019.

[159] S. Ask *et al.*, DELPHI 2002-077 CONF 611 (2002).

[160] X. Chu, J. Pradler, and L. Semmelrock, Phys. Rev. D **99**, 015040 (2019), 1811.04095.

[161] G. 't Hooft, NATO Sci. Ser. B **59**, 135 (1980).

[162] S. Dimopoulos, S. Raby, and L. Susskind, Nucl. Phys. B **173**, 208 (1980).

[163] A. Boyarsky, M. Ovchynnikov, O. Ruchayskiy, and V. Syvolap, Phys. Rev. D **104**, 023517 (2021), 2008.00749.

[164] K. Bondarenko *et al.*, JHEP **07**, 193 (2021), 2101.09255.

[165] N. Sabti, A. Magalich, and A. Filimonova, JCAP **11**, 056 (2020), 2006.07387.

[166] X. Chu, J.-L. Kuo, and J. Pradler, Phys. Rev. D **101**, 075035 (2020), 2001.06042.

[167] J. H. Chang, R. Essig, and S. D. McDermott, JHEP **09**, 051 (2018), 1803.00993.

[168] SHiP, CERN-SPSC-2019-049, SPSC-SR-263 (2019).

[169] TOTEM, G. Antchev *et al.*, Eur. Phys. J. C **79**, 103 (2019), 1712.06153.

[170] T. Pierog, I. Karpenko, J. M. Katzy, E. Yatsenko, and K. Werner, Phys. Rev. C **92**, 034906 (2015), 1306.0121.

[171] B. Döbrich, J. Jaeckel, and T. Spadaro, JHEP **05**, 213 (2019), 1904.02091, [Erratum: JHEP 10, 046 (2020)].

[172] L. Darmé, S. A. R. Ellis, and T. You, JHEP **07**, 053 (2020), 2001.01490.

[173] SHiP, C. Ahdida *et al.*, Eur. Phys. J. C **81**, 451 (2021), 2011.05115.

[174] SHiP, C. Ahdida *et al.*, JHEP **04**, 077 (2019), 1811.00930.

[175] G. Magill, R. Plestid, M. Pospelov, and Y.-D. Tsai, Phys. Rev. D **98**, 115015 (2018), 1803.03262.

[176] SHiP, Private communication.

[177] FASER, A. Ariga *et al.*, Phys. Rev. D **99**, 095011 (2019), 1811.12522.

[178] FASER, H. Abreu *et al.*, Eur. Phys. J. C **80**, 61 (2020), 1908.02310.

[179] FASER, H. Abreu *et al.*, (2020), 2001.03073.

[180] SHiP, C. Ahdida *et al.*, (2020), 2002.08722.

[181] LHCb, R. Aaij *et al.*, JHEP **07**, 134 (2018), 1804.09214, [Erratum: JHEP 05, 076 (2019)].

[182] LHCb, R. Aaij *et al.*, JHEP **10**, 172 (2015), 1509.00771, [Erratum: JHEP 05, 063 (2017)].

[183] S. Foroughi-Abari, F. Kling, and Y.-D. Tsai, Phys. Rev. D **104**, 035014 (2021), 2010.07941.

[184] K. Jodłowski and S. Trojanowski, JHEP **05**, 191 (2021), 2011.04751.

[185] H. K. Dreiner, D. Köhler, S. Nangia, and Z. S. Wang, (2022), 2207.05100.

[186] Belle-II, L. Aggarwal *et al.*, (2022), 2207.06307.

[187] DUNE, A. Abed Abud *et al.*, (2022), 2203.06100.

[188] J. P. Chou, D. Curtin, and H. J. Lubatti, Phys. Lett. B **767**, 29 (2017), 1606.06298.

[189] D. Curtin *et al.*, Rept. Prog. Phys. **82**, 116201 (2019), 1806.07396.

[190] V. V. Gligorov, S. Knapen, B. Nachman, M. Papucci, and D. J. Robinson, Phys. Rev. D **99**, 015023 (2019), 1810.03636.

[191] E. Bertuzzo, A. Scaffidi, and M. Taoso, (2022), 2201.12253.

[192] L. Buonocore, C. Frugiuele, F. Maltoni, O. Mattelaer, and F. Tramontano, JHEP **05**, 028 (2019), 1812.06771.

[193] CHARM-II, K. De Winter *et al.*, Nucl. Instrum. Meth. A **278**, 670 (1989).

[194] CHARM-II, P. Vilain *et al.*, Phys. Lett. B **335**, 246 (1994).

[195] G. R. Brown, Sensitivity Study for Low Mass Dark Matter Search at DUNE, Master's thesis, Texas U., Arlington, 2018.

[196] M. Hostert, *Hidden Physics at the Neutrino Frontier: Tridents, Dark Forces, and Hidden Particles*, PhD thesis, Durham U., 2019.

[197] A. J. Krasznahorkay *et al.*, J. Phys. Conf. Ser. **1056**, 012028 (2018).

[198] A. J. Krasznahorkay *et al.*, Phys. Rev. C **104**, 044003 (2021), 2104.10075.

[199] J. Gulyás *et al.*, Nucl. Instrum. Meth. A **808**, 21 (2016), 1504.00489.

[200] D. Tilley *et al.*, Nucl. Phys. A **745**, 155 (2004).

[201] D. Tilley, H. Weller, and G. Hale, Nucl. Phys. A **541**, 1 (1992).

[202] T. Walcher, Phys. Lett. B **31**, 442 (1970).

[203] J. Kelley, J. Purcell, and C. Sheu, Nucl. Phys. A **968**, 71 (2017).

[204] R. Segel, S. Hanna, and R. Allas, Phys. Rev. **139**, B818 (1965).

[205] MEG II, A. M. Baldini *et al.*, Eur. Phys. J. C **78**, 380 (2018), 1801.04688.

[206] M. Chiappini *et al.*, Nucl. Instrum. Meth. A **1041**, 167314 (2022).

[207] G. Azuelos *et al.*, Status of the X17 search in Montreal, 2022, 2211.11900.

[208] A. F. V. Cortez, H. N. da Luz, R. Sýkora, B. Ali, and L. Fajt, Nucl. Instrum. Meth. A **1047**, 167858 (2023).

[209] M. Raggi and V. Kozhuharov, Adv. High Energy Phys. **2014**, 959802 (2014), 1403.3041.

[210] M. Raggi, V. Kozhuharov, and P. Valente, EPJ Web Conf. **96**, 01025 (2015), 1501.01867.

[211] E. Nardi, C. D. R. Carvajal, A. Ghoshal, D. Meloni, and M. Raggi, Phys. Rev. D **97**, 095004 (2018), 1802.04756.

[212] L. Darmé, M. Mancini, E. Nardi, and M. Raggi, (2022), 2209.09261.

[213] X. Zhang and G. A. Miller, Phys. Lett. B **773**, 159 (2017), 1703.04588.

[214] H. W. Hammer, C. Ji, and D. Phillips, J. Phys. G **44**, 103002 (2017), 1702.08605.

[215] H.-X. Chen, (2020), 2006.01018.

[216] V. Kubarovsky, J. R. West, and S. J. Brodsky, (2022), 2206.14441.

[217] C.-Y. Wong, QED Meson Description of the X17 and Other Anomalous Particles, in *Shedding light on X17*, 2022, 2201.09764.

[218] A. Aleksejevs, S. Barkanova, Y. G. Kolomensky, and B. Sheff, (2021), 2102.01127.

[219] J. L. Feng *et al.*, Phys. Rev. Lett. **117**, 071803 (2016), 1604.07411.

[220] J. L. Feng *et al.*, Phys. Rev. D **95**, 035017 (2017), 1608.03591.

[221] J. L. Feng, T. M. P. Tait, and C. B. Verhaaren, Phys. Rev. D **102**, 036016 (2020), 2006.01151.

[222] NA48/2, J. R. Batley *et al.*, Phys. Lett. B **746**, 178 (2015), 1504.00607.

[223] X. Zhang and G. A. Miller, (2020), 2008.11288.

[224] N. J. Sas *et al.*, (2022), 2205.07744.

[225] J. Kozaczuk, D. E. Morrissey, and S. Stroberg, Phys. Rev. D **95**, 115024 (2017), 1612.01525.

[226] L. Delle Rose, S. Khalil, S. J. D. King, S. Moretti, and A. M. Thabt, Phys. Rev. D **99**, 055022 (2019), 1811.07953.

[227] B. Puliçe, Chin. J. Phys. **71**, 506 (2021), 1911.10482.

[228] P. Fayet, Eur. Phys. J. C **77**, 53 (2017), 1611.05357.

[229] U. Ellwanger and S. Moretti, JHEP **11**, 039 (2016), 1609.01669.

[230] D. S. M. Alves and N. Weiner, JHEP **07**, 092 (2018), 1710.03764.

[231] D. S. M. Alves, Phys. Rev. D **103**, 055018 (2021), 2009.05578.

[232] J. Liu, N. McGinnis, C. E. M. Wagner, and X.-P. Wang, JHEP **05**, 138 (2021), 2102.10118.

[233] M. Hostert and M. Pospelov, Phys. Rev. D **105**, 015017 (2022), 2012.02142.

[234] A. R. Edmonds, *Angular momentum in quantum mechanics* (Princeton University Press).

[235] J. D. Walecka, *Theoretical Nuclear And Subnuclear Physics*, 2 ed. (World Scientific Publishing Company, 2004).

[236] L. D. Landau and E. M. Lifshitz, *Quantum mechanics: non-relativistic theory* .

[237] S. Pastore, R. Wiringa, S. C. Pieper, and R. Schiavilla, Phys. Rev. C **90**, 024321 (2014), 1406.2343.

[238] W. Horiuchi and Y. Suzuki, Int. J. Mod. Phys. A **24**, 2134 (2009).

[239] A. Anastasi *et al.*, Phys. Lett. **B750**, 633 (2015), 1509.00740.

[240] SLAC E158, P. L. Anthony *et al.*, Phys. Rev. Lett. **95**, 081601 (2005), hep-ex/0504049.

[241] Y. Kahn, G. Krnjaic, S. Mishra-Sharma, and T. M. P. Tait, JHEP **05**, 002 (2017), 1609.09072.

[242] J. D. Bjorken *et al.*, Phys. Rev. **D38**, 3375 (1988).

[243] S. Andreas, C. Niebuhr, and A. Ringwald, Phys. Rev. **D86**, 095019 (2012), 1209.6083.

[244] NA64, D. Banerjee *et al.*, Phys. Rev. Lett. **120**, 231802 (2018), 1803.07748.

[245] NA64, D. Banerjee *et al.*, Phys. Rev. **D101**, 071101 (2020), 1912.11389.

[246] J. S. M. Ginges and V. V. Flambaum, Phys. Rept. **397**, 63 (2004), physics/0309054.

[247] C. Bouchiat and P. Fayet, Phys. Lett. **B608**, 87 (2005), hep-ph/0410260.

[248] S. G. Porsev, K. Beloy, and A. Derevianko, Phys. Rev. Lett. **102**, 181601 (2009), 0902.0335.

[249] V. A. Dzuba, J. C. Berengut, V. V. Flambaum, and B. Roberts, Phys. Rev. Lett. **109**, 203003 (2012), 1207.5864.

[250] G. Arcadi, M. Lindner, J. Martins, and F. S. Queiroz, (2019), 1906.04755.

[251] A. J. Krasznahorkay *et al.*, EPJ Web Conf. **142**, 01019 (2017).

[252] SINDRUM, R. Eichler *et al.*, Phys. Lett. B **175**, 101 (1986).

[253] NA48/2, J. R. Batley *et al.*, Phys. Lett. **B746**, 178 (2015), 1504.00607.

[254] D. G. Sutherland, Nucl. Phys. **B2**, 433 (1967).

[255] M. Veltman, Proceedings of the Royal Society of London. Series A, Mathematical and Physical Sciences **301**, 107 (1967).

[256] R. Barbieri and T. E. O. Ericson, Phys. Lett. B **57**, 270 (1975).

[257] M. Hostert and M. Pospelov, Phys. Rev. D **108**, 055011 (2023), 2306.15077.

[258] KTeV, E. Abouzaid *et al.*, Phys. Rev. D **75**, 012004 (2007), hep-ex/0610072.

[259] E. Abouzaid *et al.*, Phys. Rev. D **75**, 012004 (2007).

[260] M. Hoferichter, B.-L. Hoid, B. Kubis, and J. Lüdtke, Phys. Rev. Lett. **128**, 172004 (2022).

[261] P. Vasko and J. Novotny, JHEP **10**, 122 (2011), 1106.5956.

[262] T. Husek, K. Kampf, and J. Novotný, Eur. Phys. J. C **74**, 3010 (2014), 1405.6927.

[263] Y. Kahn, M. Schmitt, and T. M. P. Tait, Phys. Rev. D **78**, 115002 (2008), 0712.0007.

[264] R. H. Parker, C. Yu, W. Zhong, B. Estey, and H. Müller, Science **360**, 191 (2018), 1812.04130.

[265] L. Morel, Z. Yao, P. Cladé, and S. Guellati-Khélifa, Nature **588**, 61 (2020).

[266] F. Jegerlehner and A. Nyffeler, Phys. Rept. **477**, 1 (2009), 0902.3360.

[267] D. Hanneke, S. Fogwell, and G. Gabrielse, Phys. Rev. Lett. **100**, 120801 (2008), 0801.1134.

[268] H. Bélusca-Maïto, A. Ilakovac, M. Madjor-Božinović, and D. Stöckinger, JHEP **08**, 024 (2020), 2004.14398.

[269] *http://webusers.fis.uniroma3.it/ ceradini/dispenseFNS_last.pdf* .

[270] LHPC, TXL, D. Dolgov *et al.*, Phys. Rev. D **66**, 034506 (2002), hep-lat/0201021.

[271] S. Aoki, M. Doui, T. Hatsuda, and Y. Kuramashi, Phys. Rev. D **56**, 433 (1997), hep-lat/9608115.

[272] F. Bishara, J. Brod, B. Grinstein, and J. Zupan, JCAP **02**, 009 (2017), 1611.00368.

[273] M. Anselmino *et al.*, Nucl. Phys. B Proc. Suppl. **191**, 98 (2009), 0812.4366.

[274] J. Fan, M. Reece, and L.-T. Wang, JCAP **11**, 042 (2010), 1008.1591.

[275] M. A. Shifman, A. Vainshtein, and V. I. Zakharov, Phys. Lett. B **78**, 443 (1978).

[276] J. R. Ellis, A. Ferstl, and K. A. Olive, Phys. Lett. B **481**, 304 (2000), hep-ph/0001005.

[277] H.-Y. Cheng and C.-W. Chiang, JHEP **07**, 009 (2012), 1202.1292.